BAŞKENT UNIVERSITY
INSTITUTE OF SCIENCE AND ENGINEERING
DEPARTMENT OF DEFENSE TECHNOLOGIES AND SYSTEMS
MASTER OF SCIENCE IN DEFENSE PLATFORMS

OPTIMIZATION OF NUMBER, SEQUENCE AND THICKNESS OF LAYERS FOR METAL – CERAMIC MULTILAYER ARMOR

BY

ALİ CAN TURAN

MASTER OF SCIENCE THESIS

ANKARA - 2021

BAŞKENT UNIVERSITY
INSTITUTE OF SCIENCE AND ENGINEERING
DEPARTMENT OF DEFENSE TECHNOLOGIES AND SYSTEMS
MASTER OF SCIENCE IN DEFENSE PLATFORMS

OPTIMIZATION OF NUMBER, SEQUENCE AND THICKNESS OF LAYERS FOR METAL – CERAMIC MULTILAYER ARMOR

BY

ALİ CAN TURAN

MASTER OF SCIENCE THESIS

ADVISOR

PROF. DR. FARUK ELALDI

ANKARA – 2021

BAŞKENT UNIVERSITY
INSTITUTE OF SCIENCE AND ENGINEERING

This study, which was prepared by Ali Can TURAN, for the program of Defense Platforms, has been approved in partial fulfillment of the requirements for the degree of MASTER OF SCIENCE in Defense Technologies and Systems Department by the following committee.

Date of Thesis Defense: 22 / 12 / 2021

Thesis Title: The Optimization of the Number, Sequence and Thickness of Layers for Metal – Ceramic Multilayer Armor.

Examining Committee Members	**Signature**
Prof. Dr. Faruk ELALDI	…………………..
Prof. Dr. Yusuf Tansel İÇ	…………………..
Dr. Öğr. Üyesi Turgut AKYÜREK	…………………..

APPROVAL

Prof. Dr. Faruk ELALDI
Director, Institute of Science and Engineering

DATE: … / … / ……..

BAŞKENT ÜNİVERSİTESİ
FEN BİLİMLER ENSTİTÜSÜ
YÜKSEK LİSANS / DOKTORA TEZ ÇALIŞMASI ORİJİNALLİK RAPORU

Tarih: 23 / 12 / 2022

Öğrencinin Adı, Soyadı : Ali Can TURAN
Öğrencinin Numarası : 21910544
Anabilim Dalı : Savunma Teknolojileri ve Sistemleri
Programı : Savunma Platformları Tezli Yüksek Lisans Programı
Danışmanın Unvanı/Adı, Soyadı : Prof. Dr. Faruk ELALDI
Tez Başlığı : Optimization of Number, Sequence and Thickness of Layers for Metal-Ceramic Multilayer Armor

Yukarıda başlığı belirtilen Yüksek Lisans tez çalışmamın; Giriş, Ana Bölümler ve Sonuç Bölümünden oluşan, toplam 129 sayfalık kısmına ilişkin, 23 / 12 / 2022 tarihinde tez danışmanım tarafından "Turnitin" adlı intihal tespit programından aşağıda belirtilen filtrelemeler uygulanarak alınmış olan orijinallik raporuna göre, tezimin benzerlik oranı % 4'tür.

Uygulanan filtrelemeler:
1. Kaynakça hariç
2. Alıntılar hariç
3. Beş (5) kelimeden daha az örtüşme içeren metin kısımları hariç

"Başkent Üniversitesi Enstitüleri Tez Çalışması Orijinallik Raporu Alınması ve Kullanılması Usul ve Esaslarını" inceledim ve bu uygulama esaslarında belirtilen azami benzerlik oranlarına tez çalışmamın herhangi bir intihal içermediğini; aksinin tespit edileceği muhtemel durumda doğabilecek her türlü hukuki sorumluluğu kabul ettiğimi ve yukarıda vermiş olduğum bilgilerin doğru olduğunu beyan ederim.

Öğrenci İmzası:………………….

Onay
… / … / 20…
Prof. Dr. Faruk ELALDI

To my beloved wife, my son and dear parents...

Ali Can TURAN
Brussels - 2021

ACKNOWLEDGEMENTS

I would like to express my true gratitude to some institutions, incorporations and people via this opportunity. This list could never be exhaustive and conducive as I received much more efforts that this page would narrate for. Thus, I will confine myself with the ones that rise to prominence.

Before getting into a real tally of indebtedness, I have to state my special thanks to Prof. Dr. Faruk ELALDI who has been my motivator and guider even before being an advisor. I want to offer my sincere gratitude for his approach along the way, for advising, supervising, directing, and teaching me.

This thesis would never come in existence if it had not been for the help of Nurol Holding. I want to prioritize their material contribution herein, either provided by Nurol Teknoloji Inc. or FNSS Inc. The metal plates and ceramic pieces that were used in the experiment phase of this thesis had all been provisioned by the afore-mentioned entity. Of course, the people who behaved as intermediary or prepared and delivered me the products are of special importance in this case. On this wise, it is incumbent upon me to pronounce the names of Eralp AKGÜL, Osman BAYAT and Dilem KOÇAK.

I strongly believe that the targets would have never been prepared and put on the stage for experiments provided the contributions of the following entities had not been present then: 5th and 4th Main Maintenance Centers. These are the most prominent cornerstone maintenance centers that render Turkish Armed Forces elements undefeated through proper sustainment activities and support service involving cutting-edge technology. Therefore, I especially want to present my sincere thanks to Technical Director and Director of these institutions: Colonel Can CANDAN and Colonel Hakan ÇELİK respectively. It is again coercive for me to mention the names of some other people who did the actual work and converted the plates into confined targets by procuring sheet carbon metal plates, welding, laser cutting, band sawing, etc: Mechanical Engineer Barış AYDOĞAN, Mustafa KARABULUT, Yusuf Ziya YILMAZ and Fazlı YILMAZ.

The procurement of ammunition and allocation of ballistic test center made shooting tests possible at the end. I kindly request CES Advanced Composites and Defense Technologies Inc. and Ahmet Onur KOÇOĞLU on its behalf, as an actuator of ballistic tests, to receive my frank expression of appreciation. Furthermore, for procuring ammunition, I feel the obligation to thank Colonel (Ret.) Uğur TAŞSETEN and Kenan NALÇACI.

It is a personal necessity for me to account for the outcry of my conscience, which is actually to speak of people who either didn't fail to motivate me along this rise and fall process, or either became a mentor each to guide me through finding resources. I ought to seize this occasion to send them my candid thanks: Colonel (Ret.) Ziya SÖĞÜT, Yeşim GÖKTÜRK, İsa ATLAS, and Burak CİVELEK.

Last but above all, I cannot thank my wife, Öznur TURAN, enough for having great patience and excusing me for many nights studying. Without her, this thesis would still be alive, but I would not.

ABSTRACT

Ali Can TURAN
OPTIMIZATION OF NUMBER, SEQUENCE AND THICKNESS OF LAYERS FOR METAL – CERAMIC MULTILAYER ARMOR
Başkent University Institute of Science and Engineering
Department of Defense Technologies and Systems
2021

Determination of the number, sequence and thickness of layers in the composite armors of metal-ceramic multilayer configurations has gotten to be a very compelling issue in 21st century in terms of creating solutions yielding best ballistic performance against kinetic energy threats. This situation has evolved to be subjected to more research so as to gain more insight to resolve areas of drawbacks that have emerged so far. To mention some of these areas the effect of ceramic choice, high strength or ductile metals to be used either as cover- or back-plate, the effect of layering, best thickness ratio of ceramic to backplate, the effect of spacing, etc. have to be taken into account. It is intended within this study to cover some of these areas to end up with possible deductions towards the optimized ballistic performance. Some configurations were created to serve for this purpose. STANAG 4569 KE-4 ballistic protection level is aimed to be accomplished although the target point of view is dominant throughout the study. High velocity ballistic tests were carried out by the use of 12,7 mm steel core AP ammunitions. After ensuring the numerical results by depth of penetration conform to those of tests -simultaneously carried out- by small error margins, more numerical analyses were performed to populate sufficient data to extract the necessary deductions. In accord with these deductions, it is discovered, inter alia, that ceramic choice matters, layering is good by no means, and best protection could be elicited by a configuration in which the collocation of layers is in the order of a hard and high strength metal as coverplate, space, ceramic of high elastic modulus and ductile metal guaranteeing low density as backplate respectively.

KEYWORDS: Metal - ceramic multilayer armor, composite armor, high velocity, silicon carbide, impact,

ÖZET

Ali Can TURAN
ÇOK KATMANLI METAL-SERAMİK ZIRH SİSTEMLERİNDE KATMAN SAYI, SIRA VE KALINLIKLARININ OPTİMİZASYONU
Başkent Üniversitesi Fen Bilimleri Enstitüsü
Savunma Teknolojileri ve Sistemleri Anabilim Dalı
2021

Kinetik enerjili mühimmatlara karşı en iyi balistik performansı sağlayan çözümler üretme noktasında, çok katmanlı metal-seramik konfigürasyonlara sahip kompozit zırh sistemlerinde katmanların sayı, sıra ve kalınlıklarını belirlemek 21. yüzyılda çok ilgi uyandıran bir konu haline gelmiştir. Bu durum, şu ana değin ortaya çıkan sorun alanlarını çözmek için daha fazla kavrayış geliştirebilmeyi hedefleyen fazla sayıda araştırmaya konu olacak şekilde evrilmiştir. Sorun alanlarından bazılarını belirtmek gerekirse, kullanılan seramik cinsinin, ön veya arka tabaka için dayanımı yüksek ya da sünek metal kullanımın, katmanlamanın, optimum seramik kalınlığı - arka katman metali kalınlığı oranının, katmanlar arası boşluk bırakmanın performansa etkisi vb. dile getirilebilir. Bu çalışmada, anılan sorunlu alanlara yönelik olacak şekilde, optimum balistik performansa dair olası çıkarımlara ulaşmak hedeflenmiş, bu maksada hizmet edecek hedef konfigürasyonları tasarlanmıştır. Çalışma, hedef bakış açısı temel alınarak yürütülmüş olsa dahi STANAG 4569 KE-4 balistik koruma seviyesine ulaşmak amaç edinilmiştir. 12,7 mm çelik çekirdekli zırh delici mühimmatlar kullanılmak suretiyle yüksek hızlı balistik testler icra edilmiştir. Nümerik analizlerin eş zamanlı icra edilen balistik testler ile delme derinliği bakımından küçük hata payları dahilinde uyuştuğunu görmeyi müteakip, gerekli çıkarımları sağlayacak yeterli veriyi elde edebilmek maksadıyla daha fazla nümerik analiz gerçekleştirilmiştir. Bu çıkarımlar dahilinde -diğerleri yanında- seramik seçiminin önemli olduğu, katmanlamanın hiçbir şekilde performansa katkı sağlamadığı ve en iyi korumanın önde sert ve dayanımı yüksek bir metal, boşluk katmanı, pekliği yüksek seramik, arkada sünek ve düşük yoğunluklu bir metal sıralamasına sahip bir konfigürasyon ile sağlanabileceği tespit edilmiştir.

ANAHTAR KELİMELER: Çok katmanlı metal – seramik zırh sistemi, kompozit zırh, yüksek hız, silisyum karbür, çarpma.

TABLE OF CONTENTS

Page

LIST OF TABLES

Page

LIST OF FIGURES

Page

LIST OF SYMBOLS AND ABBREVIATIONS

β	elastic internal energy conversion coefficient
Γ	Mie Grüneisen parameter
ΔP	change in bulking pressure
Δt	time step
ΔT	temperature change
ΔU	change in elastic internal energy
ε	normal strain
ε	equivalent plastic strain
ε_f	normal strain at failure
$\dot{\varepsilon}$	plastic strain rate
$\dot{\varepsilon}_0$	reference strain rate
$\dot{\varepsilon}^*$	dimensionless plastic strain rate
$\varepsilon_x, \varepsilon_y, \varepsilon_z$	normal strains on principal axes
μ	volumetric strain
ρ	density
ρ_0	initial density
ρ_A, ρ_B	incidence and transmitted wave medium densities
σ	normal stress
σ	deviation
σ^*	stress triaxiality (Johnson – Cook model)
σ^*	normalized equivalent strength (Johnson – Holmquist model)
σ_i^*	normalized intact strength
σ_f^*	normalized fracture strength
σ_{HEL}	stress at HEL
σ_{eq}	equivalent (Von Misses) stress
σ_{tu}	ultimate tensile strength
$\sigma_x, \sigma_y, \sigma_z$	stresses on principal axes
σ_y	dynamic yield strength
σ_d	deviatoric stress
$\sigma_h, \bar{\sigma}, \sigma_i$	hydrostatic (mean) stress
$\sigma_I, \sigma_R, \sigma_T$	incident, reflected and transmitted stresses respectively
a	plug formation coefficient
a	aperture
A	area
A	static yield strength (Johnson – Cook model)
A	intact strength constant (Johnson – Holmquist model)
A_1, A_2, A_3	polynomial equation of state coefficients (compression)
AD	areal density
AP	armor piercing
APDS	armor piercing discarding sabot
APFSDS	armor piercing fin stabilized discarding sabot
b	body acceleration
B	strain hardening coefficient (Johnson – Cook model)
B	fractured strength constant (Johnson – Holmquist model)
B_0	polynomial equation of state coefficient (compression-tension)
B_1	polynomial equation of state coefficient (compression)
BLV, V_{bl}	ballistic limit velocity

c, c_2	longitudinal elastic wave speed
c_A, c_B	incidence and transmitted wave medium velocities
c_r	Rayleigh wave speed
c_s	shear wave speed
[C]	damping matrix
C	strain rate hardening coefficient (Jonson – Cook, Johnson – Holmquist and Cowder Symonds models)
C_p	specific heat capacity
C_0, C_1, C_2, C_3	strain rate hardening coefficients (a modified Johnson-Cook model)
CP	complete perforation
CG	center of gravity
CP	center of pressure
CRH	caliber radius head
D	strain rate hardening coefficient (a modified Johnson-Cook model)
D	damage parameter
D_1	damage constant (Johnson – Holmquist model)
D_2	damage exponent (Johnson – Holmquist model)
D_1, D_2, D_3	material failure constants (Johnson – Cook model)
D_4, D_5	material failure constants (Johnson – Cook model)
DOP	depth of penetration
e	specific energy
E	elastic modulus
E_1	target deformation energy
E_2	projectile fragmentation energy
E_3	fractured projectile energy
E_{DOP}	experimental DOP
E_{pp}	kinetic energy of bullet and plug
E_t	tangent modulus
f	safety factor
F	force
G	shear modulus
G_f	fracture energy
h	characteristic length
HEAT	high explosive anti-tank
HEL	hugoniot elastic limit (dynamic yield strength)
K	bulk modulus
[K]	stiffness matrix
l	length of bullet head
L	bullet length
m	mass
m	thermal softening exponent
m_p	plug mass
M	projectile mass
[M]	mass matrix
M	fractured strength exponent
M_r	projectile residual mass
n	strain hardening exponent
n	iteration number
N	intact strength exponent
N_{DOP}	numerical DOP

p	projectile deformation exponent
P	pressure
P	strain rate exponent
P_{HEL}	pressure at HEL
PP	partial penetration
s_1, s_2	slopes of shock-particle velocity
SHPB	split hopkinson pressure bar
SPH	smooth particle hydrodynamics
t	time
T	hydrodynamic tensile pressure limit
TT	target thickness
T_1, T_2	polynomial equation of state coefficients (tension)
T_{melt}	melting temperature
T_{room}	room temperature (mostly 300 °K)
T^H	homologous temperature
u, x	displacement
U_p	particle velocity
U_1, U_2	particle velocities in specific volume range
U_{pI}, U_{pR}, U_{pT}	incident, reflected and transmitted particle velocities
U_s, U_{s2}	shock wave velocity
ü	acceleration
$ü_x$, $ü_y$, $ü_z$	acceleration on principal axes
v	poisson ratio
v	specific volume
V	velocity
V_r	residual velocity of projectile
V_s,	strike velocity of projectile
WHA	tungsten (wolfram) heavy alloy
Y	static yield strength
Z	Impedance

1. INTRODUCTION

1.1. Ballistics

According to the definition of Encyclopedia Britannica [1], ballistics is defined as;

“Ballistics, science of the propulsion, flight, and impact of projectiles.”

Because of the existence of the words *propulsion, flight and impact*, it could be deducted that science of ballistics can be broken down into three subfields, which could reasonably be dubbed as interior, exterior and terminal ballistics. These subfields treat how come the actions that these three words refer respectively are substantiated.

Propulsion is realized while the projectile is inside the barrel of any weapon. Flight represents the overall unconstrained action of projectile in a medium, mostly air, located between the weapon and the target. Impact indicates the inflicting interaction between the impactor and the target. An elementary figure that encompasses all these phases a small caliber round may go through is the Figure 1.1.

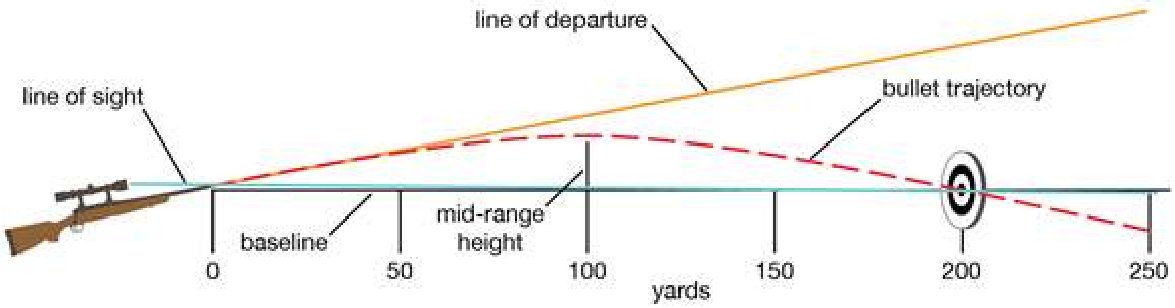

Figure 1.1. Bullet trajectory representation [1].

1.1.1. Interior ballistics

Interior ballistics is a section of ballistics that deal with all the happenings while the impactor is inside of the weapon. Thus, the field of interest of this section ends when the impactor is out of the barrel [2]. Mainly what this branch of ballistics is interested in is the motion that is relayed on a projectile by a gun. In order to maximize this motion (velocity), interior ballistics study the pressure of burning propellants, the effect of the microstructure of these propellants into pressure, the distribution of the energy acquired by burning propellants (see Table 1.1), geometry of barrel and firing chamber [3]. As it is evident from Table 1.1. that only one third of total energy is spent for projectile acceleration. To keep this portion of energy at higher levels, long barrels can be benefitted to accelerate the projectile under sustaining pressures [4]. Sustaining pressure levels can only be attained when the pressure increase is obtained by continuing rise in the amount of propellant burning, and the pressure decrease is elicited by the space emerged as the impactor get ahead through the barrel. However, these levels may not be maintained after all the propellant charge is consumed. But the pressure is maintained up until the bullet make itself out of the barrel [5]. Anyway, nearly the top velocity is elicited after a few centimeters covered through the barrel by the impactor notwithstanding the efforts to use long barrels and propellants of slow-burning rate [6].

Table 1.1. Distribution of energy created by burning propellants [3].

Energy absorbed by	*Percentage*
projectile acceleration	32
projectile friction	2
acceleration of propellant gasses	3
heat loss on gasses and barrel	62
projectile rotation and recoil	1

There should be a limit on the pressure created since high pressures and high temperatures accompanying may erode grooves and sets in the barrel. This could cause leakages in pressure and low muzzle velocities in subsequent firings [7].

At the same time, the deformation patterns the cartridge, bullet and the core in private undergo in accordance with their material properties are all within the sphere of interior ballistics research.

The chronological events that take place inside of a weapon, and relevant to interior ballistics are the release of firing pin, strike of the pin, firing of the cartridge, burning of propellant and expanding of hot gasses, acceleration of impactor by the pressure of expanding gasses through barrel, and the impactor leaving barrel [8].

1.1.2. Exterior ballistics

Exterior ballistics, concisely, deals with the projectile behavior when it is in flight, namely, between the periods of when it is out of barrel and when it strikes the target [6]. To this end, this science of ballistics studies the forces that act on the impactor, projectile stabilization issues, bullet path designation.

The forces exerted on the projectile are air drag, wind and gravitational forces. The combination of these forces determines the path of the bullet. At the same time, these forces may generate such an unbalanced motion tendency on the projectile that it tries to digress from the assumed geometrical path slightly in flight. To minimize this tendency, center of pressure (CP) in projectiles are intended to be kept at the back of center of gravity (CG) along the trajectory (see Figure 1.2.). Two kinds of stabilization measures are practiced: stabilization fins and initial rotation [9].

Stabilization fins are suitable for longer and thinner impactors where there is enough vacancy to mount these fins on. But for shorter impactors, i.e., small caliber rounds, use of fins is impossible. That is where initial rotation through the sets inside of the barrel kicks in. This rotation guarantees the bullet not to tumble and stay within the limits of assigned trajectory [9].

Wind effect on trajectory is really simple to understand. Though the rotational spin rate and the inertia of the bullet are also important to predict the degree of wind effect on an impactor, the level of the effect is literally proportional to the vectorial magnitude of the wind.

Gravitational force is a body force acting on the volume of the body. But it could be pointed out as if it acted on the center of gravity to easily find the resultant [10].

Aerodynamic force generates air drag and manipulation on the projectile path. This force is the most difficult to model compared to gravitational force and a steady wind case. Computational fluid dynamics and aiding computerized modelling devices could be very helpful to predict instantaneous and resulting behavior of impactors in flight. Nevertheless, these devices need modelling expertise and superior engineering sagacity. Even at their best, results are somewhat erroneous due to their numerical nature.

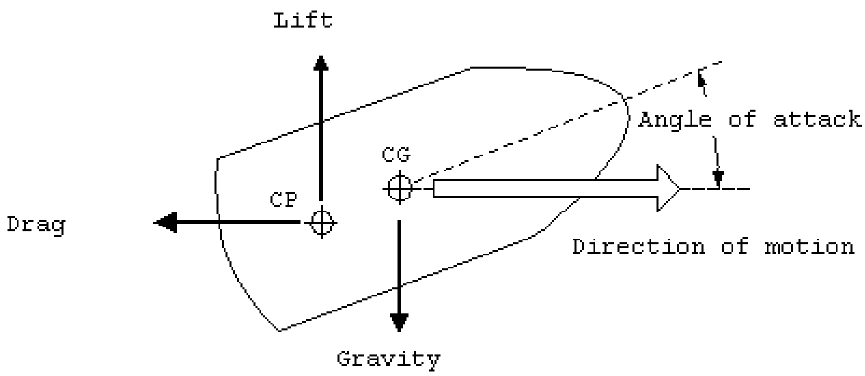

Figure 1.2. Gravitational and aerodynamic forces exerted on an impactor [11].

1.1.3. Terminal ballistics

This branch of ballistics is about the interaction between the impactor and the target [12]. The detriments target and projectile suffer, failure mechanisms, and the relation of these damage modes to the material properties of involving actors, strike angle and velocity are all the subjects that terminal ballistics inquire at, in the aftermath of an impact of very dynamic and ephemeral nature. To remain in the track of the goal of this thesis, it is necessary to mention only about high-loaded ordnance, ultra-ordnance velocities-involved situations [13]. Because we want to assume that boundary conditions are negligible and only the small portion of target material (impact region) is involved in the impacts (see subsection section 2.1.1.) [14]. Anyway, the author will take boundary conditions into consideration in the following chapters.

Projectiles impart their energy to the target and its own deformation. In military terms, the parlance target usually denotes the armored vehicle, if it is not the individual infantryman. However, there could be a necessity arising to neutralize personnel inside of the vehicles operating them, where preponderance is the ultimate goal. For these situations in military tactics, a firing in normal angles to get a complete penetration where possible is of the utmost importance for maneuverable, armored and armed tactical vehicles since the available conditions could not come into existence again to gain the sight of the target, take aim on and neutralize it before the opponent do the same. Nevertheless, the partial penetration may be enough in many situations to create influence at the interior of the vehicle by spalling effect. Spalling effect is a type of beyond armor effect, along with effects by incendiary components and poisonous gasses [4], that is likely to generate the equivalent influence on individuals inside of those vehicles (see subsection 2.2.2.).

Investigating the failure mechanisms in terms of terminal ballistics is yet another goal of this study other than producing a numerical analysis scheme conforming to the results of the experiments conducted later. Details about experiments are given in chapter 4 and 5.

1.2. Armor Threats

1.2.1. Kinetic energy threats

Kinetic energy projectiles are rounds in a more generalized term that are indebted to their mass and velocity for their energy. As they are launched from a barrel, they are orientable towards a known target. They do not incorporate explosives. While passing through the target its energy transforms into deformation, internal heat, sound energy and shock waves.

Kinetic energy projectiles should have high muzzle velocity and considerable mass to have an effect on the target [15]. Firstly, the denser the material is the more concentrated pressure at the point of impact with the same projectile diameter. Secondly, velocity increase comes along provided that more filling is present with a longer barrel and suitable trail to confront recoil.

Shorter projectiles are of cruciality in terms of avoiding wobbling and air drag (see Figure 1.3.). Notably, longer projectiles with high spin rates are compelling to stabilize [15], [16]. This can be desirable in some cases where utmost tearing and shearing effect is wanted in the target. But it is usually undesirable for longer and thinner projectiles (such as anti-tank missiles) where tumbling may afflict flight velocity and concentration degree of impact, and even the projectile may never reach the target.

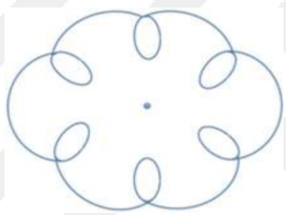

Figure 1.3. Wobbling (normal view-impact direction).

First of all, in order to avoid air drag, impactors should be axisymmetric. Otherwise, there would be produced unbalanced forces on the shaft or core making them unable to advance in void. The kinetic energy projectiles are mostly round to have smoothest aerodynamic flight.

To have a concentrated pressure on target, anti-tank missiles are made up of a slimmer shaft, which comes along with lesser aerodynamic drag as well. However so that these projectiles become able to be launched with a significant muzzle velocity without damaging the barrel, the repellent force (gas, magnetic or gunpowder) should act upon a larger area. This is secured with a sabot which is discarded by air drag later in flight. The stabilization of the long shaft is ensured by a stabilizing fin [15]. Such a round (armor piercing fin stabilized discarding sabot – APFSDS) is showed in Figure 1.4.

Small caliber impactors should also be protected against tumbling. This could be secured by angular momentum: acquisition of initial rotation. This rotation is injected through scrolled sets that are forged on the inner side of the barrel. The projectile receives a rotational force while passing through these sets in the barrel. Additionally maximum aerodynamic stabilization is acquired with conical nose-shape bullets. As for the maximum pressure to be obtained, this is elicited through a brass jacket mostly that covers the core. This jacket is squeezed between the core and the barrel hampering any expanding explosive gas leaking beyond the bullet generating turbulent air in the path of the bullet [9]. Such round examples are shown in Figure 1.5.

Figure 1.4. APFSDS round.

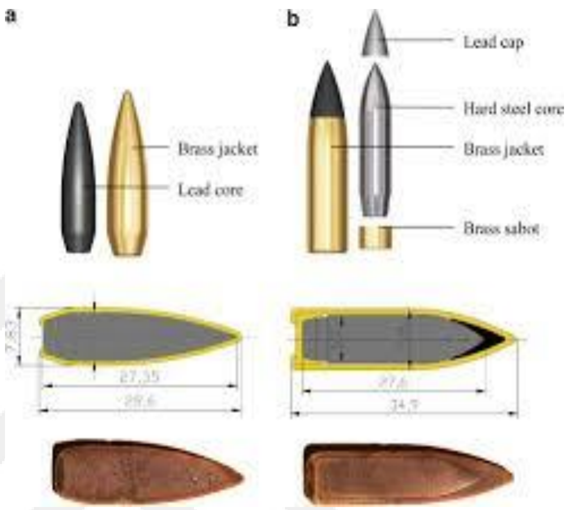

Figure 1.5. Small caliber rounds [19].

Even though the projectile cannot perforate the target, beyond armor effect shouldn't be disregarded. In fact, the damage by spalling is the main failure mechanism for the armored targets [17].

1.2.2. Chemical energy threats

Chemical energy threats are mainly high explosives and high explosive anti-tank (HEAT) ammunitions. For the course of this thesis, in order to include only the manipulated projectiles towards a target and not to include fragmentation effect, it is more suitable to stay in limits by defining shaped charge technology and its special use on HEAT ammos.

Shaped charges primarily consist of an explosive charge and a liner besides a detonator inside a cylinder [18]. Liner is mostly conical (see Figure 1.6). Working principle of shaped charges is simple. First, detonator is activated by electric ignition most of the times. Then it ignites explosive charge. Thanks to the high blast pressure coming into existence by the chemical reactions of ignited explosive, the liner bedded in a concave form [19] in front of the charge collapses into the axis of cylinder and advances normal to explosive charge towards target in high velocity, strain rates (10^4 - 10^7) and pressure [20].

Shaped charges are not launched from a gun. Instead, liner transform into a kind of stretched thin molten rod by the accelerating and expanding force of detonated chemical explosive. % 15-20 of this rod (innermost section of liner) is called as jet and it is the fastest part of the liner bulk. This jet then penetrates in fluid form the target as though it was a kinetic energy projectile. The velocity of the jet could reach and pass 9 km/s and the slug (the rear section of the rod) velocity lie in the range of 2-4 km/s [21]. But this jet ought to be kept in its integrity to achieve higher Depth of Penetration (DOP). The sustainment of this integrity depends on some parameters such as ductility and density of the liner, velocity of the tip of the jet [22].

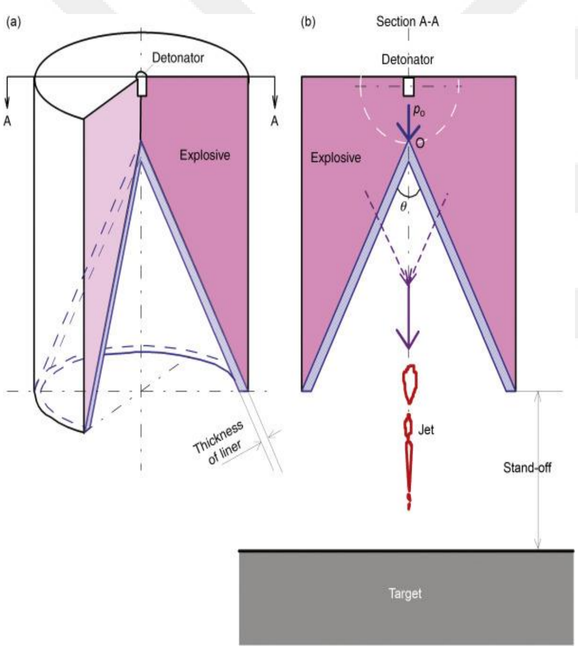

Figure 1.6. Typical conical shaped charge [23].

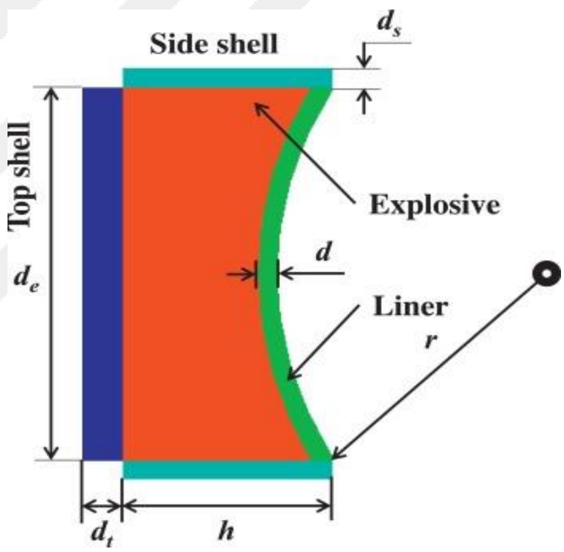

Figure 1.7. Typical hemispherical shaped charge [24].

The stand-off distance is the most crucial factor for a shaped charge to be successful enough to penetrate. Stand-off distance is the space or void between the liner diameter and the target. This distance should be long enough for stretched molten metal to form into a continuous rod, and short enough not to be broken up and fly into particles. Basic reason of this breaking up is the velocity disparity along its length. Flown particles cause inertia loss in the media decreasing DOP further in the target. There are studies searching for optimal stand-off distances to achieve maximum DOP with respect to charge diameter in literature [25]. Another factor for that media not to fly into particles is the ductility of the material used as a liner. The more ductile the material is the more time it succeeds staying in unity [18].

Density of the liner is necessarily a subject of material selection. It is a balance of availability and cost of that material. There are numerous materials tried out for a liner [26], copper being the cheapest, the most available and having an optimum performance.

Apex angle (θ) is the angle of the conical liner. Inversely proportional relationship could be made between this angle and the collapsing velocity of it. The more the collapsing velocity is the longer the length of the molten rod. But smaller angle means thinner jet and slug and less duration before particle break up: shorter stand-off distance. Therefore, there should be an optimal solution between how much DOP is desired and the radial damage needed to be produced. As a result of this balance decision, other liner models such as hemispherical (see Figure 1.7) and explosively formed penetrators exist. Though these could be assessed (especially explosively formed penetrators) in different categories, it is fundamentally related to what shape of a molten rod is desired, how much velocity is wanted, if spall (beyond armor effect) or radial damage is demanded, what the thickness of target to be penetrated is, how much stand-off distance is needed for tactical purposes etc.

HEAT ammos are nothing different than being a shaped charge module mounted on a projectile casing that launched from a platform and detonates (detonation could be complex) when the impact to target is substantiated (see Figure 1.8).

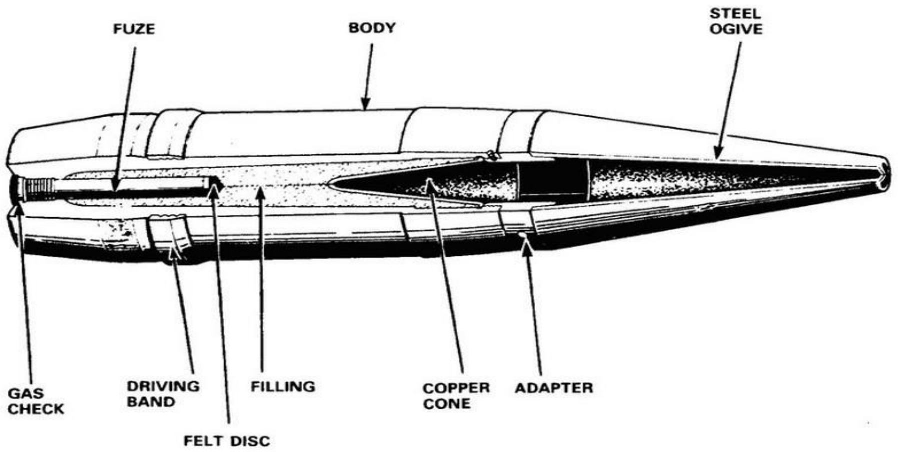

Figure 1.8. 105 mm HEAT round [27].

Shaped charges are not used only for military purposes. For example, they can be benefited in hole drilling, ice blasting, metal or tree cutting [20].

1.3. Modelling Approaches

Modelling approaches are substantial in design, test and evaluation of engineering products due to the high cost of consecutive ballistic experiments. These are made use of in the prediction of outcome in the aftermath of a ballistic impact event as well [28]. These predictions then may result in fewer tests to be conducted for a product before its debut.

Modelling procedures can be divided into three categories: numerical, empirical and analytical. Analytical modelling is an approach that benefits from the profound rules of positive sciences, necessarily physics. Computation time needed for analytically modelled cases is typically way lesser than the numerical method, but in lieu of accuracy.

The most accurate but the most expensive method is numerical approach. Implicit time integration schemes in numerical models may even get more time to compute the result of a model as it necessitates to take the inverse of stiffness matrices in every iteration. But for highly nonlinear and dynamic events such as high velocity impacts, explicit time integration scheme is used to compute stress and strain data of materials involved, in which there is no need to take the inverse of stiffness, damping and mass matrices, and there is no need to perform iterations in each time step. Therefore, convergence is guaranteed in the absence of energy and element distortion errors [29]. However, explicit method requires small time steps to be utilized for accuracy, which may prolong the simulation times and change the accuracy as well [30].

Empirical methods are generally algebraic expressions of the relation between the geometric assets of the target and projectile. In this way, they could be regarded as a regression analysis for a specific target and projectile combination including boundary conditions. Usually, the relation is between the diameter of projectile, thickness of target etc. and in the multiplication or exponential form such as in [31]. Applications of this method are usually accurate and cheap computationally. Nevertheless, the results of this method are likely to be doubted of accuracy when the case-specific values are crossed beyond the definitions attributed to them. That means extrapolation to non-experimented realms other than the case-specific ones should not be allowed. In addition, it could not be possible to extract the details of physical phenomena such as deformation patterns and damage mechanisms utilizing this method [32].

Some detailed expositions as to analytical and numerical approaches are submitted below.

1.3.1. Analytical modelling

Analytical modelling approach entails its employers to simplify the equations of basic conservation laws of energy and momentum to first- or second-degree polynomial expressions [31]. Some assumptions could be no deformation of projectiles, no mushrooming effect of blunt projectiles, kinetic energy of the impactor being dissipated only to plastic work excluding sound or heat, exclusion of elastic energy stored in projectile below Hugoniot Elastic Limit (HEL), phenomena being quasi – static etc. These simplifications in turn may disrupt the accuracy of dependent variable such as BLV. Even though these equations may yield conservative results on some occasions such as in [14] where a small caliber projectile is used on a relatively thick metal targets, anticipated conservativeness capsizes when medium or high caliber ammunition is engaged in ceramic – metal composite targets. According to Zaera and Sanches – Galves [32], the main reason for this is the more caliber a projectile has, the more localized the impact is generated by a possible medium or large caliber armor piercing (AP) projectile. This subsequently shows up as narrower conoid apex angle than normally expected, which would normally dissipate force to a large surface of backing metal. The development of grounded analytical theories through time is presented in the following paragraphs.

Being able to design and manufacture the best armor configuration, many studies have been conducted maybe since 1829, the Poncelet – Morin Hypothesis. This theorem mainly corresponds the linearized energy function of projectile, and cross-sectional area, which is based upon instantaneous depth of bullet, and upon the force exerted by target [33]. It is obvious that the independent variable -kinetic energy- of the projectile in this context cannot be conserved, due to the inelastic nature of impact phenomena, and spent in part for deformation of projectile and target.

Basic and the most famous analytical approach to find (ballistic limit velocity) BLV is the one disclosed by Recht and Ipson [34]:

$$\mathrm{V_r}=\frac{\mathrm{M}}{\mathrm{M}+m_p}\sqrt{\mathrm{V_s^2}-\mathrm{V_{bl}^2}}\ , \tag{1.1}$$

where V_s is strike velocity, V_r is residual velocity, M is projectile mass and m_p is plug mass. If plug exists, then residual velocity will drop proportionally, all other things being equal. Should the ogive-nose projectiles be wielded, no plug failure is produced and hence m_p would be zero. This approach reckons rigid behavior for projectile.

Derivation of model is quite straightforward. It settles over the basic principle of conservation of energy and momentum. When a projectile strikes a target, momentum of it is assumed to be imparted only to plug that takes shape. So, kinetic energy relayed to target as a whole is ignored. Because it is an inelastic collision, some of the energy lost, which is proportional to the mass of plug, is spent for the impulse of plug at the time of the impact. Some other division of the energy lost is spent for the shear of the plug, i.e., plastic work. Plastic work is literally related to the BLV of the target in question. Thus, plastic work is independent of the strike velocity. Remaining energy, if any, is the kinetic energy of the total mass of bullet and plug.

$$\frac{1}{2}\mathrm{MV}_{\mathrm{s}}^{2}=\frac{1}{2}\mathrm{MV}_{\mathrm{s}}^{2}\left(\frac{m_p}{\mathrm{M}+m_p}\right)+\frac{1}{2}\mathrm{MV}_{\mathrm{bl}}^{2}\left(\frac{\mathrm{M}}{\mathrm{M}+m_p}\right)+\frac{1}{2}(\mathrm{M}+m_p)\mathrm{V}_{\mathrm{r}}^{2}. \tag{1.2}$$

First term on the right side of the equation (1.2), impulse energy of the plug. Second and third terms are plastic work done and residual energy of the projectile and plug respectively. As it is easily seen from the third term, projectile behavior is supposed to be rigid. When the equation (1.2) is simplified, equation (1.1) is elicited.

Lambert et al. [33] put forth a more generalized form of equation (1.1) by introducing two experimental terms:

$$\mathrm{V}_{\mathrm{r}}=\mathrm{a}\,(V_s^p-V_{bl}^p)^{1/p}, \tag{1.3}$$

where a is plug formation coefficient and p is projectile deformation exponent. For a projectile assumed to be rigid, p equals two.

It is experienced by many authors [14], [35], [36], [37] that experimental and Lambert model least – squared curves fit each other well. For this reason, it is a primary tool for many to determine BLV.

A semi-analytical model is set forth by Chi et al. [31]. It has considerable resemblance of orientation to the one derived by Recht and Ipson [34]. As it is derived for a bilayer ceramic – metal composite armor, this model set up by Chi et el. is related to armor configurations of this thesis more than others. In addition, this model incorporates deformability of projectile. Firstly, conservation of momentum indicates:

$$\mathrm{MV}_{\mathrm{s}}=(\mathrm{M}+m_p)\mathrm{V}_{\mathrm{r}}. \tag{1.4}$$

Then, the kinetic energy of the bullet (fractured and intact as a whole) and plug is:

$$E_{pp}=\frac{1}{2}\frac{M^2}{(M+m_p)}V_s^2. \tag{1.5}$$

This energy is assumed to be utilized for defeating armor and passing through it. While passing through the target; 1. Projectile fragment ceramic, 2. Projectile deform backing plate plastically, 3. Projectile shear a plug out of plate periphery, 4. Projectile may fracture. Hence equation (1.5) can be written as:

$$E_{pp}=\frac{1}{2}(M_r+m_p)V_r^2+E_1+E_2 \tag{1.6}$$

where M_r is projectile residual mass, E_1 represents the energy which may be made use of for above-mentioned 1-3 articles and could be named as target deformation energy. E_2 is projectile fragmentation energy. Then, fractured projectile energy, E_3, could be defined as:

$$E_3 = \frac{1}{2}(M - M_r)\left(\frac{M}{M + m_p}\right)^2 V_s^2, \tag{1.7}$$

evaluating with equation (1.4).

In accordance with the model provisions, fractured projectile energy, E_3, assumed to be employed to deform and shear the target, and fracture the projectile, $E_1 + E_2$. If it is below the mentioned sum, it means the residual energy of the remaining intact projectile will undertake piercing the target. Otherwise, If E_3 is high enough to defeat the target, it will account for all target deformation, and projectile fragmentation:

$$E_3 \geq E_1 + E_2. \tag{1.8}$$

Later on, equation (1.6) can be written in two conditions:

$$E_{pp}=\frac{1}{2}(M_r+m_p)V_r^2 + E_1 + E_2, \qquad \text{for } E_3 < E_1 + E_2; \tag{1.9}$$

$$E_{pp} = \frac{1}{2}(M_r+m_p)V_r^2 + E_3, \qquad \text{for } E_3 \geq E_1 + E_2. \tag{1.10}$$

Phenomenon at the ballistic limit velocity might be a good example for first condition with residual velocity being zero. When equation (1.5) is put into equation (1.9), the revealed simplified form is:

$$E_1 + E_2 = \frac{1}{2}\frac{M^2}{(M + m_p)}V_{bl}^2. \tag{1.11}$$

Finally, if equations (1.7) and (1.11) are put into equations (1.10) and (1.9) respectively, following expressions might be extracted:

$$V_r = \left(\frac{M^2}{(M_r + m_p)(M + m_p)}(V_s^2 - V_{bl}^2)\right)^{1/2}, \qquad \text{for } E_3 < E_1 + E_2; \tag{1.12}$$

$$V_r = \left(\frac{M}{M + m_p}\right)V_s, \qquad for\ E_3 \geq E_1 + E_2. \tag{1.13}$$

Equation (1.12) is the same equation derived by Recht and Ipson [34]. But the difference come along with equation (1.13) that it prevents residual velocity to be more than strike velocity: at most, these two can be equal, plug mass being zero theoretically and assuming a rigid projectile.

For this semi – analytical model; BLV, M_r and m_p values must be fed to the model either from experiments or other means of modelling approaches such as numerical modelling. Typical plug formation that is likely to be a sample for Recht Ipson and Chi et al. models is presented in Figure 1.9.

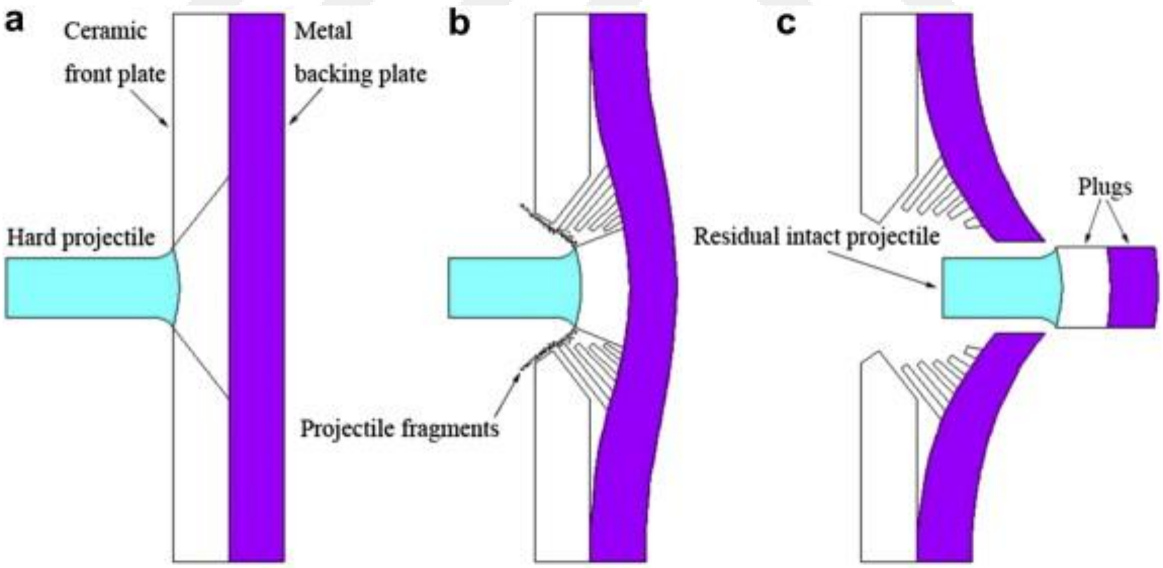

Figure 1.9. Typical plug formation for a bi-layer armor system [31].

1.3.2. Numerical modelling

Most physical problems involve differential equations -partial differential equations of second order at large- to be solved [see equation (1.14) for a one-dimensional wave equation]. Unfortunately, not all of these equations can be solved analytically. Therefore, most of the time it is not possible to find an exact result to those problems. Some numerical methods need to be developed and applied to obtain a convergent result, which could be in conformity with the data of real event within acceptable error.

Finite element method is one of numeric methods utilized to find a close solution to problems. The method itself is not recent vintage. The method is extensively used starting from the second half of the century. Even though the method involves several steps (12) through a solution, fundamental idea is the same in all the situations and simple: firstly, the problem domain should be split into a set of subdomains -discretization; secondly, an elemental equation -ordinarily polynomial- ought to be assigned to describe the behavior of every subdomain, and thirdly, all equations of these subdomains must be grouped (in a matrix system) to form a system of equations [38]. After defining the initial boundary conditions and constitutive equations there could be acquired a solution with small errors.

$$\frac{\partial^2 \mathrm{u}}{\partial \mathrm{t}^2} = \mathrm{c}^2 \frac{\partial^2 \mathrm{u}}{\partial \mathrm{x}^2} \tag{1.14}$$

For a numerical outline to be drawn, three ingredients are needed: the governing equation of the problem, constitutive equations defining the behaviors of materials, and boundary conditions [28]. For impact simulations, explicit time integration scheme is practiced. Through this scheme, firstly, the displacement, velocity and acceleration values are determined. Later on from these values, strain and stress data are garnered [29]. Though the solution explicitly proceeds as explained, accuracy might not be gained if bigger time steps are used.

In commercial analysis products of finite element method, there are a couple of domains that can be used to define subdomains within. The most employed domains to discretize subdomains are Lagrange, Euler and Smooth Particle Hydrodynamics (SPH). First two are mesh-based and the last method is a mesh-free method. Hence, there is a need to describe the outstanding qualifications of them briefly.

Lagrangian domain

This domain is the most frequently used domain in structural analyses. Within this domain, computational nodes on a structured mesh act in unison with the corresponding material points [39]. Since the coordinates of nodes and related individual material particles exactly coincide with each other, deformation at these points occurs with the same amount, pattern and simultaneously (see Figure 1.10). That means conservation of mass is secured from the start. Therefore, there is no need to incorporate additional calculations to transform and transport the strain and stress values from one to another that would otherwise be the case. This, of course, comes with lesser computational times.

A drawback of this domain is its vulnerability to mesh tangling issues when large distortions appear (see Figure 1.11) [40]. Mesh refining cannot amend the situation most of the times, but just procrastinate the time of error message pop-up in commercial simulation tools. Even though some precautions such as introducing geometric (strain) erosion to the model can be taken to prevent this issue such as in [31], it is generally in exchange for the extraction of strain energy stored in nodes prematurely, which disrupts accuracy [41]. If these precautions are not taken, then time step may fall at the low ebb and finally the process is halted by the solver with a diagnostic message accompanying.

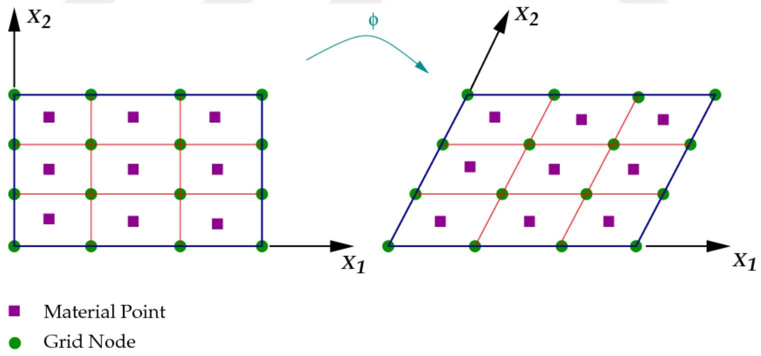

Figure 1.10. Lagrangian scheme [42].

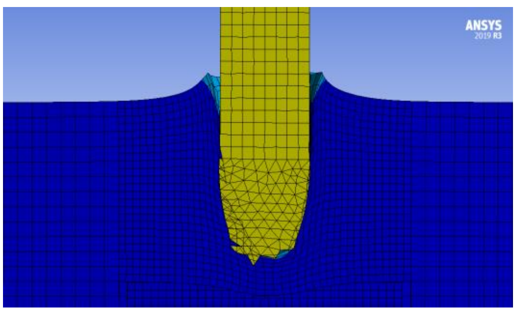

Figure 1.11. Mesh tangling on a projectile-target interface.

Eulerian domain

Eulerian domain is normally for fluid movements or for structural displacements acting like fluid in adiabatic conditions, which grow very fast (0,0001 s – hyper velocity impacts) [39]. In order to describe these movements in accuracy and find a remedy to mesh distortions, mesh grids in this domain fixed in space and deformation takes place with respect to these grids (see Figure 1.12). Therefore, additional calculations herein need to be done for the transformation of stress data between nodes and individual material points to track time history, which cause extra computational time. Material mesh is anyway needed just to ensure the location of material atoms in space, in other words, to define boundaries or shape of the geometry. Thus, coarse material mesh is mostly adequate.

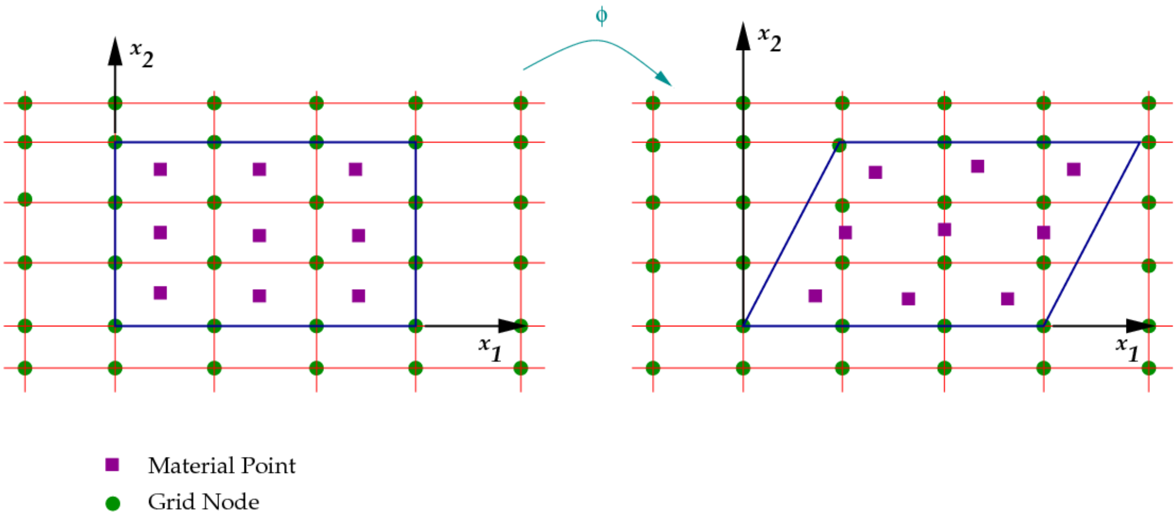

Figure 1.12. Eulerian scheme [42].

Smooth particle hydrodynamics (SPH) domain

SPH is a mesh-free discretization method (see Figure 1.13 for an example of SPH model). Because it is mesh-free, no mesh tangling issues could be present. Additionally, it is more convenient to simulate the failure mechanisms of brittle materials by this method. Because there is no danger of mismatch between a discontinuity and the relevant elements along the crack path. This is maybe the major advantage of SPH over lagrangian scheme as lagrangian elements cannot be divided within itself to model cracks; they deform or erode only.

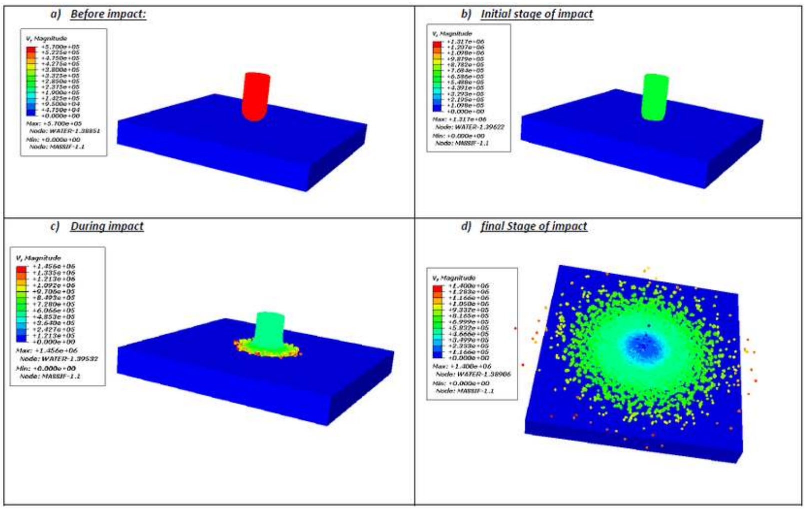

Figure 1.13. Water jet modelled in SPH domain impacting a plate [43].

One advantage of SPH over eulerian scheme is that only the materials engaged in the analysis have to be modelled whereas, in eulerian scheme, the space the material particles would tend towards should also be modelled. However, material particles scattered around need to locate one another for any possible interaction since the space they are moving is not modelled. Naturally, this means more computations to be handled and more simulation time [28].

As a result, despite the afore-mentioned advantages of euler and SPH regimes, lagrangian scheme will be used in this thesis. First reason of this choice is that scrutinizing the failure mechanisms of the damaged targets is second priority to deciding only on the best target configuration of the similar and even the equal areal densities (AD). Thus, there is slight visual interest, there should be quite a small need for SPH scheme. Second reason is that, according to the author, the most manipulative asset in this decision-making process is the computation time considering the best computing properties at hand are 16 GB of ram and 2,21 GHZ of processing capacity. As lagrangian scheme offer the least computational effort among others, it will be the discretization domain to utilize.

1.4. Previous Studies

Through time, the weapon systems of a country, of course armor systems as a mirroring sector of it, have been the major deterrents besides being warfare tools. Countries to have means of power globally, pushed its scholars into investigate and develop competent armor systems beside other warfare-related issues. Anyhow, no material meet all the requirements expected from them [44]. Thus, researchers seek for partial fulfilment of performance requirements for each particular case. While some of their studies have been focusing on the optimization of configuration and sequence of armor systems, some others have dealt with improving material properties of armor constituents. Somehow the latter topic is said to be found less frequent in literature [45]. Though the high strength metals such as steel and aluminum have been investigated as armor and replaced bronze and iron for centuries ago due to their insufficiency in defeating a threat [8], ceramics are relatively new for composite armor systems; extended studies may be found as late as 1990's [46]. An increasing interest in layered structures to enhance armor performance is also newly developed, limited, and inconsistent. Below is presented some examples from literature that have treated and experimented both metals and ceramics to get an insight of how they behave in a multilayered e armor system, or standalone.

Chi et al. [31] studied the performance of bi-layer ceramic-metal armor systems under the impact of 20 mm armor piercing discarding sabot (APDS) ammunition. They aimed at developing numerical model which would be verified by available experiments then. After verification, they produced simulations from the model to feed semi-analytical model, which they developed simultaneously, with BLV, residual projectile and plug mass values. Moreover, in their extended study, they showed through simulations taking impactor diameter as the denominator of other dimensions that the bi-layer armor numerical model is conformant to scaling laws. Finally, they concluded with the results of their empirical study that the optimum thickness ratio of ceramic thickness to total thickness in a bi-layer armor system should lie somewhere in between 0,55 and 0.6.

Ubeyli et al. [47] had their research focused onto the effect of back plate hardness level on the performance of ceramic-metal composite armor systems. They obtained steels with different hardness figures after intercritical annealing treatments. The other variable of theirs was areal density (AD). Under varied AD and hardness values, they found, back plate hardness does not have much effect on the performance.

Espinoza et al. [46], in their extensive work, studied the effect of front and back plate hardness and thickness, ceramic type, graphite thickness, varied stiffness due to welding on the metal-ceramic armor system under the impact of tungsten heavy alloy (WHA) penetrators (see Figure 1.14. for a better conceiving of ballistic configuration). They concluded that though front and back plate hardness, back plate thickness, welding efforts, confinement of ceramic and graphite thickness to localize impact are all important factors to enhance performance; ceramic type is of minor significance. The obtained outcome was that, for ceramic type determination for a particular armor, the Hugoniot elastic limit ought to be the benchmark for high velocity impacts to put a performance distinction between them.

Goh et al. [45] studied, as it is already covered in the work of Espinoza et al. [46], the front and back plate hardness influence. But they deduced a different result: they finalized their study with an implication that thin front plate hardness values are not as important as Espinoza et al. indicated in their work. The reason of the discrepancy of findings, in the parlance of Goh et al., could be the difference of front plate thicknesses employed in the experiments. According to Goh et al., the positive performance effect of front plate in the other work might be due to interface defeat, confinement sustainability and initial shock prevention (see Figure 1.15.) capabilities likely to be obtained by thicker front plates; but not due to hardness level. Goh et al. also got able to observe dwell phenomenology in their studies (see subsection 3.2.3).

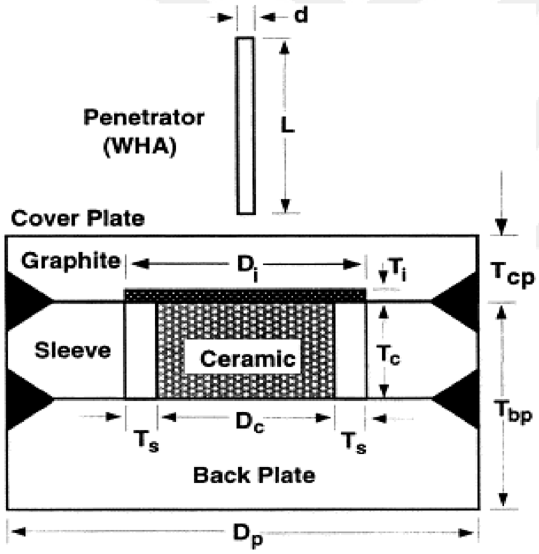

Figure 1.14. Target configuration of Espinoza et al. [46].

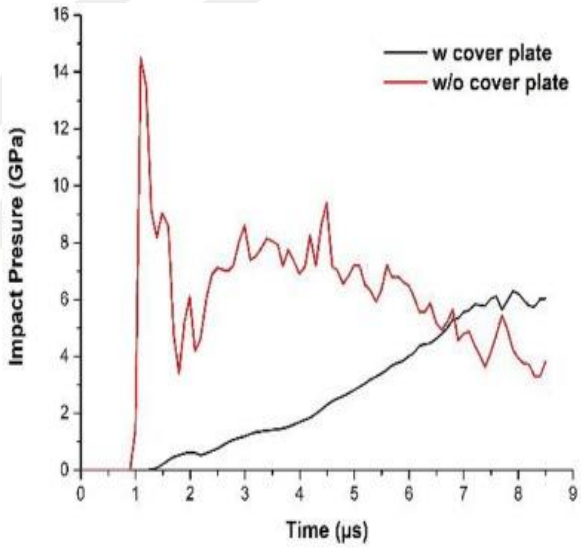

Figure 1.15. Initial shock prevention of cover plate against WHA penetrator [45].

Manes et al. [48] carried out experimental tests, and processed analytical and numerical models to predict and find residual velocity and depth of penetration values against monolithic aluminum plates under the impact of low caliber projectiles. Real ammunition with sabot and core was used. Hereby with this study, the so-called significance of friction coefficient values to manipulate analytical and numerical results came up to surface. Despite the general idea that no friction is needed to be applied in high velocity impact simulations where materials behave as if they were fluid because of soared adiabatic heating at the impact region [30], [14], [36], Manes et al. prefer to employ friction coefficients in their parametric study -indicating that the real phenomenon involves friction- to predict residual velocity and DOP values for aluminum plates of three different thicknesses. But Manes et al. can't be assumed sole authors in defining friction between impactor and target (see [49], [50]). However, expected inversely proportional relationship between friction coefficient, and the residual velocity and DOP was not guaranteed in the trials. Moreover, two contradictory ideas were attained about whether the friction assigned between the sabot and aluminum plate facilitated the projectile go further in the target or aggravated. Furthermore, it seems unclear why different frictions need to be put into use for targets of the same material but different thicknesses if the aim was to reflect real impact event. Nevertheless, it is accepted that friction variance along with temperature and projectile velocity change, and geometry, target material features may reverberate distinct failure mechanisms accordingly.

Borvik et al. [51] performed experiments and analytic calculations based on a cavity expansion model [52] against aluminum plates of 20, 40, 60 mm under the impact of 20 mm ogive rods and 7,62 mm bullets. Bullets are tested in its entirety and only with its core. Ballistic experiments showed that disparity between BLVs of core-only and entire-bullet shoots against same targets fluctuates between 4 and 12 percent, BLV of core-only being higher. Even if tests with cores counted to have yielded non-conservative result, it may be deduced that modelling only cores of bullets may present similar data to the ones that are modelled in its entirety.

Flores-Johnson et al. [53] might count as one of the most extensive numerical works carried out in the millennium. After many simulations with 7,62 mm bullets involved, they compared the performances of monolithic and layered plates of the same material (steel and aluminum), and of mixed layered plates of these two materials by changing the places of aluminum plate. According to the analyses and comparisons of residual velocity values, monolithic plates of the same material yield better performance than layered counterparts - which is more distinct for triple-layered plates and total thicknesses above 20 mm, while double-mixed plates with a thin aluminum plate at the front and thick steel plate at the rear performed better than monolithic steel plate of similar AD. The research concludes aluminum plates should be placed toward front to hamper themselves to have a brittle fracture due to not being supported by any ductile medium that would otherwise be the case.

The reason for layered plates performing worse is that they exhibit lower bending stiffness than monolithic ones. Another worthwhile finding is that aluminum plates attained a better performance level than steel plates of similar AD.

Teng et al. [49] performed ballistic tests and numeric studies engaging the plates of two different steels regarding their ductility level under the impact of bullets of two disparate nose shape to identify the best case in terms of order in double layer formation. Bullets are modelled elastic in simulations. Even though the failure mechanisms of target plates differ a lot between the impactors regardless of the target formation, it seems that the common response of the target samples with a front plate of high ductility is tensile tear, and of lower ductility is shear plugging for high strike velocities. Another result is the best order should be of higher ductility at the front, and of lower ductility at the back plate. This assertion is in agreement with Flores-Johnson [53]'s results. In the favor of numerical modelling, Teng et al. developed a modified Johnson-Cook model by introducing a multiplier variable (scaling factor) located at the very front of classic strength formula originating from a fact that steels have similar toughness values with differing only in strength and strain hardening, which means there is a trade-off of strength and ductility between armor steels (see Figure 1.16. for mentioned trade-off). Therefore, instead of specifying strain hardening, strain rate and temperature based strength coefficients for each steel types; designating these values for only one of them (reference steel), later on determining the first multiplier value in conformity with true stress-strain curve of the reference steel, and then assigning the second multiplier value of the other steel type only by taking the inverse of the first one to use with the same strength coefficients of reference steel is sufficient for modelling purposes.

Yunfei et al. [35] tested the ballistic performance of double-layered plates which were constituted by two kinds of steels of different strength under the impacts of blunt and ogival projectiles. For them, armor system represents better when the front layer is of higher strength and the back layer is of lower strength, which contradicts what Flores-Johnson et al. [53] found three years before. Findings herein disagree with the ones found by Teng et al. [49] either. The authors relate this discrepancy to impactors modelled as elastically deformable: not able to fracture and erode. While the authors denote higher deformation pattern as higher energy absorption capability to augment performance, Flores-Johnson et al. [53] named the same pattern as a result of lower stiffness to wane it. Another key result is that ogive bullets did not suffer a considerable amount of mass and length, while at the blunt impactor side the situation was the opposite, which in turn secure BLV and energy loss to be lesser for ogival projectiles.

Yadav and Ravichandran [54] executed ballistic experiments on laminated ceramic-polymer layers and monoblock ceramic plates of the same thickness under the impact of WHA projectiles. They concluded that polymer stratums between ceramic layers enhance the performance of layered structures by keeping the intensity of shock wave propagation lower and by arresting radial tensile cracks at the rear surfaces (see Figure 1.17. for more detailed view of crack formation in ceramic armors), which in turn may result in a more localized damage and a brief period of lateral confinement. More interestingly, this study could be one of the scarce studies performed attaining a result that a layered ceramic structure having more than two layers might yield a better performance than monoblock plate of the same thickness. In the study, it is thoroughly communicated that if polymer is stiff with a higher impedance value (medium density multiplied by elastic wave speed, or square root of the multiplication of medium density and elastic module [44], [55]), more volume of shock wave are transmitted to back plate. In this case, the failure mode of ceramic could be due to high compressive stress of bullet. If polymer has lower impedance value, then because of high volume of reflected waves, failure mechanism happens to be bending stress. After these results, reader is inclined to choose between *1.* avoiding the formation of thin and high number of layers to hamper bending stress, and using stiff polymer stratums between double or triple layers at most to hinder compressive stresses and secure shorter radial cracks; or *2.* adhere strictly to monolithic formation.

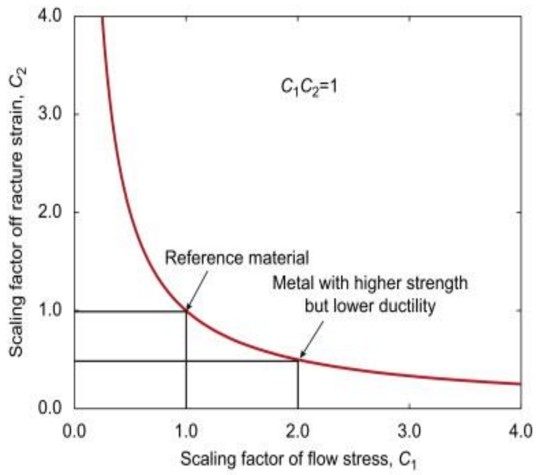

Figure 1.16. Multiplier variables, scaling factors (C_1,C_2) of reference (higher ductility) steel and higher strength steel [49].

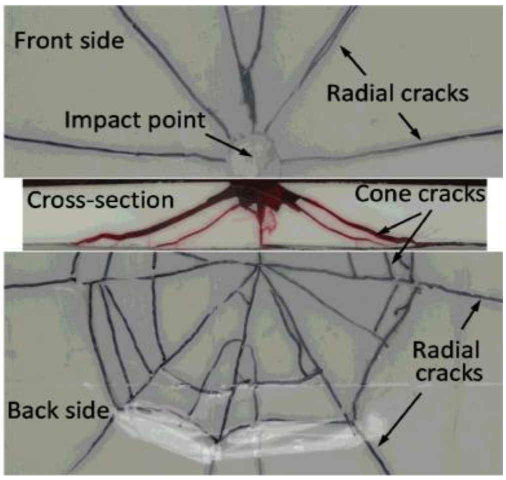

Figure 1.17. Crack formation in ceramic armors [56].

Borvik et al. [14] set to work with five steel plates of different strength-grades to try out the idea whether standard structural steels with a moderate and balanced grade of ductility and strength can be equally successful compared to high strength steels as they -reportedly- might compensate strength deficiency with their high energy absorbing competence: ductility. But findings were in the same line with the general perspective found in literature that strength is a dominant factor in comparison to ductility. Additionally, core-only shootings were also carried out against the same targets. The findings were opposite of the ones found by same leading author against aluminum plates [51]: BLVs of core-only bullets were lower than that of entire impactors yielding conservative results.

In the study of Zaera et al. [44], role of adhesive layer that is used to bond armor layers to each other was treated with regard to their impedance values and thicknesses. Experimental tests and numerical simulations were carried out. Two types of adhesives, polyurethane and epoxy resin, were employed. Epoxy resin performed better from the former since its impedance mismatch with ceramic is lower, and so is able to transmit more of shock wave to contiguous metal. As for thickness, the greater the thickness of adhesive layer is the larger volume the compressive waves have to convert to tensile waves which in the sequel would destruct and fragment ceramic layer. As for back plate, when the adhesive layer thickness is increased, the size of impact area is increased through the ceramic layer giving way to back plate to confront the exerted force with a reduced pressure. Under this dilemma, author emphasized of deciding on the thickness of adhesive layer in favor of ceramic layer as it is the main component in the armor system with its role in eroding and decelerating a projectile due to its high strength.

Roeder and Sun [57] conducted experiments and numerical analyses to determine whether layering waxes or saps the performance of aluminum-alumina composite targets. They found that armor systems of lesser in number and thicker plates perform better than thin and layered armors. In accord with authors' findings, first ceramic layer ought to be thicker enough to flatten the tip of projectile, dissipate the energy and delay the transfer of already reduced energy to back metal. In addition, it is suggested that aluminum plates with superior yield strength bring about shallower DOP values, especially for thinner aluminum plates.

Despite the majority of findings pointing out that the BLVs of ogival projectiles are lower than that of blunt projectiles since ductile hole expansion process by ogival projectiles cause lesser energy drop [35], [58], Dey et al. [36] found it is just the opposite experimentally and numerically. They asserted that because shear of target plate by blunt projectile requires lesser energy, which is why BLVs of blunt projectiles are lower than that of the other impactor in question. The main aim of the study was to demonstrate if double layered plates were equally or more successful than monolithic steel plates. When double plates of the same total thickness were involved, there was a slight decrease in BLV for ogival projectiles, which could be a result of lower bending stiffness in a layered structure; a considerable increase in BLV for blunt projectiles, for which the obstruction caused by the interaction of plugs of the consecutive and contiguous plates could be the reason. As a general comment regardless of projectile nose shape, the performance augmentation in double-layered plates could be tied to the higher energy exploitation capacity according to the authors, which conforms what Yunfei et al. [35] set forth. In the numerical simulations, it was found that ogive projectiles are lesser mesh size sensitive than blunt impactors as the latter involves localized shear. In monolithic plates, because the shear exposed cannot be reduced by bending; computational time is more for them. Finally, the effect of air gap between layers was investigated. The result was overt that air gap not necessarily impose any change in the performance of armor irrespective of impactor type unless the gap amount is such that the strike velocity diminishes between layers to some extent.

Zukas et al. [40] made a rough classification about the performance comparison of monoblock and layered structures of the same thickness and material property with regard to target thickness-impactor diameter ratio. As a summary, they suggest that the lower the ratio is the worse the performance for layered plates. In any case, the performance tends to diminish after a certain number of layers regardless of the ratio.

Holmquist et al. [59] extracted coefficients of Johnson-Holmquist continuous model for aluminum nitride in their study. One fundamental deduction in their experimental work was that layering in ceramics contracts the damaged area in making the configuration better for multi-hit situations with respect to monolithic plates, although DOP was still dissatisfying compared to its monolithic peer.

Lee and Yoo [41] tried to determine the best ceramic – back metal thickness ratio by comparing BLVs of different ceramic-metal layered armor systems with the same AD. In preliminary conclusions, they asserted that ceramic plate ought to be thick enough to have a bigger apex angle, to dissipate remaining energy to larger area at the fore surface of back plate, to erode and decelerate projectile considerably. However, if the back plate is too thin, it might not support ceramic plate against tensile failure, or fail pulverized ceramic to keep confined. Hence there should be an optimization. They found optimum thickness ratio of ceramic-metal thicknesses is 2,5, which is two times more than the result found by Chi et al. [1].

Gupta et al. [58] performed ballistic experiments and numerical analyses to shed a light on the failure mechanisms of monoblock and layered aluminum structures under the impact of ogival, blunt and hemispherical projectiles using thin aluminum plates thicknesses of which varied from 0,5 mm to 1,5 mm. Numerical analyses fell short to describe damage modes due to being modelled as axisymmetric. The results were in the same line with Yunfei et al.'s [35]. BLVs of ogival projectiles were lower compared to the others which needed more energy to shear the target. As for layering, monolithic structures outrace layered ones in general regardless of impactor nose-shape. Furthermore, when layering is piled up more, the aperture of success gets bigger in favor of monoblock armors. For blunt nose projectiles, delamination was observed in layered configurations as well as plugging phenomenon. The main failure mechanism is petalling for ogive impactors. Both failure mechanisms -plugging and petalling- were found in the targets under the impact of hemispherical bullets.

Yunfei et al. [37] studied extensively the effects of number, sequence, thickness of plates and air gap amount in multilayer armor systems along with the influence of strike velocity on the failure mechanisms and BLV values under the impact of ogival bullets, using thin steel plates thicknesses of which varied from 0,5 mm to 2 mm. One of the takeaways is that air gap is inversely influential in ballistic performance, which is a result different from what Dey et al. [36] found: no effect. Main reason of success for plates in contact is thought to be the bracing interaction between them. Another finding was energy loss barely changes irrespective of target configuration or strike velocity for ogival projectile. However, velocity loss is so tempted to have downward jumps at the whereabouts of BLV. One of other findings was that for double-layer armors of same total thickness, upper thin and lower thick layer configuration present better protection -especially for armors with moderate total thickness. Deformation patterns for monolithic structures is more intense compared to layered plates. Failure mechanisms of monolithic and layered plates, bulging and petalling, did not differ much for lower total thicknesses; when the thickness figures are pushed upwards to reach moderate total thickness levels, damage mode in monolithic plates converts to pure petalling; and in layered plates bulging through bending and stretching is more dominant, which is in favor of performance of layered plates as bulging phenomenon is more capable to absorb energy. What that means is for thicker armor systems, layered structure could be better.

Nevertheless, authors did not disclose any border between this failure mechanism change that would normally satisfy reader to decide under what thickness conditions layering should be kept in mind. Another qualitative result is that more layering decrease BLV as it is usually encountered in literature [58], [59].

Yunfei et al. [60], as it was in their previous study, treated the same variables for hemispherical projectiles. This time, the main failure mode is shear for thin multi-layered plates; when moderate thickness levels are attained, this mode turned into bulging making them outpace monolithic armor equivalents. One differing discovery for hemispherical bullets was that among the double-layered plates of the same thicknesses, the best performance is from the plates halving the total thickness.

Sherman and Ben Shushan [61] studied the significance and effects of confinement in ceramic composite armor systems. According to authors, the impact phenomena is essentially quasi-static, because *1.* projectile decelerates while digging into the target, *2.* ceramic and back plate have the same surface area and impedance values. The other variable studied was thickness of ceramic and back metal. When stiffness is increased by small increments before each ballistic test; cone crack diameter gets narrower, lesser radial cracks form, and lesser damage occurs. When thickness of ceramic layer is increased by small increments before each ballistic test; delayed and lesser radial cracks and premature cone cracks form at the rear surface of ceramic plate, which again induce lesser damage. In the same manner if steel or aluminum are confined, better performances ensue. The authors found in their experiments that thin ceramic plates fail by radial cracks (tensile failure), thick ceramic plates fail by cone cracks (compression failures). These results are conformant to shock wave propagation theory.

Zuoguang et al. [62] carried out Split Hopkinson Pressure bar (SHPB) tests to evaluate alumina-aluminum armors. In addition, the influence of accrual in ceramic and back plate thicknesses were evaluated by assessing apex angle, radial crack count, and transmitted / reflected wave intensity. When ceramic thickness is augmented, there reveals a decreasement in apex angle and an increasement in radial crack count, which is not a favorable case for performance. On the contrary, when back plate thickness is increased there reveals an increasement in apex angle and a diminishment in radial crack count along with a decay in reflected wave intensity and an escalation in transmitted wave volume. These findings are literally different from the ones [31], [41] alleging ceramic layer should be thicker than back layer. The exquisite side of the study is thought to be the critical remarks made on the study of Sherman and Ben-Shushan [61]. Authors explicitly criticize the qualification of ceramic damage as a quasi-static process. The conclude that the phenomena itself is dynamic due to a couple of reasons, exemplifying ballistic data of their own: *1.* Top view of cone cracks do not yield a sign of crushed (compressed) of pulverized ceramic, *2.* Side view of cone cracks reveals that the main failure mode is not shear but tensile indicating cone crack formation starts from the rear surface, and *3.* cone crack formation is seemingly dominated by shock wave propagation as it is observed that nearer boundary conditions produce narrower, farther ones bring about larger apex angles.

Gama et al. [63] investigated the effect of an additional thin rubber or aluminum foam layer on the performance of composite-ceramic-composite armors. They found that additional stratum delays the shock wave propagation in accordance with material properties of relevant armor layer and additional stratum thickness. Delaying of shock wave propagation means retardation in back layer failure as well, paving the way for a less damaged back layer for the time of encounter with projectile along the way. Furthermore, these supplemented layers attenuate the tensile and compressive wave amplitudes generated after the first rebound of impactor at the very initial phase of the impact. Therefore, it could not be unreasonable to deliver the opinion that tensile stress-based delaminations and compressive stress-originated micro / macro cracks are likely to be cut down to some degree. However, these additional layers exert considerable thickness to the armor system. In design point of view, this system may require reassessing when there is a restriction of vacancy where the armor would be applied.

Kacan and Elaldi [64] studied the possibility of replacement of ceramic as a intermediary layer with carbon fiber reinforced / epoxy composite layer. Their intention was to state whether this replacement could yield better results, and therefore, be more economic as ceramic production is costly. During the experiment phase of their study, they made some shots against fiber reinforced / epoxy composite layer sandwiched with armor steel plates. At the end of shots realized in accordance with Stanag 4569 KE-4, it was observed that a composite armor consisting of metal cover and back plates and a carbon fiber reinforced /epoxy layer can yield lesser areal density figures compared to RHA to fulfill the aforementioned standard protection level requirements. Another observation of the authors was of significance: unidirectional fiber orientation might change the direction of the projectile waning the localization of the event.

As it is easily comprehensible from the above-mentioned publications and its deductions, there is still controversy in the realm of armor design and evaluation. The interaction of the variables like material properties such as hardness and strength, ratios of layer thicknesses, ductility and toughness, layering vs. monoblock plates, etc. are still obliged to be subjected to further exploration. This thesis is in the aim of treating some of them through numerical models and experiments.

1.5. Objective

Objective of this thesis is to shed a light on the findings that have remained contentious as they bear different outcomes to similar inputs, disclaiming somehow that this study would put an end to all of the discrepancies therefrom.

After setting this objective, the primary work to carry out is establishing what the contentious are. Therefore, the disputed topics the author would like to study are:

- the optimum thickness ratio (range) between ceramic and backplate,
- the ceramic material itself: density and toughness,
- the so-called added value of metal strength: the better performance means the more strength or ductility the metal would have,
- the effect of layering on backplate,
- the so-called added value of strength / ductility on layered armor plates used for backplate,
- the effect of layer thickness optimization for layered backplate,
- the effect of ceramic-metal-ceramic-metal lamination (not seen as much in literature),
- *the effect of layering on ceramic,*
- *the effect of layering on coverplate,*
- *the effect of spacing.*

Last three disputed areas were only tested on numerical environment.

1.6. Projectile Definition and Geometry

Projectile used in this study is a 12,7 x 99 mm steel core-AP projectile. The real dimensions of this projectile could easily be found in the literature or via a regular search on the web. Some of them are already available in Table 1.2. For the components and dimensions adapted into numeric environment, please see the Figure 1.18. below.

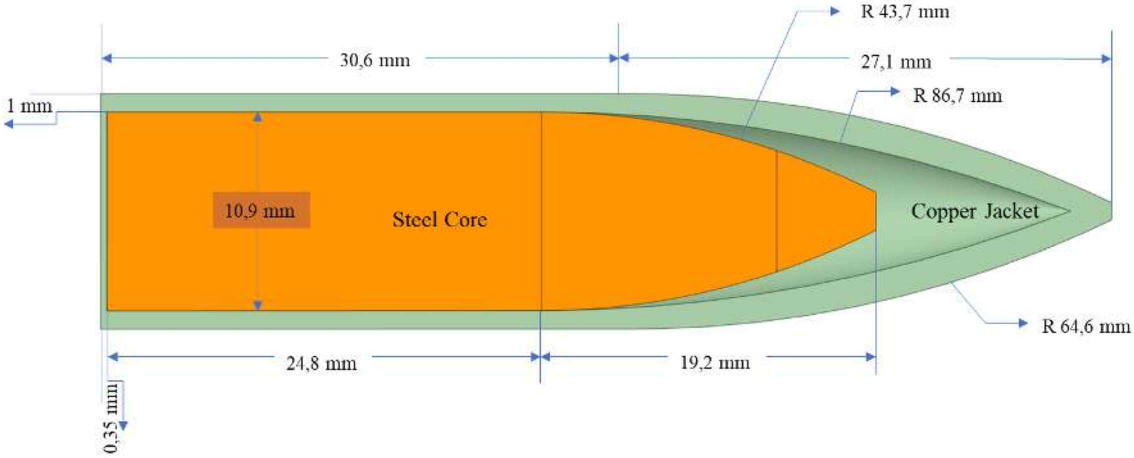

Figure 1.18. 12,7 projectile dimensions for numeric study.

For comparison of our numeric projectile dimensions with that of real world one, please see the Table 1.2. below.

Table 1.2. Comparison of real world and numeric projectiles.

	Projectile Length	Projectile Diameter	Projectile Mass	Core Length	Core Diameter	Core Mass
Real-case	*58,7 mm*	*12,98 mm*	*45,9 g*	*45,9 mm*	*10,9 mm*	*25,9 g*
Numeric	*57,7 mm*	*12,9 mm*	*45,6 g*	*44 mm*	*10,9 mm*	*26,3 g*

As seen from the table, the geometric alterations made to overcome modelling difficulties (see Chapter 3 for what they are.) are of minor figures.

The ammunition used in experiments is set out below in the Figure 1.19.

Figure 1.19. 12,7 x 99 mm steel core - AP projectile.

1.7. Target Configurations

The configurations were designed so that the objectives in the section 1.5. would easily be targeted. Within this aim, 12 discrete configurations were contemplated. The findings were thought to be compared to obtain quantitative and qualitative results after conducting experiments. One to three samples were manufactured for each configuration. These configurations will constitute a base upon which extensive numerical analyses depend. The configurations designed for experiments are submitted below in the Table 1.3. Layers in the table are arrayed in a way that reader can discover the material, and its thickness in millimeters in the same column.

The configurations designed for numerical analyses are given below in the Table 1.4. The first twelve are the same as the configurations for the experiments. Nevertheless, the thicknesses of layers are all different to keep the areal density same. Throughout the commentaries on numerical analyses (Chapter-3), fixed areal density for all configurations will constitute a benchmark permitting the researcher to evaluate respective performances of the targets in a controlled test environment

Table 1.3. Configurations for experiments.

Configurations	Layer-1		Layer-2		Layer-3		Layer-4		Layer-5		Total Thickness (mm)	Areal Density (kg/m^2)
1	S	8	Al_2O_3	10	Al	19,05					37,05	151,5
2	S	8	Al_2O_3	10	S	8					26	163,2
3	S	8	SiC	9	S	8					25	149,3
4	S	8	Al_2O_3	10	S	8	Al	8			34	184,5
5	S	8	Al_2O_3	10	Al	8	S	8			34	184,5
6	S	8	Al_2O_3	10	Al	12,7	Al_2O_3	10	Al	12,7	53,4	206,8
7	S	8	Al_2O_3	10	Al_2O_3	10	Al	12,7	Al	12,7	53,4	206,8
8	S	8	Al_2O_3	10	Al_2O_3	10	Al	8			36	160,5
9	Al	19,05	Al_2O_3	10	S	8					37,05	151,5
10	S	8	Al_2O_3	10	Al	8	Al	8	Al	8	42	164,6
11	S	8	Al_2O_3	10	Al	8	Al	19,05			45,05	172,8
12	Al	19,05	Al_2O_3	10	Al	19,05					48,1	139,7

S : armor steel.
Al_2C_3 : alumina.
SiC : silicon carbide.
Al : aluminum.

Table 1.4. Configurations for numerical analyses.

Configurations	Layer-1		Layer-2		Layer-3		Layer-4		Layer-5		Layer-6		Layer-7		Total Thickness (mm)	Areal Density (kg/m^2)
1	S	8	Al_2O_3	10	Al	22,05									40,05	
2	S	8	Al_2O_3	10	S	7,7									25,7	
3	S	8	SiC	16,5	S	7,7									32,2	
4	S	8	Al_2O_3	10	S	5,7	Al	5,7							29,4	
5	S	8	Al_2O_3	10	Al	5,7	S	5,7							29,4	
6	S	8	Al_2O_3	6,8	Al	8,6	Al_2O_3	6,8	Al	8,6					38,8	
7	S	8	Al_2O_3	6,8	Al_2O_3	6,8	Al	8,6	Al	8,6					38,8	
8	S	8	Al_2O_3	10	Al_2O_3	10	Al	8							36	
9	Al	22,5	Al_2O_3	10	S	8									40,5	
10	S	8	Al_2O_3	10	Al	7,5	Al	7,5	Al	7,5					40,5	160,6 ± 0,25
11	S	8	Al_2O_3	10	Al	7,5	Al	15							40,5	
12	Al	23	Al_2O_3	10	Al	23									56	
13	S	8	Al_2O_3	20	Al	8									36	
14	S	8	Al_2O_3	5	Al_2O_3	5	Al_2O_3	5	Al_2O_3	5	Al	8			36	
15	S	4	S	4	Al_2O_3	10	S	7,7							25,7	
16	S	2	S	2	S	2	S	2	Al_2O_3	10	S	7,7			25,7	
17	Al	11,5	Al	11,5	Al_2O_3	10	Al	23							56	
18	Al	5,75	Al	5,75	Al	5,75	Al	5,75	Al_2O_3	10	Al	23			56	
19	Al	22,5	Al_2O_3	10	S	2	S	2	S	2	S	2			40,5	
20	S	8	Al_2O_3	10	Al	4,5	Al	4,5	Al	4,5	Al	4,5	Al	4,5	40,5	

Table 1.4. Continued.

Configurations	Layer-1		Layer-2		Layer-3		Layer-4		Layer-5		Layer-6		Layer-7		Total Thickness (mm)	Areal Density (kg/m^2)
21	S	8	Al_2O_3	13,6	Al	17,2									38,8	
22	S	4	-	4	S	4	Al_2O_3	10	Al	22,5					40,5	
23	S	8	-	8	Al_2O_3	10	Al	22,5							40,5	160,6 ± 0,25
24	Al	11,5	-	11,5	Al	11,5	Al_2O_3	10	Al	23					56	
25	Al	23	-	23	Al_2O_3	10	Al	23							56	

S : armor steel. Al_2O_3 : alumina. - : SPACE.

SiC : silicon carbide. Al : aluminum.

2. HIGH VELOCITY IMPACT PHENOMENON

High velocity impact is a dynamic phenomenon [62]. The materials used cannot respond to the load applied on them as they do in quasi-static situations. Therefore, some equations of state (EOS), strength and failure models [29], which will be covered in detail in chapter 3, need to be developed to fully understand the response mechanism.

Stress wave propagation is a profound aspect of any dynamic process such as impact events. Impact events usually span a very minute time range of 0,001-0,0001 s [29]. During such a short time, material may not be able to find time to react the action with its entire atoms. Because the effect of the impact, shock waves, might not be felt in some remote parts of the material [65]. This feature makes the impact phenomena highly transient. Most of the time, the assumption of uniaxial strain [32], [66], [67] is sufficient for a good cause, which is that radial boundaries cannot find time to respond. This approach is going to be accepted in this work as well.

For above-mentioned reasons it seems to be indispensable to walk over some key aspects such as stress wave propagation appearing in an impact event.

2.1. Wave Propagation

Basically, in an impact, elastic [(longitudinal, shear and Rayleigh), (see Figure 2.1.)], plastic and shock waves are generated. The elastic portion of the deformation for metals with lower dynamic yield strength might be neglected in some situations as the slope in one dimensional stress-strain curve exceeded in most high velocity conditions (to be covered later in the subsection 2.1.3.) [68]. However, for materials with higher dynamic yield strength such as ceramics, elastic waves take on a more predominant role as they are the determinants of ceramic-metal interface fracture or failure (to be covered later in the subsection 2.2.2.).

2.1.1. Elastic waves

Elastic waves are the waves that do not generate permanent deformation on the material. These waves exist in steady-state conditions (or for strain rates below 10000/s [55]), where the involved materials do have time to relay the exerted force as a momentum to one another through their atoms. Because the application time of the forces are assumed to be greater compared to the duration taken by this imparting mechanism in most cases, the variable (i.e.: spread of stress) could be revealed using rigid bodies if deformation is not to be monitored; even though nothing could be supposed to be a part of rigid body dynamics in real world conditions. In rigid body dynamics, an action is felt at the other portion of the material, which is not subjected to external force directly, with zero-time delay.

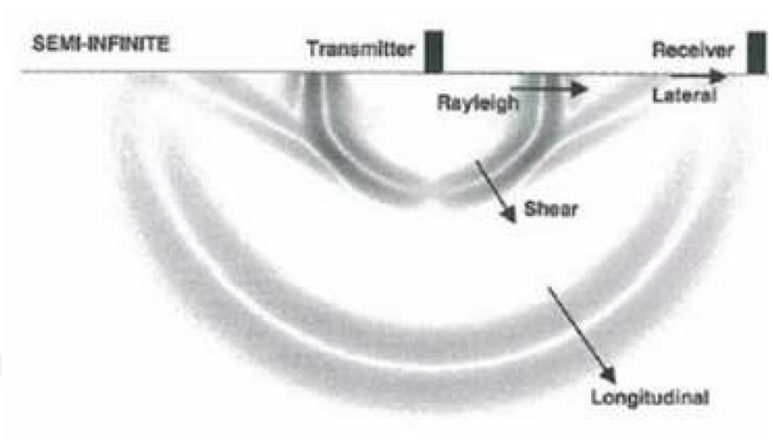

Figure 2.1. Elastic waves [68].

In uniaxial stress condition with no shear assumed (see Figure 2.2.), for a rod diameter of which is pretty small compared to its length, elastic wave speed can be derived through one dimensional stress equation of motion:

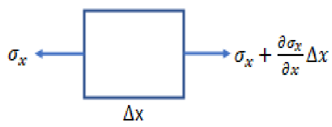

Figure 2.2. Uniaxial stress equation of motion.

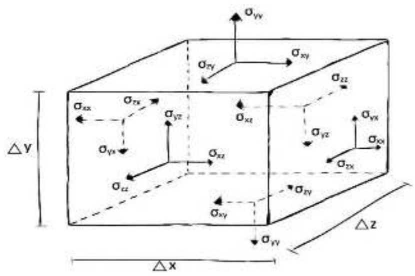

Figure 2.3. Three-dimensional stress components.

$$\sigma = m.\ddot{u}.\frac{1}{A} \tag{2.1}$$

$$\left(\sigma_x + \frac{\partial \sigma_x}{\partial x}\Delta x\right) - \sigma_x = \rho.\Delta x.\ddot{u} \tag{2.2}$$

$$\boldsymbol{\frac{\partial \sigma_x}{\partial x} = \rho.\ddot{u}} \tag{2.3}$$

$$\frac{\partial}{\partial x}\left(E\frac{\partial u}{\partial x}\right)=\rho\frac{\partial^2 u}{\partial t^2} \tag{2.4}$$

$$\frac{\partial^2 u}{\partial t^2}=\frac{E}{\rho}\frac{\partial^2 u}{\partial x^2} \tag{2.5}$$

where *E*: elastic modulus, *ρ*: density, *u*: displacement, *m*: mass, *A*: area. When compared equation (1.14) with equation (2.5), it is found that elastic wave speed for a beam is:

$$c=\sqrt{\frac{E}{\rho}} \tag{2.6}$$

From the Hooke's elasticity law for three-dimensional case, the relationship matrix between principal stresses and strains is obtained:

$$\begin{bmatrix}\sigma_x\\ \sigma_y\\ \sigma_z\end{bmatrix}=\frac{E}{(1+v)(1-2v)}\begin{bmatrix}(1-v)\varepsilon_x+v(\varepsilon_y+\varepsilon_z)\\ (1-v)\varepsilon_y+v(\varepsilon_x+\varepsilon_z)\\ (1-v)\varepsilon_z+v(\varepsilon_x+\varepsilon_y)\end{bmatrix} \tag{2.7}$$

where *v*: Poisson ratio, *ε*: normal strain. For uniaxial strain case, $\varepsilon_y=\varepsilon_z=0$, it boils down to:

$$\sigma_x=\frac{(1-v)E}{(1+v)(1-2v)}\varepsilon_x=\left(K+\frac{4}{3}G\right)\varepsilon_x \tag{2.8}$$

$$c=\sqrt{\frac{E(1-v)}{\rho(1+v)(1-2v)}}=\sqrt{\frac{K+\frac{4}{3}G}{\rho}} \tag{2.9}$$

where *K*: bulk modulus and *G*: shear modulus.

For the three-dimensional case, stress equations of motions including shear stresses this time (see Figure 2.3.) could be written as:

$$\boldsymbol{\frac{\partial\sigma_x}{\partial x}}+\frac{\partial\tau_{xy}}{\partial y}+\frac{\partial\tau_{xz}}{\partial z}=\boldsymbol{\rho}.\ddot{u}_x \tag{2.10}$$

$$\frac{\partial\tau_{yx}}{\partial x}+\frac{\partial\sigma_y}{\partial y}+\frac{\partial\tau_{yz}}{\partial z}=\rho.\ddot{u}_y \tag{2.11}$$

$$\frac{\partial\tau_{zx}}{\partial x}+\frac{\partial\tau_{zy}}{\partial y}+\frac{\partial\sigma_z}{\partial z}=\rho.\ddot{u}_z \tag{2.12}$$

where body forces and accelerations are zero and $\ddot{u}_{x,y,z}$ are principal accelerations. When equation (2.3) and (2.10) are compared, bold figures stand out as common terms.

Finally shear and Rayleigh wave speed formulas are:

$$c_s = \sqrt{\frac{G}{\rho}} \tag{2.13}$$

$$c_r = \frac{0,862 + 1,12.v}{1 + v} c_s \tag{2.14}$$

where c_s: shear wave speed and c_r: Rayleigh wave speed. If the last two equations are utilized to find out whether boundary conditions (distance between radial free edge and impact center on a plate) are significant or not, one may realize easily that the indicated distance is not needed to be more than a couple of projectile diameters. Therefore, most high velocity impact events are assumed to be uniaxially strained: relief waves generated cannot find time to travel back to impact site before penetration or perforation is accomplished.

2.1.2. Plastic waves

Plastic waves are the waves which generate permanent deformation. They are encountered in steady state and dynamic conditions. These waves appear when the stress in the material surpass the yield strength of the material. In steady state cases, the slope of the stress-strain curve decreases after that strength. This decreasement is due to relative increasement in strain compared to stress (see Figure 2.4.).

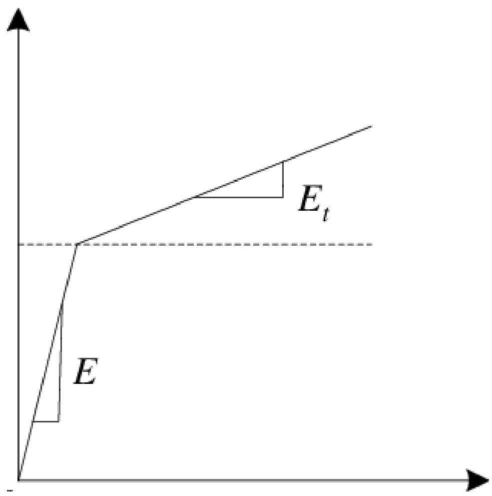

Figure 2.4. Elastic-linear strain hardening material σ-ε curve.

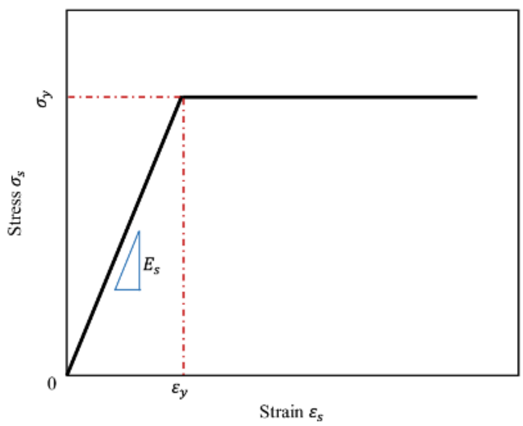

Figure 2.5. Elastic-perfectly plastic material σ-ε curve.

For materials having a stress-strain curve as it is in Figure 2.5., the plastic wave speed wanes with the elastic modulus diminution to tangent modulus, E_t, proportionally. For these kinds of materials:

$$c_p = \sqrt{\frac{E}{3\rho(1-2v)}} = \sqrt{\frac{K}{\rho}} \tag{2.15}$$

Since elastic modulus is lowered to bulk or tangent modulus in the plastic region, it goes without saying that elastic wave speed is higher than plastic wave speed in quasi-static conditions, which will be overturned in the next subsection.

2.1.3. Shock waves

Shock waves show up in dynamic situations only. It happens when the instant stress level is well above the material dynamic yield strength. In such a situation, shear stresses become negligible, adiabatic conditions develop, no elastic behavior involves [65].

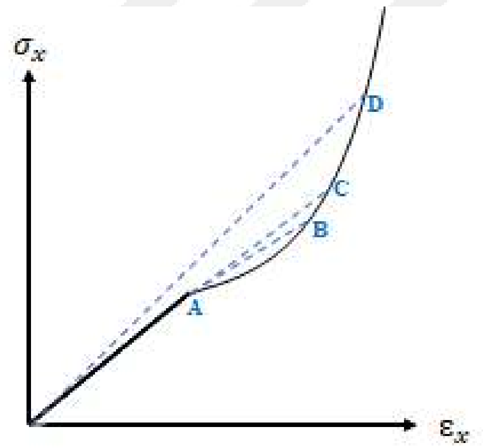

Figure 2.6. Stress-strain curve under dynamic uniaxial strain conditions [69].

In Figure 2.6., point A is the material yield strength in dynamic situations, HEL. For stress levels above the point A, for example at the point B or between [BC], elastic and plastic waves come into being, elastic wave being the precursor. The intensity of the plastic wave is calculated according to the [AB] slope. If the stress developed is at the point C plastic wave speed catch up on the elastic precursor, both having the same slope and speed. Finally for stress levels above the point C, shock waves emerge only (no elasticity accompanying) and it travels corresponding to its slope relative to origin. As it seen from Figure 2.6., for higher pressure levels above the point C, shock wave velocity is changeable. That means bulk modulus of the material, *K*, gets subjected to change from that level onwards. Generally, the pressures above the point C equates to the values over 10 GPa [28].

There is found necessary to expose the derivations of conservation laws for shock velocity-involved conditions. Conservation of mass can be expressed as:

$$\rho_0 . U_s = \rho_1 . (U_s - U_p) \tag{2.16}$$

where the subscript *1* define the instantaneous density at any time on the course of impact, U_s: shock wave velocity, U_p: particle velocity accelerated.

The stress level of a particle that shock wave sweeps on its path can be derived by:

$$F = m . \ddot{u} \tag{2.17}$$

$$F . dt = m . \dot{u} \tag{2.18}$$

$$\sigma_i . A . dt = \rho . A . dx . \dot{u} \tag{2.19}$$

$$\sigma_i = \rho \frac{dx}{dt} \dot{u} = \rho U_s U_p \tag{2.20}$$

where $\dot{u}=U_p$: particle velocity. This is the expression for the conservation of momentum.

Finally, the conservation of energy may be uttered as:

$$e_1 - e_0 = \frac{1}{2} \sigma_i \left(\frac{1}{\rho_0} - \frac{1}{\rho_1} \right) \tag{2.21}$$

where e: specific energy, energy per unit mass, and σ_i: hydrostatic energy.

Equation (2.16), (2.20) and (2.21) are known as Rankine-Hugoniot equations. If a relation between the two variables among shock velocity, particle velocity, internal energy, hydrostatic stress and density *(Us, Up, e,* σ_i*, ρ)* could be created through an additional equation, then the pressure and internal energy of a particle can be calculated. Just as it will be presented in subsection 3.2.1., such a relation could be created in a number of ways.

2.2. Failure Mechanisms

There have been many studies over time to understand the main failure mechanisms of armor systems to reach a certain capacity in protectiveness. However, it could be a challenging toil of work. The failure mechanisms are so varied for both ceramics and metals that are used in armor systems in concordance with their material properties such as hardness, dynamic yield strength, ductility etc. However, in order to remain within the track of this thesis, it is objected to investigate the damage modes of multilayered composite armors, constituents of which are a metal cover layer, a hard ceramic layer and a supportive metal back layer. However, brief account for projectile failure is provided below before that of target.

2.2.1. Projectile failure

From the point of this thesis, it seems evident from many publications that the deformation amount for ogival projectiles is negligibly small [35], while it is considerably higher for blunt projectiles [31]. The high resistance to deformation of ogival projectiles can be attributed to the perforation mechanism assumed and experienced to be involved: ductile hole growth [51]. As for blunt projectiles, this resistance is decreased by the shear of target and the higher global deformation mechanism of target that comes along.

Again, from the orientation of this study, there is anticipated no projectile fracture or bending deformation as no bending stresses will be available (see Figure 2.7.) exerted upon it. Because oblique impact is out of consideration in this study. Thus, a conservative approach is aimed to be gained by normal impact case.

Any information as to numerical modelling of the projectiles that were used in the ballistic tests of this thesis is allocated for section 3.4.

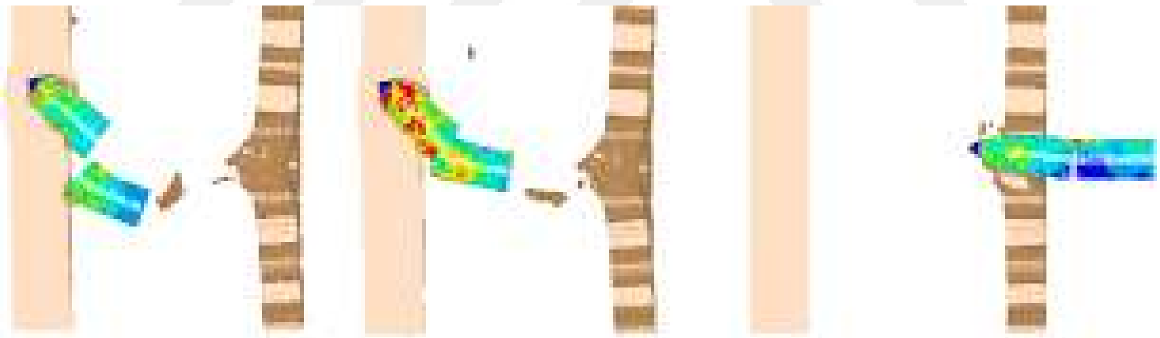

Figure 2.7. Projectile fracture through bending due to a preliminary perforated plate [28].

2.2.2. Target failure

Failure mechanisms on targets vary with regard to their material properties such as ductility and strength, being multilayer or monoblock structures, configured in contact or air gap between them if multilayered, their thickness, configured in a composite or standalone armor systems, projectile impact velocity etc. Main failure modes are in Figure 2.8.

To address multilayer targets in concise before proceeding for details, these structures show up as armor systems with low bending stiffness relative to that of monoblocks. This could be helpful to exploit more energy from the projectiles since more portions of material in the radial direction contribute to the resistance by bending, if the layer number is scarce. However more layers mean increasingly low stiffness causing premature perforation at the end [53].

Metals

Ductile materials such as relatively low strength steels intend to bulge at the rear side before perforation. Some analytical models are present to calculate the energy absorbed based on the height of bulging [68]. Bulging level is directly related to the projectile diameter, nose shape and the material properties of the layer in question and ones before, if any. For example, thick ceramic layers may disseminate the pressure of projectile to a larger surface at the ceramic-metal interface due to the expanding cone angle. Thus, that time, bulging height and radial span become evident. Otherwise, especially at high velocities, damage localizes and petalling outrace bulging.

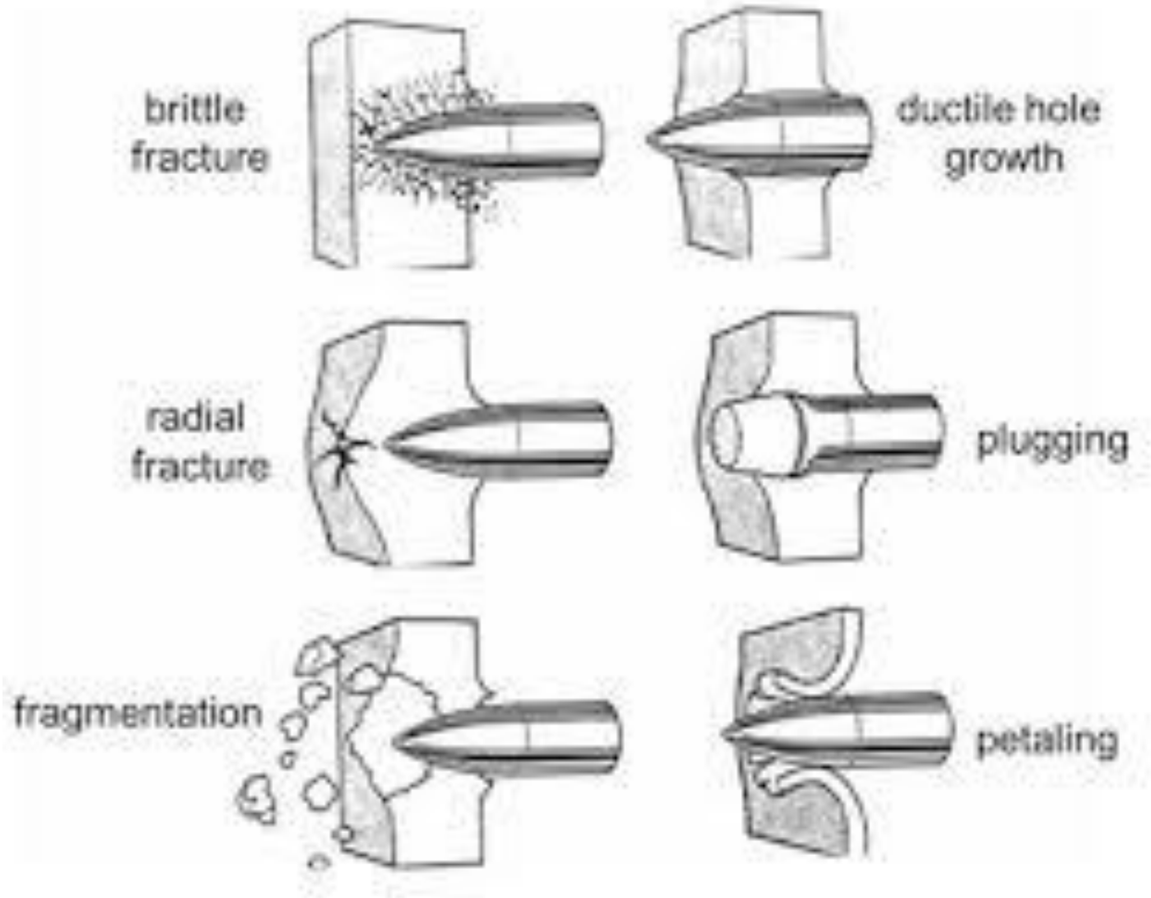

Figure 2.8. Failure modes in general [70].

Dishing could be said to be a special shape of bulging with more area of global deformation involved. Global deformation is relatively higher for ductile materials and multilayered structures. The former suck in more energy and the latter has lower stiffness (see Figure 2.9.).

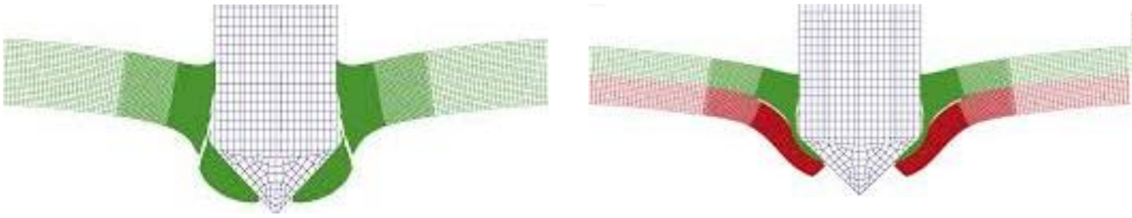

Figure 2.9. Global deformation on ductile and multilayered target impacted by ogival blunt projectiles [49].

High strength, high hardness materials are generally used as the first interface against projectiles to increase impact angle, to cause ricochet, if possible, and hence reduce penetration capability. However, whether they are successful to defeat a projectile compared to a low density, highly ductile material of the same AD will be a subject of this study as well as their use together in multilayered structures. Indeed, ductile materials are good at energy absorbing by shear.

Thin armors are inclined to localize the effect of impact as they cannot exhibit enough inertia in such a short time.

Petalling is a tensile or shear tearing process that usually emerges in relatively high strength armors impacted by ogival projectiles. Since global deformation is lesser in this case, damage localizes, bulging that the petals lie over is more evident and sagging, height of bulging is more [37].

Spalling or fragmentation is a damage mode encountered when compressive waves formed by projectile reaching at the free face act as tensile waves while returning back. The result is the ruptured, splitted and detached armor pieces from the free surface. This phenomenon is more generally seen with harder materials. The shock waves surging from the tip of projectile can also induce spalling at the front face of the ceramic [28].

Plugging is a deformation mechanism confronted with blunt projectiles. While they are progressing through the target by shear, they tear and pluck off the relevant portions of target plates having approximately the same diameter of the projectile and the same thickness of their master armor plates.

The major failure mechanism for a brittle material of high compressive strength and hardness are radial and cone cracks. Cone cracks are each a product of propagating shock waves, and radial cracks are due to tensile waves at the free surface and bending (see Figure 1.17). More detail is allotted for the next subsection.

Ceramics

Ceramics are brittle materials. The ceramics that most appear in armor systems are alumina (aluminum oxide), silicon carbide, titanium bromide, boron carbide. They are used in armor systems as they display high compressive strength, such as in [46]. Additionally, thanks to their high hardness levels, they are capable to erode and decelerate projectiles. However, they are lacking tensile and bending strength, therefore need to be supported by metals mostly to maintain its compact structure under confinement during an impact (see Figure 2.10). Confinement is especially significant in multi-hit situations to decrease the area affected in an individual impact by narrowing down cone crack diameter, so spallation (see Figure 2.11) [61].

When an impactor gets into contact with ceramic layer / armor, it decelerates instantly thanks to the high compressive strength of ceramic. Secondly, projectile is eroded by irritating and pulverized ceramic that has formed in front of the projectile due to arising crushing pressure. As it goes further and erosion continues to take place, shock waves propagate through the ceramic armor creating a conoid formation of longitudinal cracks. Cross-section of the cone cracks start to take a trapezoidal shape, the longer edge expanding towards the free face of the ceramic. Later on, comminuted ceramic that cannot find a place to get out of projectile's way, leak into the apertures of cone cracks forming. Additionally, the backing material, if present, which cannot endure the increasing pressure, begin dishing and bulging, and in this way making more room for pulverized ceramic, and eroded projectile granules [46] to swarm into. After compressive waves reach the rear surface of ceramic, reflect back to confront projectile front and hence complement conoid formation. While these consecutive reactions are taking place, bending tensile stresses exerted on ceramic layer result in radial cracks at the rear face, especially when thicker adhesive layer is present at the interface [44]. Finally, the projectile goes further through the back metal, if present, and perforates it with a possible petalling damage mode.

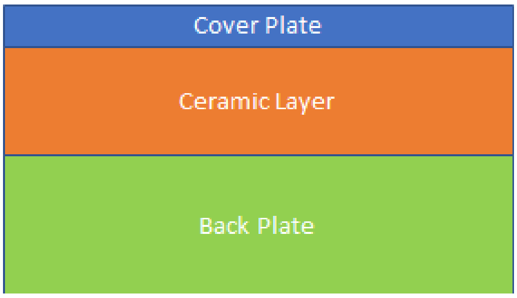

Figure 2.10. Typical ceramic-metal composite armor.

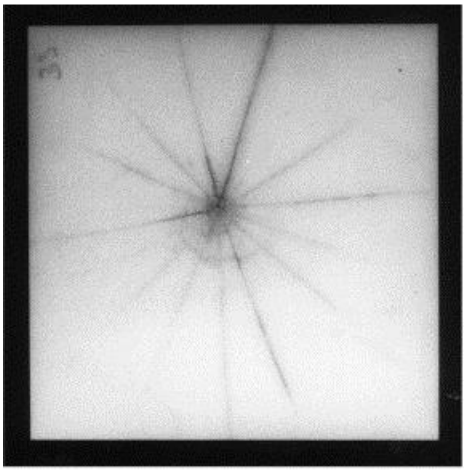

Figure 2.11. Indistinct and narrow cone at the bottom of ceramic layer [61].

As previously stated in wave propagation section, elastic waves are crucial to grasp the phenomenon behind this compressive-to-tensile transition at the backside of ceramic laminate. This cruciality is because they generate impedance mismatch at the interface. To make this impedance mismatch clearer, below is presented the relation of stress with particle and elastic wave velocity figures, U_p, c, the very similar one to the equation (2.20) with just one differentiation as we are dealing with elastic waves:

$$\sigma = \rho c U_p \tag{2.22}$$

The first two terms on the right side of the equation above denote impedance, I, of any material [44], [55]:

$$I = \rho \times c = \sqrt{\rho \times E} \tag{2.23}$$

Elastic stress wave propagation for interfaces with equal cross-sectional areas are:

$$\sigma_I + \sigma_R = \sigma_T \tag{2.24}$$

$$U_{pI} - U_{pR} = U_{pT} \tag{2.25}$$

where σ_I, σ_R and σ_T are incident, reflected and transmitted stresses, and U_{pI}, U_{pR} and U_{pT} are incident, reflected and transmitted particle velocities. When we express the terms on equation (2.25) with equation (2.22), we get:

$$U_{pI} = \frac{\sigma_I}{\rho_A c_A}, \qquad U_{pR} = \frac{\sigma_R}{\rho_A c_A}, \qquad U_{pT} = \frac{\sigma_T}{\rho_B c_B} \tag{2.26}$$

where ρ_A and ρ_B are incidence and transmitted wave medium densities, and c_A and c_B are incident and transmitted wave medium velocities. Later we put equation (2.26) into equation (2.25), we get:

$$\frac{\sigma_I}{\rho_A c_A} - \frac{\sigma_R}{\rho_A c_A} = \frac{\sigma_T}{\rho_B c_B} \tag{2.27}$$

Finally, when we consider equations (2.24) and (2.27) together, we get the stress relation generated by incidence, reflected and transmitted elastic waves:

$$\begin{aligned} \frac{\sigma_R}{\sigma_I} &= \frac{\rho_B c_B - \rho_A c_A}{\rho_B c_B + \rho_A c_A} \\ \frac{\sigma_T}{\sigma_I} &= \frac{2\rho_B c_B}{\rho_B c_B + \rho_A c_A} \end{aligned} \tag{2.28}$$

As we understand from the equations above, when the transmitted wave medium impedance happens to be greater than incidence wave medium impedance (rarely encountered), reflected stress has the same sign (positive) with incidence wave. For the opposite scenario (usually seen), we can expect some reflected stress waves to travel backwards from the interface [55]. Nevertheless and already, continuum could not be maintained on interfaces of armor laminates as adhesives or air between them generates discontinuities, which in turn, creates negative-signed reflected waves. Eventually, if this discontinuity is large or impedance mismatch is high, ceramic fractures due to reflected (tensile) waves.

But even after fracture, comminuted ceramic that are confined has also a strength. They aggravate the projectile digging further. In addition, due to its hardness, pulverized material continues eroding the tip of the projectile by high frictional force.

Conoid formation is an asset for distributing the pressure over a large area on the ceramic-metal interface which is a good thing in terms of the performance of backing metal and of course, of the entire armor system. Nevertheless, while projectile is progressing in ceramic, conoid base radius gets smaller [31]. This means more localized pressure for back metal to stand against. It is indeed the basic reason of back metal deflection and failure afterwards.

Cone and radial cracks are the main failure mechanisms for ceramic plates as touched upon previously. Generally, one of them is more effective on the failure. Shock waves are faster than the projectile tip, therefore radial cracks precede cone cracks, and as a result fracture starts from the bottom in thin plates. On the contrary, for thick plates, tensile waves may weaken through the thickness up until they reach the bottom to generate radial cracks, thus cone cracks may be predominating failure factor [61]. Additionally, it is also said that the subject of whether the cone or radial cracks precede one another, and cause failure is related to the backplate thickness as well according to the findings in [62].

Ceramic production techniques (i.e., hot pressed or pressed only), additives used in production, microstructure etc. are also significant both in strength and failure of ceramics, which are out of consideration of this study.

3. NUMERICAL MODELLING

Numerical analyses are carried out using AUTODYN™ software, which was first developed by Century Dynamics in 1986, embedded in Explicit Dynamics modulus in ANSYS® commercial numerical analysis tool. AUTODYN™ software is a finite element, volume and difference multi-processor that can treat different domains in a problem, e.g., fluids, gasses, solids, and couple them (contacts, interactions included) in space and time to reach a solution. Some schemes to depict these domains in are given in subsection 1.3.2. Some applicable problem areas are given below:

- impacts,
- explosions,
- bird strike,
- accident simulation,
- jet and missile exposure,
- study of stress and shock waves,
- constitutive model development [29].

3.1. Lagrange Processor and Time Integration

Explicit Dynamics modulus in ANSYS® is a special module to simulate non-linear, short time span, dynamic events. There is no need to invert stiffness matrix to elicit displacements for this solution method unlike the case of implicit solvers: convergence is guaranteed unless time step is gotten too small (see equation 3.1.) when erosion criteria in analysis do not conform the plasticity or failure model (see section 3.2.), or energy loss happens to emerge mostly because of false contact definitions. It incorporates explicit time integration (mentioned briefly in section 1.3.) for accuracy. Explicit time integration (also known as Courant-Friedrichs-Lewy Integration condition) is based on the formula:

$$\Delta t \leq f.\left(\frac{h}{c}\right)_{min} \tag{3.1}$$

where Δt: time step, f: safety factor [a number between (0-1)], h: element characteristic length regarding its inertia, and c: element sound speed (see equations 2.6, 2.9, 2.15). As it is seen from the equation, processor ensures that the stress wave cannot travel more than one element in one time step. Safety factor does even restrict the distance a stress wave can cover in a time step. Additionally, time step is inversely proportional to elastic modulus of constituents. As stated previously in section 1.3., this type of time integration may stretch out simulation time for highly non-linear, shock wave and high element distortion-involved cases. When element distortion is high, characteristic length of the element decreases yielding smaller time steps [39].

In the numerical analyses in this thesis, Lagrange solver is used. Explicit solver employs central difference time integration scheme (Leapfrog Method). In this method, the followings are applied in order (see Figure 3.1.):

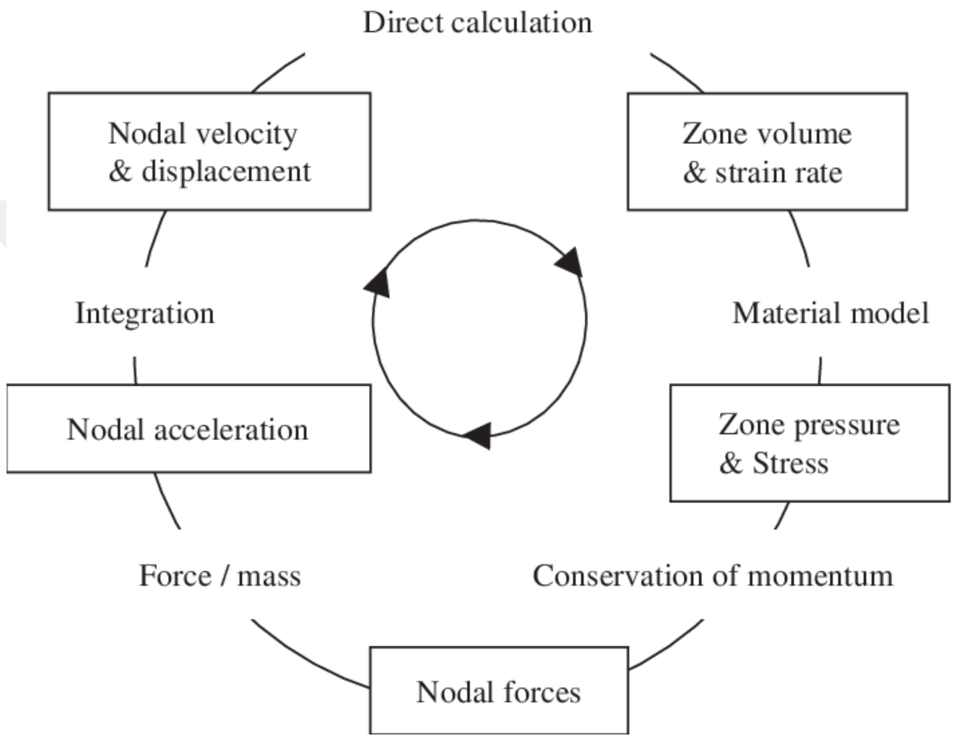

Figure 3.1. Lagrange explicit computation cycle [29].

- According to the initial and boundary conditions of the problem; nodal forces, stress and strain figures are calculated and assigned onto each node. If it is one of intermediate cycles, the displacement, velocity and acceleration figures of the cycle one before is used and the equation is:

$$[M].\ddot{u} + [C].\dot{u} + [K].u = [F] \tag{3.2}$$

where $[M]$: mass matrix, $[C]$: damping matrix, $[K]$: stiffness matrix.

- Nodal accelerations are computed by the equation:

$$\ddot{u} = \frac{F}{m} + b \tag{3.3}$$

where b: body acceleration -available when a body force is present, possibly due to gravitational force or magnetic field.

- Nodal velocities and displacements are computed by integration:

$$\dot{u}^{t+\Delta t} = \dot{u}^{t} + \int_{t}^{t+\Delta t} \ddot{u} . dt \tag{3.4}$$

$$u^{t+\Delta t} = u^{t} + \int_{t}^{t+\Delta t} \dot{u} . dt \tag{3.5}$$

- From the nodal displacements, new locations of nodes are computed. From these new locations, volumes of elements and total structure, strain rates are determined.

- Stress (deviatoric) and pressure (hydrostatic) figures (covered in next section) are determined through material models, i.e., EOS, strength and failure formulations, in which strain rates are generally an input [29], [39].

3.2. Material Modelling

Material models that describe the properties and behaviors of materials in a dynamic impact analysis is of ultimate importance. Because sound description of material behavior under impact yields the best results and depiction of failure mechanisms as close to real phenomena as possible.

To efficiently model a constituent in a numerical analysis, three modelling formulations are necessary, which are strength, failure and EOS formulations.

Stress tensor could be expressed as a combination of *hydrostatic stress*, in which a mean value of principal stresses is taken, and *deviatoric stress* that creates change in shape, namely, distortion in constituents (see Figure 3.2.). EOS and strength model treats these respectively.

EOS formulations relate state variables to each other; such as pressure, volume, density, temperature and internal energy. These formulations, which manage material behavior when it is under hydrostatic or hydrodynamic stresses (EOS formulations do not necessarily be deducted from dynamic cases, however it is better for obtaining material behavior in those situations), could be linear or non-linear. In dynamic cases such as high velocity impacts involving shock waves and high strain rates, drastic pressure increasement and relevant density augmentation in a short duration is as usual. For example, in the numerical analyses, while % 5 density increasement at most was encountered for metals, that figure couldn’t go beyond ‰ 8 for ceramics, within this study. For these situations, it is appreciable to utilize non-linear equations of state formulations to best describe pressure change.

Strength models, which consist of constitutive relations between material static yield strength, strain, strain rate, temperature etc., are utilized to calculate stress tensor that are accumulated on the material (on elements specifically). They are needed if deviatoric stresses are likely to be present in plastic region, namely, material resistance to shear distortion is applicable to the problem in question.

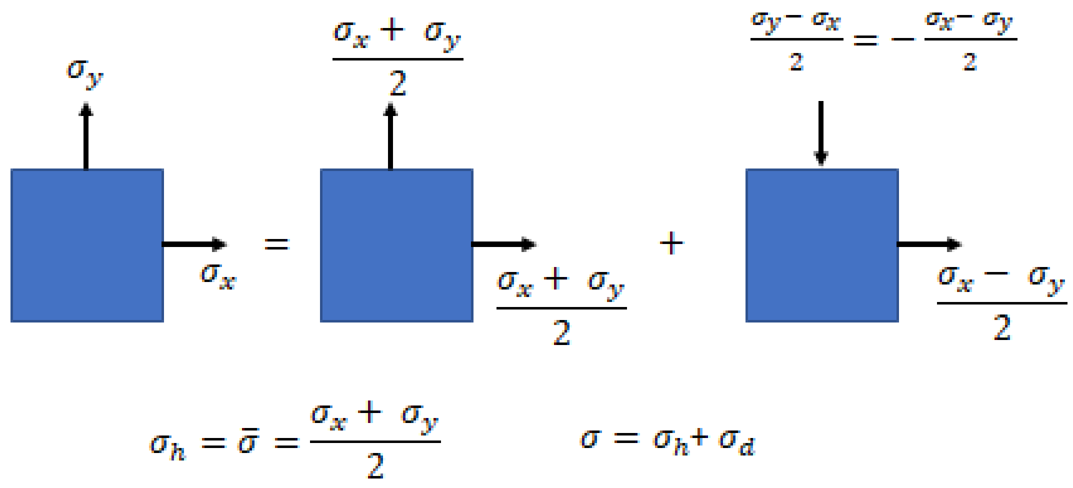

Figure 3.2. Two-dimensional stress tensor *[σ_x, σ_y]* demonstration only with principal stresses: hydrostatic and deviatoric stresses.

Failure models incorporated into the analysis decide on when to erode an element that would experience predetermined figures of plasticity, temperature, geometric shape change, element time step (see subsection 1.3.2.) etc. In this study, main emphasis will be put into eroding elements in accordance with the accumulated strain on them. As it is obvious, yield and ultimate failure stress figures which are outputs of uniaxial stress experiments set up in quasi-static strain rate conditions are no longer applicable for events that involve material response in dynamic situations. For instance, numerical analyses showed in this study that a maximum strain rate of 4 x 10^6 was attainable. Therefore, failure models that orient from total strain energy or deviatoric strain energy in quasi-static conditions, such as *Maximum Strain Energy Theory* and *Maximum Distortion Energy Theory* that are based on constant strength figures on the ongoings of an event, are not utilizable in dynamic situations [71].

The material models that are made use of in the thesis are sorted below mentioning why and how they are advantageous.

3.2.1. Equation of state

As stated before, EOS is necessary to account for hydrostatic stress component of stress tensor. An equation of state should be enough to cover all the hydrostatic pressure range that can occur in a material for a particular problem to accurately predict and provide a basis for failure mechanisms. Even if an impact phenomenon is mostly compressive in nature, reflected waves from the contact regions or relief waves are tensile. Thus, a sufficient EOS must be able to encompass minimum pressure figures too.

In this study, as we are engaged in solids -though impact region could count as an adiabatic region with zero shear modulus- EOS for solids must be employed in the study.

First EOS to consider is linear equation of state formulated as:

$$\mathrm{P} = \mathrm{K}.\mu \tag{3.6}$$

where P: pressure, μ: volumetric strain which equals to $(\rho/\rho_0 - 1)$ where ρ_0: initial density. This EOS is used where moderate pressures are likely to be produced. According to some authors, only moderate pressure levels are attainable for impacts substantiated at strike velocities of 0,5-2 km/s [14], [72].

Second EOS is to mention is shock EOS linear and shock EOS quadratic. Previously in subsection 2.1.3, Rankine-Hugoniot equations that deliver mass, momentum and energy conservation in dynamic situations were uttered -which make a connection between density, hydrostatic pressure, shock and particle velocity, and internal energy. There was made a conclusion that there could possibly be made a relation between the two of any variables mentioned to extract all the five variables. From the experiments, mostly from high velocity flyer plate impact experiments such as in [73], it is proved to be a linear or quadratic relationship between shock and particle velocity [39]. These equations are:

$$\mathrm{U_s} = \mathrm{c} + \mathrm{s_1}.\mathrm{U_p} \tag{3.7}$$

$$\mathrm{U_s} = \mathrm{c} + \mathrm{s_1}.\mathrm{U_p} + \mathrm{s_2}.\mathrm{U_p^2} \tag{3.8}$$

where s_1 and s_2: experimental slopes of shock velocity to particle velocity. These flyer tests are also used to determine material constants in some material models such as Johnson – Holmquist strength model (see section 3.2.3.).

It is also obligatory to introduce Mie Grüneisen coefficient, or say, gamma. This coefficient relates change in pressure to change in internal energy at constant volume, namely:

$$\Gamma = v.\left(\frac{dP}{de}\right)_v \tag{3.9}$$

where Γ: Mie Grüneisen parameter, v: specific volume, volume per unit mass which is 1/ρ. By this parameter, relation of pressure change to internal energy change through shock hugoniot curve (see Figure 3.3.) could be conducted:

$$P_1 - P_0 = \frac{\Gamma}{v}(e_1 - e_0) \tag{3.10}$$

where $P_0 = -\frac{de_0}{dv}$.

After some analytical derivations to find P_1 *and* e_1 and assuming *Γ/v*: constant, equation (3.10) become:

$$\frac{\rho.c^2.\chi}{(1 - s_1.\chi)^2} + \frac{de_0}{dv} = \frac{\Gamma}{v}\left(\frac{P_1\chi}{2.\rho_0} - e_0\right) \tag{3.11}$$

where $\chi = 1 - \frac{\rho_0}{\rho} = 1 - \frac{v}{v_0}$.

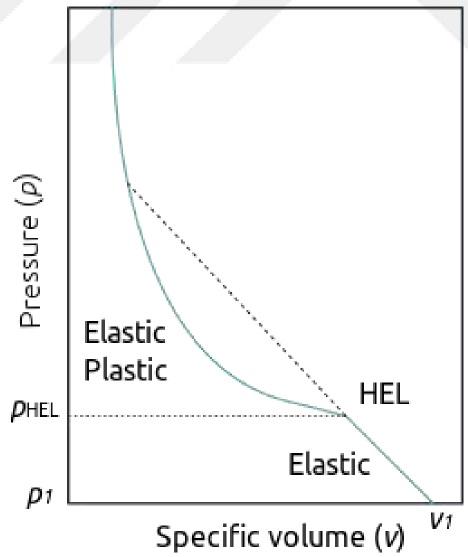

Figure 3.3. Shock hugoniot curve.

Third EOS to deliver is shock EOS bilinear. For higher compression levels, assumption that Γ/v is constant does not hold. For these situations to compensate the accuracy, in order to describe the relationship between shock and particle velocity, two separate curve fits could be used for adjacent regions of pressure: one for lower shock compression region ($v>v_B$), one for higher shock compression region ($v<v_E$), where v_B and v_E are the boundaries of the

area that specific volume figures are expected to range within. The first relationship is the same as equation (3.7). The second one is:

$$U_{s2} = c_2 + s_2 . U_p \tag{3.12}$$

Finally, the resultant shock wave velocity is:

$$U_s = \frac{(U_{s2} - U_{s1})(v - v_B)}{(v_E - v_B)} \tag{3.13}$$

Mie Grüneisen parameter is an input to EOS formulation along with the values of selected EOS: either linear / quadratic or bilinear.

Polynomial EOS is the fourth EOS to remark on herein. It is basically for building up a closer relationship between the pressure and volumetric strain for higher pressure levels (see the first EOS). It also responds to tensile stresses. The equations are:

$$P = A_1 . \mu + A_2 . \mu^2 + A_3 . \mu^3 + (B_0 + B_1 . \mu) . \rho_0 . e, \quad \text{for } \mu > 0 \text{ (compression)} \tag{3.14}$$

$$P = T_1 . \mu + T_2 . \mu^2 + B_0 . \rho_0 . e, \quad \text{for } \mu < 0 \text{ (tension)} \tag{3.15}$$

where $A_1, A_2, A_3, B_0, B_1, T_1, T_2$ are polynomial EOS coefficients [29].

The Tables 3.1. to 3.3. below lists the constants that were used in the numerical analyses:

Table 3.1. Linear EOS constants for armor steel and aluminum [74].

Linear EOS	K (GPa)
Armor Steel	159
Al-5083-H131	58,33

Table 3.2. Shock EOS (linear) constants for copper and epoxy resin [74].

Shock EOS Linear	Mie Grüneisen Parameter	c (m/s)	s_1
Copper	2	3958	1,497
Epoxy Resin	1,13	2730	1,493

Table 3.3. Polynomial EOS constants for alumina and silicon carbide [74].

Polynomial EOS	A_1 (GPa)	A_2 (GPa)	A_3 (GPa)	B_0	B_1	T_1 (GPa)	T_2 (GPa)
Alumina	231	-160	2774	0	0	231	0
Silicon Carbide	220	361	0	0	0	220	0

3.2.2. Johnson – Cook strength and failure models

The elastic strain is handled by Hooke's law. As noted formerly, elastic region could never be present if shock waves are produced in dynamic situations. In any case, whether elasto-plastic region is available, or material behaves only plastically (see Figure 2.6.), there should be a strength model to plot the behavior of solids *(G≠0)* in the plastic region to account for distortional stress component of stress tensor.

The strength model to make a description here for is Johnson-Cook strength model, which is an empirical couple with its failure model. It is mostly utilizable for ductile metals and good at capturing viscoplasticity, adiabatic transient dynamic events [75]. The model is:

$$\sigma_y = (A + B.\varepsilon^n)(1 + C.\ln\dot{\varepsilon}^*)[1 - (T^H)^m)] \qquad (3.16)$$

where σ_y: dynamic yield strength, *A*: static yield strength -transition coefficient from elastic to plastic region, *B* and *n*: strain hardening coefficient and exponent respectively, ε: equivalent plastic strain, *C*: strain rate hardening coefficient, $\dot{\varepsilon}^*$: dimensionless plastic strain rate which equals to $\dot{\varepsilon}/\dot{\varepsilon_0}$ where $\dot{\varepsilon}$: plastic strain rate and $\dot{\varepsilon_0}$: reference strain rate (1/s), T^H: homologous temperature which equals to $(T\text{-}T_{room})\ /\ (T_{melt}\text{-}T_{room})$ where T_{melt} and T_{room}: melting temperature of the material in question and room temperature respectively, *m*: thermal softening exponent. Homologous temperature ensures that at the melting temperature of the material, dynamic yield strength is zero meaning no shear modulus.

This model takes strain hardening, strain rate hardening and thermal softening effects in dynamic yield strength of a material into consideration. It is applicable for ductile metals which go through large strains, high stain rates and high temperatures in a dynamic event involving intense loading [76].

The five material variables A, B, n, C, m are compulsory to be extracted from uniaxial tensile tests and torsion tests in quasi-static conditions. Firstly, after a uniaxial tensile test, true stress-strain graph is plotted for the relevant material in conditions where $\dot{\varepsilon}^*=1$ and $T^H=0$ making strain rate hardening and thermal softening effects on material out of question. The plastic region of true stress-strain graph at hand is curve-fitted with the terms inside the first parenthesis: $A + B.\varepsilon^n$. The extraction of the terms in second and third brackets are similar. For the terms of second parenthesis, Split Hopkinson Pressure Bar (SHPB) tests could be carried out to simulate different strain rates, better up until 10^7. The new true stress-strain graphs are curve fitted with the terms of the second bracket using the figures already found in the first bracket. For the terms of the third parenthesis, the work is the same as it is done for the first. The only difference is to conduct quasi-static tensile tests in different temperatures to curve-fit a value for thermal softening exponent. Temperature change in algorithm is needed to be calculated to find and iterate homologous temperature, T^H, through formula below:

$$\Delta T = \frac{1}{\rho . C_p} \int_0^{\varepsilon_f} \sigma_y \, . \, d\varepsilon \tag{3.17}$$

where ΔT: temperature, C_p: specific heat capacity and ε_f: normal strain at failure. Integrated part in the equation is strain energy accumulated until HEL. So, we could conclude temperature change is due to strain energy accumulation.

This process is given in detail in, for example, in [28], [75], [77] by taking logarithm of the terms of the first and second bracket. It is already straightforward and in closed form for the ones of third parenthesis.

There are some modified versions[1] of the original model such as the ones presented in [72] to compensate for the unconformity between numerical and experimental results, or say, for non-representability.

Johnson-Cook failure model is suitable for ductile materials -equivalent plastic strain failure could be more convenient for relatively less ductile and harder materials [71]. The model is:

$$\varepsilon_f = \left(D_1 + D_2 e^{D_3 . \sigma^*}\right)(1 + \dot{\varepsilon}^*)^{D_4}(1 + D_5 . T^H) \tag{3.18}$$

$$D = \sum \frac{\Delta \varepsilon}{\varepsilon_f} \tag{3.19}$$

where D_1, D_2, D_3, D_4, D_5 are material failure constants, σ^*: stress triaxiality which equals to $\bar{\sigma}/\sigma_{eq}$, D: damage parameter which receives a value between [0,1], unity standing for damaged. The model takes stress triaxiality, strain rate and temperature effects in material

---

[1] $\sigma_y = (A + B.\varepsilon^n)(1 + ln\,\dot{\varepsilon}^*)^C[1 - (T^H)^m)]$ by Borvik et. al. [84]

[1] $\sigma_y = (A + B.\varepsilon^n + D.ln\,\dot{\varepsilon}^*)[1 - (T^H)^m)]$ by Gamble et. al. [50]. Gamble preferred to relate strain hardening and strain rate hardening additively, not multiplicatively.

[1] Zhang et. al. [77] left equation (3.16) unchanged. However, as the original model take the average of strain rate hardening coefficient at different strain rates, they claimed that it is not adequate to describe the real phenomena efficiently. Afterwards, they invented a new expression for strain rate hardening exponent which includes trigonometric and logarithmic terms within the body. The new expression is $C = C_0 + C_1\left(sin\,\pi \frac{ln\,\dot{\varepsilon} + C_2}{C_3}\right)$.

response into consideration. Nevertheless, most important constants are the first three as stress state is more predominant than strain rate and temperature effects to determine failure moment for most metals [78].

Johnson-Cook failure model is an instantaneous failure model. What that means is the failure of any element is realized when *D* in equation (3.19) equates to 1. Degradation of any element subjected to damage levels between [0,1] is not possible, which means any element in a mentioned-case behave as if it was carrying load though it is able to distort in the course of penetration. The ultimate strain before failure for metals involving this failure model in numerical analyses was found to be between 1,5-1,6 within this study. However, the damage well accumulates -not yielding a failure before a damage level of unity- in individual elements by equation (3.19). Post failure response of elements is nullification of stresses carried before failure [29].

The Table 3.4. below lists the constants that were used in the numerical analyses:

Table 3.4. The constants of Johnson-Cook (JC) strength and failure models facilitated in the numerical analyses.

	Armor Steel [59]	**Al-5083-H131** [79]	**Copper** [80]
A (MPa)	910	167	90
B (MPa)	596	596	292
n	0,26	0,551	0,31
C	0,014	0,001	0,025
m	1,03	0,859	1,09
$\dot{\varepsilon}_0$	1	1	1
D_1	-0,8	0,0261	0,3[2]
D_2	2,1	0,263	0,28[2]
D_3	-0,5	-0,349	3,03
D_4	0,002	0,247	0,014
D_5	0,61	16,8	1,12

[2] These values are different from the used originally in the Reference, and found by the author to serve better the numerical analyses in this study.

3.2.3. Johnson – Holmquist strength continuous model

Johnson-Holmquist strength continuous model is a specialized model to depict behavior of brittle materials under highly impulsive loads. This model was set forth by Johnson and Holmquist in 1994 [81]. The model rests on three material variables to specify: strength, pressure and damage. Strength is twofold: intact and damaged strength of material. So damaged material present protectiveness too (see subsection 2.2.2.). An EOS relationship between pressure and volume of material acknowledges bulking effect too [59]. Bulking effect is the effect of increasing pressure resulting from the inclination of fractured material volume to increase too in a confined state [66]. Finally, a damage model describes the evolution of damage on the material -from intact to fractured state. Namely, this model incorporates all needed material models in its entirety to depict material behavior under dynamic loading: EOS, strength and failure models (see Figure 3.4).

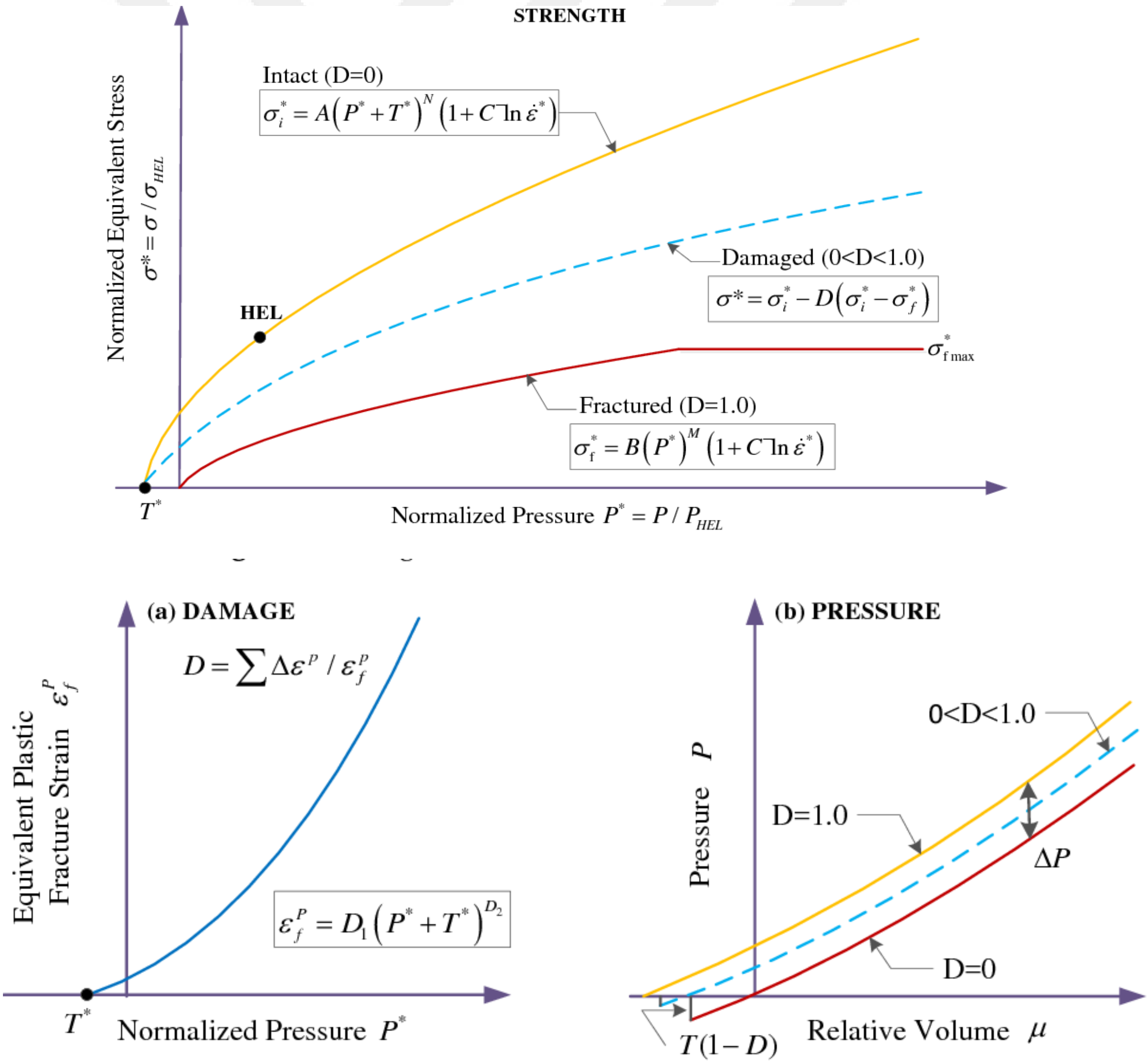

Figure 3.4. Johnson-Holmquist strength, damage and pressure models [59].

According to the model, the process is taken as elastic at the beginning with defining a polynomial EOS, which can be formulated as:

$$\mathrm{P} = \mathrm{A_1}.\mu + \mathrm{A_2}.\mu^2 + \mathrm{A_3}.\mu^3 + \Delta\mathrm{P_n}, \qquad \text{for } \mu > 0 \text{ (compression)} \tag{3.20}$$

$$\mathrm{P} = A_1.\mu, \qquad \text{for } \mu < 0 \text{ (tension)} \tag{3.21}$$

$$\Delta\mathrm{P_{n+1}} = -\mathrm{A_1}.\mu_{\mathrm{n+1}} + \sqrt{(\mathrm{A_1}.\mu_{\mathrm{n+1}} + \Delta\mathrm{P_n})^2 + 2.\beta.\mathrm{A_1}.\Delta\mathrm{U_n}} \tag{3.22}$$

$$\Delta\mathrm{U_n} = \mathrm{U_n} - \mathrm{U_{n+1}} = \frac{\sigma^2}{6\mathrm{G}} \tag{3.23}$$

where ΔP: change in bulking pressure, n: iteration (time step) number, β: elastic internal energy conversion coefficient, ΔU: change in elastic internal energy. β is normally taken as unity indicating that all elastic internal energy is converted to hydrostatic energy: bulking effect. The elastic internal energy ΔU decrease through time due to waning deviatoric stresses on material: material is damaged, gotten fractured as event progresses. Since apparent from equation (3.21), tensile pressures compel material to behave only in elastic region. Outside of the elastic region, instantaneous failure is inevitable for tensile pressures.

Later on, after a critical deviatoric stress limit is exceeded, then it can be said that material stress no longer equates to the strength in its intact state: stress relationships could be defined as:

$$\sigma^* = \sigma_\mathrm{i}^* - \mathrm{D}(\sigma_\mathrm{i}^* - \sigma_\mathrm{f}^*) \tag{3.24}$$

$$\sigma_\mathrm{i}^* = \mathrm{A}(\mathrm{P}^* + \mathrm{T}^*)^\mathrm{N}(1 + \mathrm{C}\ln\dot{\varepsilon}^*) \tag{3.25}$$

$$\sigma_\mathrm{f}^* = \mathrm{B}(\mathrm{P}^*)^\mathrm{M}(1 + \mathrm{C}\ln\dot{\varepsilon}^*) \tag{3.26}$$

where σ^*: normalized equivalent strength, σ_i^*: normalized intact strength, σ_f^*: normalized fracture strength, P^*: normalized pressure, T^*: normalized hydrodynamic tensile pressure limit. *A, B, C, M, N* are material constants. *A*: intact strength constant, *B*: fractured strength constant, *C*: strain rate constant, *M*: fractured strength exponent, *N*: intact strength exponent. As clearly seen from equations (3.25) and (3.26), stress on material is correlated to pressure and strain rate figures. Normalization of stress is done by taking the ratio of current stress to stress at HEL (σ_{HEL}). In the similar manner, the normalization of pressure and hydrodynamic tensile pressure limit is handled by taking the ratio of them above the denominator being pressure at HEL (P_{HEL}). This normalization procedure allows comparison of different materials regarding their material constants. Since hydrodynamic tensile pressure limit (see equation 3.6 and 3.15), *T*, is an experimental value; it could be taken as a material constant too.

HEL addressed at subsection 2.1.3. The expression for HEL in the model is:

$$\mathrm{HEL} = \mathrm{P_{HEL}} + \frac{2}{3}\sigma_{\mathrm{HEL}} = \mathrm{A_1}.\mu_{\mathrm{HEL}} + \mathrm{A_2}.\mu_{\mathrm{HEL}}{}^2 + \mathrm{A_3}.\mu_{\mathrm{HEL}}{}^3 + \frac{4}{3}\mathrm{G}\frac{\mu_{\mathrm{HEL}}}{1+\mu_{\mathrm{HEL}}} \qquad (3.27)$$

The equation (3.27) is noticeably comparable to equation (2.8).

Damage parameter, *D*, is calculated in the same manner with Johnson-Cook model (see equation 3.19). But the failure plastic strain is computed differently:

$$\varepsilon_{\mathrm{f}} = \mathrm{D_1}(\mathrm{P^*} + \mathrm{T^*})^{\mathrm{D_2}} \qquad (3.28)$$

where D_1: damage constant, D_2: damage exponent. Damage is not due to the dislocation mechanism as it is for metals; rather it is because of microcrack growth [39].

Since equation (3.24) suggests, just as damage on material $[0 < D < 1]$ increases after plastic strain begins to accumulate, deviatoric stress diminishes, change in internal energy and finally bulking effect emerge. An average of 200 MPa bulking pressure was monitored in ceramic elements before failure in the numerical analyses.

To define the model constants at HEL (at the point where damage accumulation starts), firstly, pressure to volume (and to volumetric strain from conservation of mass consequently) relationship is experimentally defined and graphed. From the equation (3.20); A_1, A_2, A_3 polynomial EOS coefficients are determined. Later on, HEL is experimentally determined too -through equation (2.8). After that, from equation (3.27), by substituting A_1, A_2, A_3 and HEL, volumetric strain at HEL (μ_{HEL}), P_{HEL} and σ_{HEL} is resolved.

In a nutshell, according to the algorithm, at the very beginning of impact, say first few microseconds, ceramic defies against fracture formation. The event observed in this period is called as dwell phenomenology where no penetration is involved as time elapses. But after that period, when material dynamic yield strength (HEL) is exceeded, cracks ingenerate and strength in material decrease with the consistent increasement in pressure. During this period material internal energy is transferred to bulking pressure. When damage parameter, D, equals 1; pulverized ceramic with no ballistic strength continues to be an impediment for projectile to penetrate further as it is confined: fractured strength. Afterwards maximum bulking pressure is attained and deviatoric stresses are completely set to zero, reflected tensile waves appears to be emerging then.

The Table 3.5. and 3.6. below list the constants that were used in the numerical analyses:

Table 3.5. JH-2 strength and pressure constants for alumina and silicon carbide.

	A	B	C	M	N	β	HEL (GPa)	T (GPa)	σ_f^* (Max)	$\dot{\varepsilon}_0$
Alumina [81]	0,88	0,28	0,007	0,6	0,64	1	6,57	-0,262	1	1
Silicon Carbide [66]	0,96	0,35	0	1	0,65	1	14,567	-0,37	0,8	1

Table 3.6. JH-2 damage constants for alumina and silicon carbide.

	D_1	D_2
Alumina [81]	0,01	0,28
Silicon Carbide [66]	0,7	0,48

3.2.4. Crack softening failure model

This model is simply related to when material transition into the stage where it can no longer carry tensile stress. Therefore, the model assumes the element would be rendered as incapable and unable to contribute into the overall strength of the system / material in particular. While the model could be interpreted as a tool to determine the failure point of an element, one another use of the model is to specify what thickness a material should be needed to endure a specific load. For the model, there needs to be a maximum fracture energy that the material can withstand:

$$G_f = F \times u \tag{3.29}$$

where G_f is the fracture energy that is stored on the material. For ceramics, brittle materials in general, fracture energy is:

$$G_f = \frac{F \times u}{A} \tag{3.30}$$

The fractured faces in brittle materials make up a surface unlike ductile metals that fracture at the point where the cross section of the sample reach nearly zero. Indeed, that's why we don't dub this phenomenon as "fracture" for metals but rather a "flow" before complete separation. That's another explanation that metals can be hardened but ceramics cannot: most of the time the strain energy stored when fractured is not beyond elastic.

This fracture energy is proportional to the stress applied upon, and inversely proportional to material young modulus. Namely:

$$G_f = \frac{\sigma^2 \text{ x a}}{E} \tag{3.31}$$

where *a*: aperture on the material due the damage. It can be seen from the formula above that fracture energy is the area under stress-strain curve, per unit volume, multiplied by aperture.

Fracture toughness could be formulated as:

$$K_{IC} = \sqrt{G_f \text{ x E}} = \sigma\sqrt{a} \tag{3.32}$$

The last formula can either be benefitted by suggesting a fracture toughness figure or by designating a fracture energy to failure figure extracted from experiments. Though the literature scarcely present fracture toughness for some sort of materials, ANSYS® require a fracture energy to failure figure to define the model.

3.2.5. More on strength and failure models

Cowder Symonds strength model is similar to Johnson-Cook strength model. It depends on material static yield strength, strain hardening and strain rate growth, differentiating from Johnson-Cook model only with excluding temperature softening effect. The model is:

$$\sigma_y = (A + B.\varepsilon^n)\left[1 + \left(\frac{\dot{\varepsilon}}{C}\right)^{1/P}\right] \tag{3.33}$$

where P: strain rate exponent [72], [77].

The Table 3.7. below lists the constants that were used in the numerical analyses:

Table 3.7. The CS constants for epoxy resin [44].

	A (Mpa)	B (Mpa)	n	C	p
Epoxy Resin	43	16	1	4000	0,1887

Plastic strain failure is an isotropic failure model. It should be utilized provided that the failure is expected at all (principal) directions. When the plastic strain in a material exceeds a predefined value, instantaneous failure is actualized. This model is advised to be used for ductile but low deformable materials [71].

Principal stress and strain failure models lie on directional damage. It is especially important for impact damage mechanisms such as plugging, spalling etc. User is prompted to type maximum tensile and/or shear stress for the former, maximum principal and/or shear strain for the latter model into the prescribed tabs. Especially the former model is aimed to control tensile limits of materials. When the directional property in a material exceeds a predefined value, instantaneous failure is materialized. If these models are to be used with a plasticity or strength model, user is urged to deactivate shear components (shear tabs) by typing an utopic high number. Then shear is handled by plasticity or strength model elected.

For the above-mentioned failure models, a failed cell cannot sustain deviatoric or hydrodynamic tensile stress, those stress values are all set to zero as a post failure response. That means only positive pressures can be sustained and relayed among cells [29], [39].

3.3. Computer Aided Design (CAD) Modelling

3D design was modelled in SpaceClaim, ANSYS®. 3D modelling was preferred to have better visualization of failure mechanisms after the analyses, which is to be narrated later in the Chapter 5.

Projectile was modelled to be travelling on -Y direction. Thus the target plates were modelled to be laid and mounted on X-Z plane. Only half of the design was modelled to economize run-time. Therefore, a virtual plane that is believed to cut the design in halves through X-Y plane to constitute two identical parts was designated as the plane of symmetry. Please see the Figure 3.5. below for visualization.

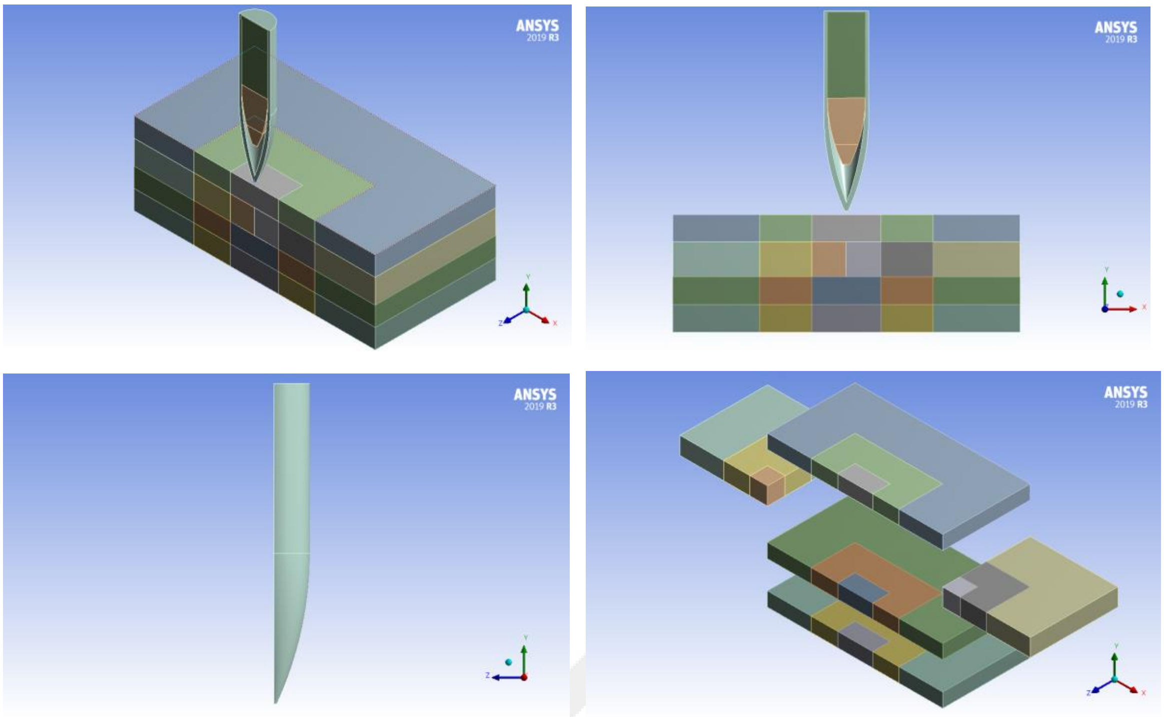

Figure 3.5. CAD modelling.

The alumina pieces are 50 x 50 mm in size and so they were modelled accordingly.

The targets were artificially split into three domains to have different structures of mesh in the radial direction both to have cheaper analyses and better results at the center, contact vicinity. Because of the division, artificial faces were created between the parts representing the same body. That's not something desired, and does not reflect the case exactly. However, mesh quality is the priority to take better results out. Thus, the integrity of plates were protected with bonded contact between afore-mentioned artificial faces. The jacket and the core were also divided into parts, which is again related to having a structured mesh (see Figure 3.6. for visualization).

Projectile jacket and core tip was modelled to form a surface rather than a point in order not to cause singularity for when the analyses were carried out. Otherwise, singularity could have emerged and caused longer run-times, artificial distortion at the elements of first contact, and falsified results (see section 3.1. for more intuitive explanation of time integration). The reducted weight was compensated somehow.

The filler was neither designed, modelled or analyzed, except trials before actual analyses. The author found out no considerable discrepancy between results yielded by either with or without filler. However, outstanding diminishment in run-time was apparent. This was due to the singularity that formed at the location where core exterior surface, jacket inner surface and filler met. It is visible from the Figure 3.6 below that the black volume where filler normally needs to be located is getting smaller and smaller just to turn into an arc without a volume. Additionally, the surrounding area of the arc needed elements having minute volume and of course minute characteristic length bearing longer run times (see section 3.1)

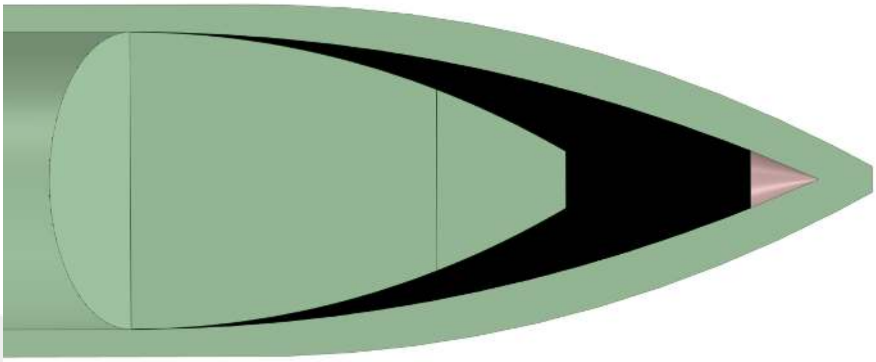

Figure 3.6. Front clip of the projectile with filler modelled.

3.4. Projectile Behavior

Some authors assumed elastic or rigid projectile models by ignoring any kind of permanent deformation on impactors after impact such as in [49], while some others characterized this approach as ‘patchy’ and defended that no material could be rigid in real world conditions such as in [65]. Besides these, some another group of authors, along with not experiencing and not assuming any deformation on projectiles in their own tests, chose to model them as deformable numerically to capture an agreement between tests and numerical analyses. Vice-versa situation is also present in literature, where deformation or fracture / failure is evident in tests but not in the numerical models the owners set up, such as in [14]. Some others chose to model the core of the bullet as rigid, and the other parts like jacket as plastic as it is in [48]. It is mostly due to the high strength of the core, material of which is commonly tungsten carbide or hardened steel. Some authors define plasticity for impactors, but not let them to fail in numerical analysis such as in [53].

Overall combinations of impactor modelling include: *1.* elastic projectile, *2.* rigid projectile, *3.* plastic projectile with no failure, *4.* plastic projectile with failure. There are examples in which the impactor tip was modelled as rigid while the remaining part was modelled as plastic to absorb plastic strain, and to avoid mesh tangling issues in lagrangian domain (see subsection 1.3.2.) and higher DOP figures than expected like it is in [28].

The combinations tried for conformity to the experiment results[3] are given in the Table 3.8. below with elicited remarks for each case.

Table 3.8. The projectile behavior combinations tried out before actual numerical analyses.

Combinations	Remarks
Entire projectile: plastic with failure	*Benchmark attribution herein. This is the combination that prevailed in this study.*
Entire projectile: elastic	Analyses proved to be running longer bringing about a "time step too small" error at one point. This is mainly because of the elements distorted unrealistically without failure.
Entire projectile: plastic with no failure	The same scenario as the one before.
The core: rigid **The jacket: plastic with failure**	The analyses lasted much quicker but with incorrect / overshot results of DOP compared to the benchmark combination and the experiment results[3].

The Figure 3.7. sets off a glimpse from a pre-analysis in which the projectile was modelled with plasticity but no failure. It is visible how the steel core was way too much shortened and expanded for an ogival core beyond the anticipated levels that could be reasoned through the available literature.

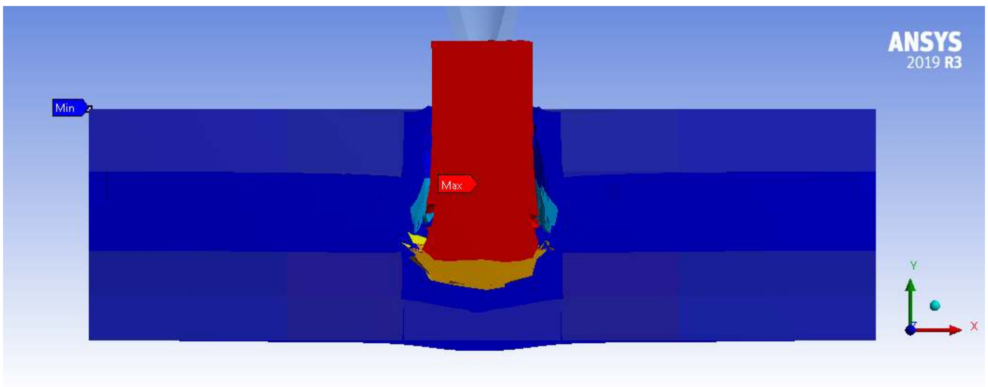

Figure 3.7. Depiction of expansion and shortening of a projectile modelled as plastic but no failure.

[3] For the experimental results, reader may refer to "Chapter-5 Results and Discussions".

At the end of the day, the author emphasize that observations should be kept upon the deformation mechanism characteristics of targets as long as the residual velocity and ballistic limit velocity figures accord among test and numerical results. Most of the times, the actual research purposes seem to have been put into surfacing the optimal armor in specific cases, as it is also the case for this study.

3.5. Contacts Definitions

Contact definition is another arrangement that deserves attention for the sake of accuracy in the analysis. For the analyses performed herein, it is not intended to designate a contact method or type either as 'the only true type' or 'best contact method' and so on. This is usually associated with plethora of variables. One of them is the material model incorporated to the analysis for a specific part, and how it behaves coupled with contact definition. The other one could be how the materials interacting each other respond to the defined contact type between them.

Contact between the parts pertaining to same body was determined as bonded contact. Any another type would not be logical as these parts are indeed created just to account for a better / structured mesh.

Contacts between the armor plates were assigned as bonded at first to account for the confinement and extra stiffness that had been added by adhesive agent at the periphery of targets (not between layers). However, it was decided the frictionless contact to be more rational as creep was possible between layers in the radial direction no matter how small it could be. Though the frictionless contact type costed 10% more run-time, it was requisite to provide a room for creeping between layers. As just a brief creep was contemplated, friction coefficient was not needed to be defined.

The contact definition for projectile was deemed to be a body interaction. Since projectile was modelled just 1 mm away from the target, the engagement was sudden, which means that element failures took place just from the start. This could be attributed to a dynamic process with the possibility that all elements could come into contact, erode each other, and pave the way for more of these interactions for the elements that could not have otherwise confronted one another. These initials required a bonded body interaction involving both jacket and core parts. In that vein, through same logic, some frictionless body interactions were defined one at a time between each relevant inner target part and projectile.

Friction was not depicted in numerical analyses, for the phenomena is assumed to have soared adiabatic heating at the impact region. That means a liquid-like behavior prevails.

Element self-contact is a secondary erosion method that can discard elements with highly contracted characteristic length. Because geometric strain erosion was employed with caution on needed locations through the analyses, another artificial erosion method was not favored.

The Figure 3.8. below provides for a visualization over contacts employed herein.

a. Bonded contact between parts of a single plate.

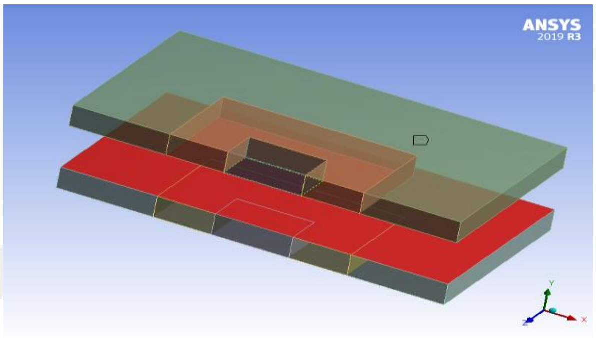

b. Frictionless contact between armor plates

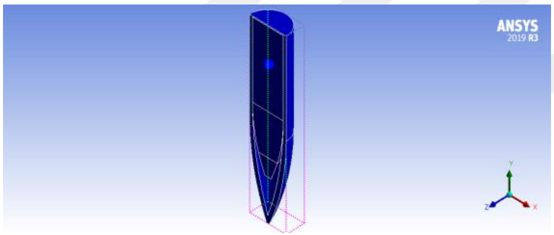

c. Bonded body interaction between jacket and core parts.

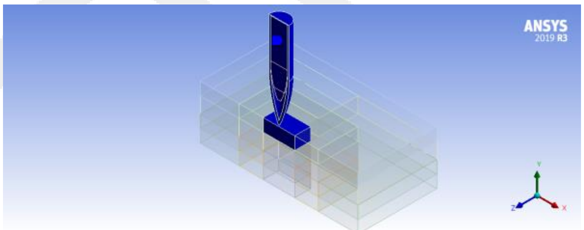

d. Frictionless body interaction between projectile and imminent target inner part.

Figure 3.8. Contact types employed.

3.6. Mesh

3.6.1. Mesh method and element type

Some of the analyses were done selecting the favorable settings above using the element types below:

Table 3.9. Mesh trials for element selection.

Trial -1 (selected)	Jacket: patch conforming	Jacket is not a sweepable body. It somewhat resembles a hollowed cylinder. The lesser of the evils is patch conforming for jacket. The core is sweepable.
	Core: sweep	
Trial-2	Jacket: patch conforming	When the core is meshed with patch conforming method, a slightly improved accuracy plus more acceptable hourglass energy values (see section 3.7 for more information on hourglass) are obtained, but it is in lieu of doubled run-time.
	Core: patch conforming	

Sweeping is the best method though the elements get more and more vulnerable to hourglass when combined with reduced integration. If the elements are first order, the danger is more imminent and obvious. Nevertheless, for the same size elements, the characteristic length of a hex element is much longer than that of a tetra element. To put it more understandable, the volume of a hex is eight times bigger than a tet with the same size. That's why sweeping was the first choice if available, as it was for targets.

The core is sweepable but only when a deceptive maneuver, so to speak, is undertaken. Partition of the core into several pieces is needed to define a new source and target each time to sweep with this method. As a result, both sweeping came to occurrence and it got possible to have bigger characteristic lengths towards the end core tip.

The jacket and the core are both meshable via cartesian method. However, this method also leaves minute elements here and there in order to snap to the shape of bodies.

The Figure 3.9. below consolidates the statements of paragraphs above.

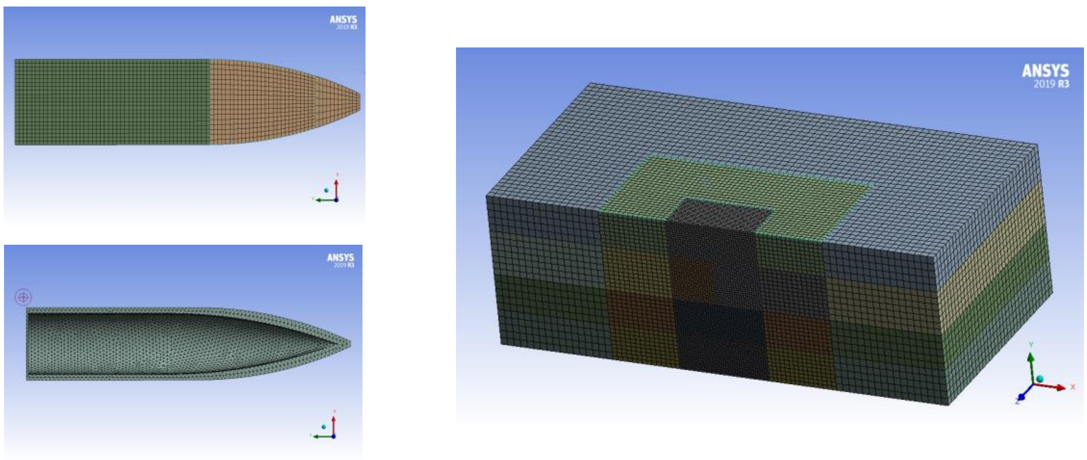

Figure 3.9. Meshed bodies.

3.6.2. Mesh size

Establishing optimum and the most economic mesh, and thus assigning the largest elements that does not hinder accuracy is utmost importance in an analysis. Therefore, a sensitivity research was done in this study to designate the optimum mesh.

For the research, five mesh sizes are specified for five locations, which are jacket, core; target outer, mid and inner. The assignment of sizes to locations are presented below in the Table 3.10. The steepness of element size change is respectively more for core and target inner locations.

Table 3.10. Element size categorization.

PART		**Mesh Method**	**Element Size**				
			Coarsest	Coarse	Ref.	Fine	Finest
Projectile	Jacket	Patch conforming	1,3e-3	1,3e-3	7e-4	7e-4	7e-4
	Core	Sweep	1e-3	7,5e-4	5e-4	4e-4	3e-4
Target	Outer	Sweep	3e-3	2,25e-3	1,5e-3	1,5e-3	1,5e-3
	Mid	Sweep	2e-3	1,5e-3	1e-3	7,5e-4	7,5e-4
	Inner	Sweep	1e-3	7,5e-4	5e-4	4e-4	3e-4

Some of the configurations were run consecutively by only changing mesh size in each run. The results are presented below in the Table 3.11. The divergence from experimental DOP could easily be seen for each successive run together with some other relevant information.

Table 3.11. DOP comparison between experimental and numeric values[4].

	Coarsest	**Coarse**	**Reference**	**Fine**	**Finest**
Configuration			**1**		
Strike Velocity (m/s)			1095		
Element Quality	0,95	0,97	0,97	0,97	
Element Number	24984	50965	185808	311891	
Run-time (min)	4	11	71	154	
Experimental DOP (mm)			30,1		
Numeric DOP (mm)	24	29,2	29	30,3	

[4] For all the experimental results not given here, reader may refer to “Chapter-5 Results and Discussions”.

Table 3.11. Continued.

	Coarsest	Coarse	Reference	Fine	Finest
Configuration			**3**		
Strike Velocity (m/s)			986,4		
Element Quality	0,92	0,95	0,95	0,95	
Element Number	23322	48198	170840	294877	
Run-time (min)	6	16	72	201	
Experimental DOP (mm)			21,9		
Numeric DOP (mm)	20,5	23,7	21,7	24,9	
Configuration			**4**		
Strike Velocity (m/s)			1102,3		
Element Quality	0,94	0,96	0,96		0,98
Element Number	23370	47816	174992		471027
Run-time (min)	5	9	47		199
Experimental DOP (mm)			24,5		
Numeric DOP (mm)	23,4	26	25		29,5
Configuration			**7**		
Strike Velocity (m/s)			978		
Element Quality	0,96	0,97	0,97		
Element Number	32280	69342	247209		
Run-time (min)	6	15	70		
Experimental DOP (mm)			23,5		
Numeric DOP (mm)	23,7	26,7	24,1		
Configuration			**10**		
Strike Velocity (m/s)			1084,2		
Element Quality	0,88	0,89	0,91	0,95	
Element Number	73454	165314	354154	447697	
Run-time (min)	8	25	94	210	
Experimental DOP (mm)			38,1		
Numeric DOP (mm)	35	38,2	39,2	39	

Table 3.11. Continued.

	Coarsest	Coarse	Reference	Fine	Finest
Configuration			**11**		
Strike Velocity (m/s)			1076,9		
Element Quality		0,97	0,97	0,97	
Element Number		51670	185653	311949	
Run-time (min)		16	80	193	
Experimental DOP (mm)			44		
Numeric DOP (mm)		44,2	41,4	42,1	
Configuration			**12**		
Strike Velocity (m/s)			1080,9		
Element Quality	0,95	0,97	0,97		
Element Number	27286	56893	201206		
Run-time (min)	7	20	75		
Experimental DOP (mm)			40,5		
Numeric DOP (mm)	35,8	43,4	43,1		
Configuration			**14**		
Strike Velocity (m/s)			1085		
Element Quality		0,97	0,97		
Element Number		62993	228003		
Run-time (min)		22	101		
Experimental DOP (mm)			55,8		
Numeric DOP (mm)		55,5	54,9		

After acquiring these values from the table above, a standard deviation-ish method was invented to decide upon the best / optimum mesh size category, even though the optimum is generally the one with the finest mesh. The formula employed is below:

$$\sigma = \sqrt{\frac{\sum_{i=0}^{i} \left| N_{DOP}^{i} - E_{DOP}^{i} \right|^{2}}{i}} \tag{3.34}$$

where σ: deviation, N_{DOP}: numerical DOP and E_{DOP}: experimental DOP.

When the formula is applied to the figures of Table 3.11, the optimum mesh size belongs to the mesh category with the smallest variation from the experimental DOP. The results are below:

Table 3.12. Numeric deviation from the experimental values.

DEVIATION				
Coarsest	Coarse	Reference	Fine	Finest
7,25	1,75	1,88	1,83	5

As seen from the table above, surprisingly the category causing least deviation happens to be ‘coarse’. Even so, some analyses were carried out with ‘reference’ mesh category for aesthetic purposes.

3.7. Analysis Settings and Setup

Many pre-analyses were carried out to find out how the changes affect the result once a specific setting was applied as standalone. This pre-work was done by introducing one setting change at a time / run to truly understand the effect generated at the end, whereby a controlled test environment happened to be created.

The Table 3.13. below demonstrate the benchmark setting preference along with the trials which brought in better or worse results when set against each other and running time, which is followed by a more detailed rationales, if required, for each setting.

Table 3.13. Analysis setting preferences.

Setting	Preference and Remarks	
Automatic Mass Scaling	Setting change is not possible since all material models have an integrated EOS. It would not be preferred though since it would lead to incorrect results changing inertia.	
Hex Integration Type	Exact	Benchmark
	First Gauss	50 % less run time without afflicting accuracy.
Tet Integration	Average Nodal Pressure	Benchmark
	Nodal Strain	No considerable change in any sense.

Table 3.13. Continued.

Setting	Preference and Remarks	
Density Update	Total	Benchmark
	Incremental	35 % less run time without afflicting the accuracy.
Hourglass Damping	Autodyn for secondary priority locations	0,1
	Flanagan Belytschko for locations over projectile route	0,02-0,03
Geometric Strain Limit	Benchmark: NO: Longer run time accompanied with mesh tangling and possible “minimum time step error”.	
	YES: 2: Shorter run time accompanied with minimized mesh tangling without errors.	
Material Failure	YES	Straightforward. Failure models were assigned for each material (see section 3.2).

Automatic mass scaling is artificial augmentation of mass in a particular location in the model, for one or more parts. This is needed to dodge longer run times stemming from elements representing low-density materials with high young modulus and / or highly small characteristic length (see subsection 2.1.1, 2.1.2 and section 3.1 for more information). It would be desired and deemed as quite helpful as long as injected in a controlled analysis settlement.[5] This study could not incorporate mass scaling setting of any level due to the cause set above in the table [29].

Integration points are the points where the average strain and stress is calculated and reflected to guide the displacement for any individual element. Thus usually, higher number of integration points (max is dubbed ‘exact’) mean more accuracy to account for every increment of load affecting any part of an element. As displacement mirrors the change of shape for an element – no matter it is via deviatoric or hydrostatic force, visual representation

[5] It is useful to run such an analysis with a small number of cycles beforehand. Then by the help of ‘timestep’ and ‘mass_scale’ commands, one can understand where the location is that the mass is added, how it changes the cycle time and how much the real world case is diverted.

of the model is also enhanced. However, pre-analyses showed that the influence is hardly noticeable for this study when only one integration point was used.

For high compression analyses like the ones pertaining this study, density change (increasement) is inevitable due to the rising in pressure and consequently in volumetric strain. Nevertheless, it is small (see section 3.2.) and has no bearing on accuracy.

Hourglass damping is closely linked to element integration method employed and the order of element utilized.[6] Shortly, for 3D hex elements with reduced integration points, hourglass energy should be introduced to the analysis to offset for unreal absence of bending stress related displacement. Hourglass energy amount is determined by damping coefficient. The hourglass energy level incorporated ought to be monitored to make sure it does not exceed one tenth of internal energy for every single element, if possible, and if not, at least for every single part at the location of collision. This study employed the type and value of coefficient advised by [29], [39], [74].

Geometric strain limit is the erosion method to be facilitated in an analysis to get rid of elements that are believed to have failed, either for not carrying stress / strain anymore or for passing the edge of reality in terms of displacement, in lagrange domain (see subsection 1.3.2). Analyses herein consist of material failure models already to account for erosion. Nevertheless, sometimes material models fail to respond for unrealistic displacement figures and lag behind in eroding these elements. For these circumstances, geometric strain limit kicks in just to be used prudently, for example, by introducing a high number lest it prematurely kill a to-be-alive element. This study cautiously incorporated geometric strain limit for some analyses containing thick layers of aluminum, which is remarkably ductile, one after the other.

[6] For more information on element integration and hourglass damping and the relation between them, refer to [85].

4. EXPERIMENTS

4.1. Target Preparations

The metal ingredients that were utilized in these experiments are MIL-DTL-46100 Armor Steel and Al-5083 H131 aluminum. Both were provided by FNSS Defense Inc. The steel plates were obtained in two different thicknesses: 8 and 12 mm. Regarding aluminum plates, they had three different thicknesses: 8 and 12,7 and 19,05 mm.

Ceramic materials to be used are alumina (Al_2O_3) and silicon carbide (SiC). Both were provided by Nurol Teknoloji Inc.

All dimensions explained herein were tried to be aligned, and thus identified through an operational research regarding all variables: the objective of the author (see section 1.5.), the target configurations that are needed to fulfill the objective given, the provisions of the provider about the study / objective and available resources of the suppliers, and capability and the settlement of the ballistic test center.

The metal plates received were then splitted into smaller square plates of 100 x 100 mm. The steel plates of 8 and 12 mm together with the aluminum plates of 8 and 12,7 mm were splitted via a laser-cutter. The last plate of aluminum with 19,05 mm thickness was splitted via band saw, due to the fact that the amount of time for a laser photon beam to cut a point cannot be more than a specific timeframe in order not to create over-heating.

Laser cutting was provided by 4th Main Maintenance Center (see Figure 4.1.), and band saw capability was secured by 5th Main Maintenance Center.

Figure 4.1. Laser cutting of armor plates.

The targets require confinement since that all configurations incorporate ceramic ingredient of one kind. Thus, layered metal-ceramic targets need a encapsulation of some sort. An adhesive agent would have been facilitated but then impedance mismatch between layers could have created immature failure (see subsection 2.2.2. for more information about ceramic failure). Screwing targets from their respective faces through bolts could be assumed the best idea (see [46], [61]) as neither does it involve external agent and nor does it endanger the role of target as being a sectional representation of an armored vehicle guaranteeing absolute confinement. Nevertheless, targets herein are 100x100 mm and the author was prudent for not affecting boundary conditions notwithstanding having made the analytical calculation to make sure boundary conditions are out of concern for the energy generated by 12,7 mm. projectiles used in the experiments (see subsection 2.1.1. for Rayleigh waves).

Ultimately, targets to be used in the experiments were all confined by encapsulating them into a cage of some sort by carbon steel sheets. This confinement left the foremost and backmost faces of the targets clear for projectile route, but provided full confinement in the orthogonal direction and partial confinement in the radial direction. At last, encapsulated targets were welded to an additional flat carbon steel sheet of 250 x 250 mm, a 100 x 100 mm section of which is corrugated at the center and extracted to clear the way of projectile. Please see Figure 4.2. for visualization.

Figure 4.2. Targets consisting of alumina.

The targets consisting of silicon carbide needed to be prepared disparately as the geometry of them does not form a square when combined in a way or another. In order to get them in a square shape, the author filled the gaps with epoxy resin after utilizing the maximum number of silicon carbide pieces that is possible for a 100 x 100 mm square shape, which connotes 19 pieces for a single sample. Of course, this preparation work entailed a simple mold to detain liquid epoxy resin, non-bonding agent to prevent bonding between mold and epoxy resin, and a 1 mm carbon steel (as thin as possible not to increase armor strength artificially) to hold hexagonal pieces and solid epoxy together. Please see Figure 4.3. for visualization.

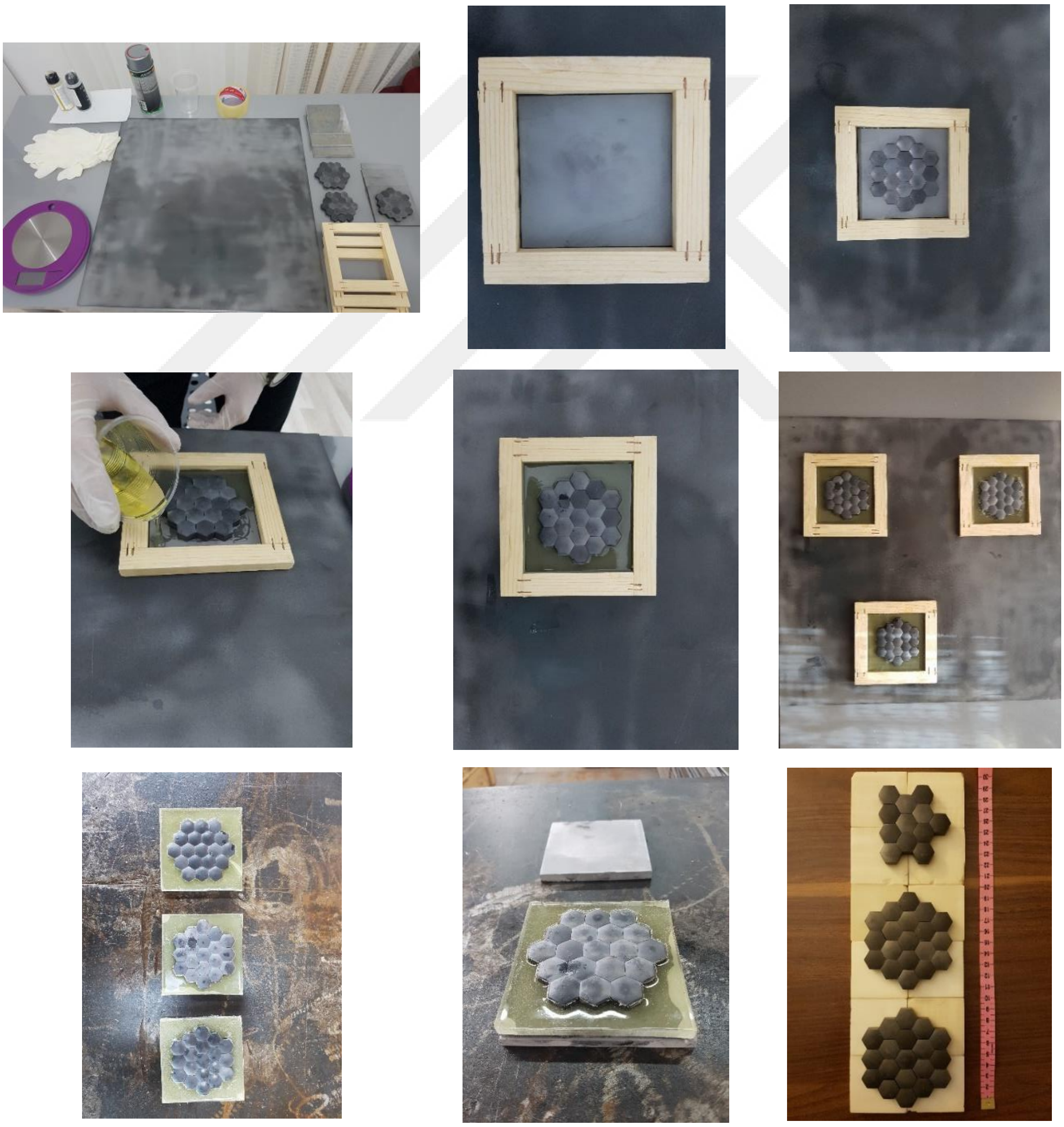

Figure 4.3. Targets consisting of silicon carbide.

4.2. Test Centre Settlement and Execution

Test center used for ballistic tests is the one belonging to CES Advanced Composites and Defense Technologies Inc. This facility was literally state-of-the-art.

It has capability to monitor and record all shots, tools such as a velocimeter to measure speed, a sensitive air conditioning system to keep track of humidity and temperature changes all the time, a fixation frame, many barrels compatible to every caliber of ammunition in accordance with some in-demand standards. It also has a safety algorithm incorporated to permit for shots only when the main entrance to test area is closed and there is nobody inside. Some visuals of the test facility are demonstrated below.

Figure 4.4. Test center.

During the tests, 15 meters of range is left between the barrel and targets. Temperature was an average of 20 Celsius. Humidity was between 35% and 45%. Every target is captured a photograph before and after the testing. Some photographs of targets are presented below.

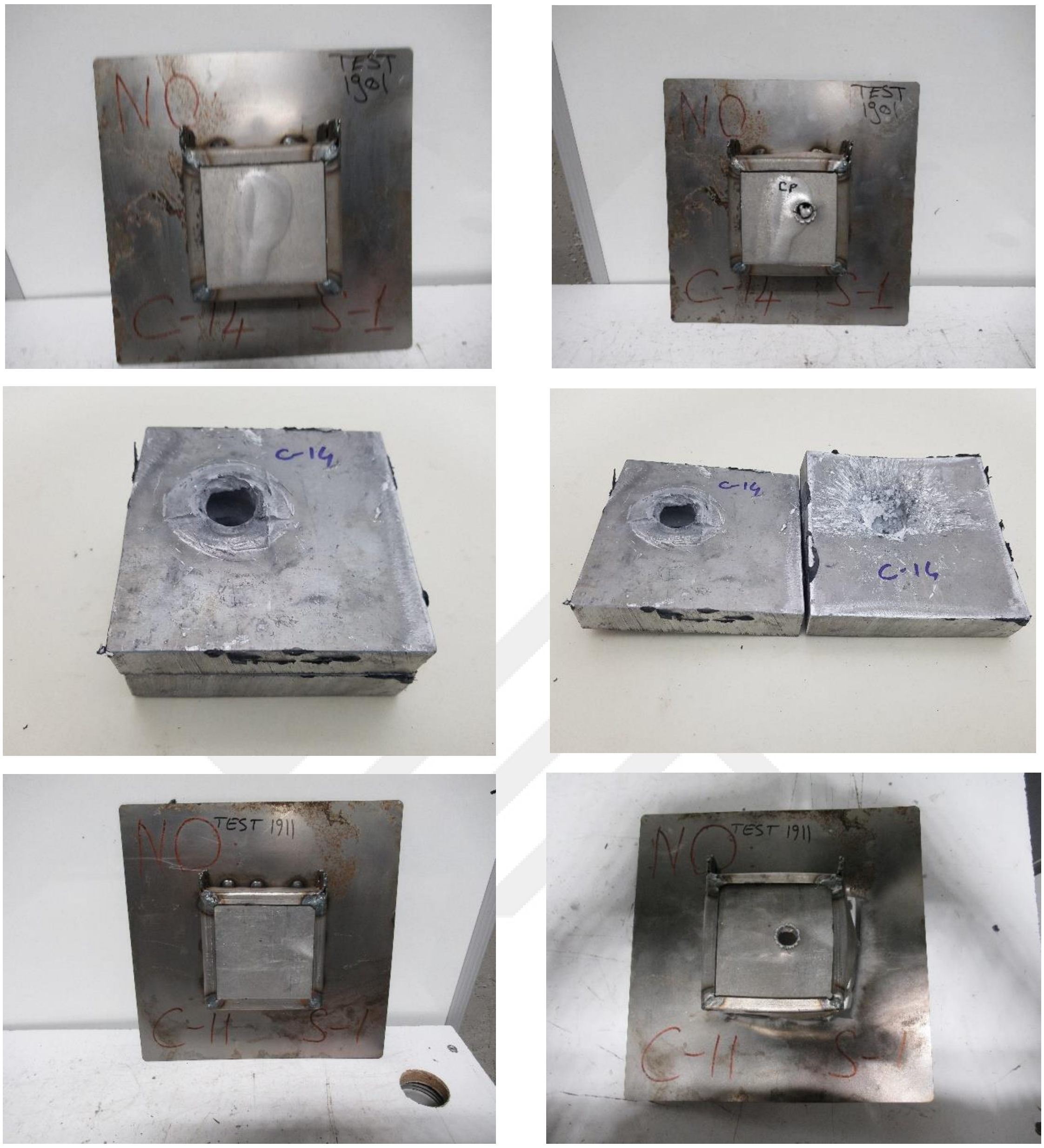

Figure 4.5. Sample target visuals[7].

[7] Please note that some configuration numbers placed on targets might have been changed after tests.

5. RESULTS AND DISCUSSIONS

5.1. Experimental Results

Experiment results are presented below in the Table 5.1. with some relevant information.

Table 5.1. Experiment results.

CATEGORY	NU.	CONFIG. NUMBER[8]	SAMPLE NUMBER[6]	TARGET THICKNESS (MM)	AREAL DENSITY (KG / M2)	STRIKE VELOCITY (M/S)	PENETRATION STATUS[9]	DEFORMATION OF TARGET (MM)	DOP / TT (Target Thickness)
1	**1**	C-1	S-1	37,05	151,5	1095	PP	30,1	81%
	2	C-1	S-2	37,05	151,5	971,4	PP	22,8	62%
	3	C-2	S-1	26	163,2	909,7	PP	20,7	80%
	4	C-2	S-2	26	163,2	1070,3	PP	24,1	93%
	5	C-3	S-1	26	149,3	986,4	PP	21,9	84%
	6	C-3	S-2	26	149,3	1073,6	PP	27,8	107%
	7	C-8	S-1	36	160,5	1084,2	**CP**	**36**[10]	106%
	8	C-9	S-1	37,05	151,5	1076,9	PP	44	119%
	9	C-9	S-2	37,05	151,5	990,4	PP	40,5	109%
	10	C-10	S-1	42	164,6	1080,9	PP	40,5	96%
	11	C-12	S-1	48,1	139,7	1085	PP	55,8	116%
2	**12**	C-4	S-3	34	184,5	959,1	PP	20,5	60%
	13	C-4	S-2	34	184,5	1102,3	PP	24,5	72%
	14	C-5	S-3	34	184,5	988,8	PP	24	71%
	15	C-6	S-1	53,4	206,8	978	PP	23,5	44%
	16	C-6	S-3	53,4	206,8	1087,8	PP	29,1	54%
	17	C-7	S-3	53,4	206,8	892,6	PP	30,4	57%
	18	C-7	S-2	53,4	206,8	1026	PP	33,6	63%
3	**19**	C-11	S-1	45,05	172,8	1079,8	PP	31,8	71%

[8] The Letters C and S denote "configuration" and "sample" respectively.
[9] PP and CP denote "partial penetration" and "complete perforation" respectively.
[10] Deformation of witness plate was 2,1 mm.

The table above harbor some significant data such as categorization of configurations in accordance with their areal density, penetration status and the ratio of DOP to TT for each configuration.

Mentioned categorization is to make comparison among configurations easier by descoping areal density via assigning the same shading color to some extent, even though the variations still exist. Third categorization is somewhat residual such that the author abstained to put it in the initial two categories.

Some deductions are immediately possible by observing DOP / TT ratio. A performance table approximating in between strike velocities is offered below therefrom.

Table 5.2. DOP / TT performance comparison among configurations.

NU.	CONFIG. NUMBER	SAMPLE NUMBER	AREAL DENSITY (KG / M2)	STRIKE VELOCITY (M/S)	DEFORMATION OF TARGET (MM)	DOP / TT
17	C-6	S-3	206,8	1087,8	29,1	54%
19	C-7	S-2	206,8	1026	33,6	63%
21	C-11	S-1	172,8	1079,8	31,8	71%
14	C-4	S-2	184,5	1102,3	24,5	72%
1	C-1	S-1	151,5	1095	30,1	81%
4	C-2	S-2	163,2	1070,3	24,1	93%
10	C-10	S-1	164,6	1080,9	40,5	96%
7	C-8	S-1	160,5	1084,2	**36**	106%
6	C-3	S-2	149,3	1073,6	27,8	107%
11	C-12	S-1	139,7	1085	55,8	116%
8	C-9	S-1	151,5	1076,9	44	119%

Expected is appeared in the table such that the targets with higher areal density performed better. However, this deduction is misleading hereupon: Configuration C-8, S-1 is perforated but still succeeds to be at some higher rank. Therefore, there is a necessity to rectify analyses. It is only possible by manifesting how it is indeed feasible. True comparison is only plausible by:

- equating areal density among configurations, approximation is not enough,
- equating strike velocity among configurations,
- involving higher strike velocities to acknowledge possible BLV figures for each configuration.

5.2. Numerical Verification

Since preconditions set at the end of previous section were not possible to apply upon in experiments, artificial configurations are necessitated in order to isolate only DOP values for comparison via numerical analyses.

Before doing that way, the verification of numerical results with the ones presented in the Table 5.1 is thus inevitable. The Table 5.3. below lays the verification level:

Table 5.3. Experimental and numerical values comparison.

NU.	CONFIG. NUMBER	SAMPLE NUMBER	STRIKE VELOCITY (M/S)	DEFORMATION OF TARGET (MM)		DEVIATION
				EXPERIMENT	NUMERIC *(REF. MESH)*	
1	C-1	S-1	1095	30,1	29	4%
2	C-1	S-2	971,4	22,8	23,3	2%
3	C-2	S-1	909,7	20,7	20,1	3%
4	C-2	S-2	1070,3	24,1	25,8	7%
5	C-3	S-1	986,4	21,9	22,2	1%
6	C-3	S-2	1073,6	27,8	25,6	8%
7	C-8	S-1	1084,2	36	36	0%
8	C-9	S-1	1076,9	44	41,4	6%
9	C-9	S-2	990,4	40,5	36,7	9%
10	C-10	S-1	1080,9	40,5	43,1	6%
11	C-12	S-1	1085	55,8	56,5	1%
12	C-4	S-3	959,1	20,5	21,1	3%
13	C-4	S-2	1102,3	24,5	25	2%
14	C-5	S-3	988,8	24	24,4	2%
15	C-6	S-1	978	23,5	24,1	3%
16	C-6	S-3	1087,8	**29,1**	**32,4**	**11%**
17	C-7	S-3	892,6	30,4	28,9	5%
18	C-7	S-2	1026	33,6	32,9	2%
19	C-11	S-1	1079,8	31,8	29,2	8%

As it is seen from the table above, only one numerical value is observed to stray away more than 10 % from its experimental peer. That doesn't seem to jeopardize subsequent and deeper numerical analyses.

5.3. Numerical Results

Numerical configurations are given in the Table 1.4. To remind again: areal density is constant and 160,6 kg/m^2.

First package of numerical analyses were administered with a strike velocity of 1100 m/s, which is approximately a ceiling value that couldn't be gone beyond in the experiments due to physical reasons: barrel warming, shell explosion and welding into inner surface of barrel etc. The results are below in the Table 5.4. Subsequent numeric analyses were only performed for the ones having been perforated previously, with a strike velocity of 900 m/s.

Table 5.4. Numerical analyses 1 and 2.

CONFIG. NUMBER	**NUMERIC-1**, V_s=1100 m/s		**NUMERIC-2**, V_s=900 m/s	
	DEFORMATION OF TARGET (MM)	**DOP / TT**	**DEFORMATION OF TARGET (MM)**	**DOP / TT**
C-1	28	69%		
C-2	29,5	115%		
C-3	33,2	103%		
C-4	31,3	106%		
C-5	31,9	109%		
C-6	36,2	93%		
C-7	38,4	99%		
C-8	**CP**		**34,9**	**97%**
C-9	44	109%		
C-10	48,5	120%		
C-11	43	106%		
C-12	49,5	88%		
C-13	**CP**		**35**	**97%**
C-14	**CP**		**35,3**	**102%**
C-15	30,7	119%		
C-16	**CP**		**24,3**	**106%**
C-17	53	95%		
C-18	57,8	103%		
C-19	**CP**		**36,4**	**90%**
C-20	54,4	134%		
C-21	34,4	89%		
C-22	30,4	75%		
C-23	26,8	66%		
C-24	55	98%		
C-25	53	95%		

According to the outcomes above, the BLV of the configurations 8, 13, 14, 16 and 19 lie somewhere between 900 and 1100 m/s. After excluding these configurations, another numeric analyses were executed continuing to attain comparative findings. The Table 5.5. below lists the outcomes elicited by an initial strike velocity of 1200 m/s and a subsequent strike velocity 1150 m/s for the perforated ones.

Table 5.5. Numerical analyses 3 and 4.

CONFIG. NUMBER	**NUMERIC-3**, V_s=1200 m/s		**NUMERIC-4**, V_s=1150 m/s	
	DEFORMATION OF TARGET (MM)	**DOP / TT**	**DEFORMATION OF TARGET (MM)**	**DOP / TT**
C-1	31,9	79%		
C-2	**CP**		**CP**	
C-3	38,7	120%		
C-4	40,2	137%		
C-5	**CP**		**34,5**	**117%**
C-6	46,1	119%		
C-7	45,2	116%		
C-9	**CP**		**CP**	
C-10	**CP**		**CP**	

Table 5.5. Continued.

CONFIG. NUMBER	NUMERIC-3, V_s=1200 m/s		NUMERIC-4, V_s=1150 m/s	
	DEFORMATION OF TARGET (MM)	**DOP / TT**	**DEFORMATION OF TARGET (MM)**	**DOP / TT**
C-11	**CP**		**49,3**	**122%**
C-12	60,9	109%		
C-15	**CP**		**CP**	
C-17	**CP**		**57,3**	**102%**
C-18	**CP**		**64**	**114%**
C-20	**CP**		**CP**	
C-21	41,7	107%		
C-22	34	84%		
C-23	30,3	75%		
C-24	**CP**		62,2	111,1%
C-25	62,5	111,6%		

According to the outcomes above, the BLV of the configurations 2, 9, 10, 15 and 20 are less than 1150 m/s, and 5, 11, 17, 18 and 24 lie somewhere between 1150 and 1200 m/s. After excluding these configurations, another package of numeric analyses was executed continuing to attain comparative findings. The Table 5.6. below lists the outcomes obtained by a strike velocity of 1250 and 1400 m/s. The latter was chosen on purpose considering DOP / TT figures in question.

Table 5.6. Numerical analysis 5 and 6.

CONFIG. NUMBER	**NUMERIC-5,** V_s=1250 m/s		**NUMERIC-6,** V_s=1400 m/s	
	DEFORMATION OF TARGET (MM)	**DOP / TT**	**DEFORMATION OF TARGET (MM)**	**DOP / TT**
C-1	-		44,7	110%
C-3	**CP**			
C-4	**CP**			
C-6	**CP**			
C-7	**CP**			
C-12	**CP**			
C-21	**CP**			
C-22	-		**CP**	
C-23	-		43,5	107,3
C-25	**CP**			

BLV for C-1 and C-23 is found later in two additional analyses to be 1425 m/s and 1445 m/s.

5.4. Failure Mechanisms

In the first place, ceramic layers couldn't be recovered since they broke in tiny chunks and chips. Even the ceramic parts closest to the center through projectile route fused with cover and backplate in pulverized condition.

The most significant finding about the failure mechanism of ceramic plates tested in this study is that radial crack formation and relief waves reflecting from the back surface reveal what the weak side of them is. The Figure 5.1. below clearly depicts the Equivalent Stress (distortion energy per unit volume) accumulation of four uppermost and lowermost central elements from innermost part of the ceramic plate-C-1 configuration.

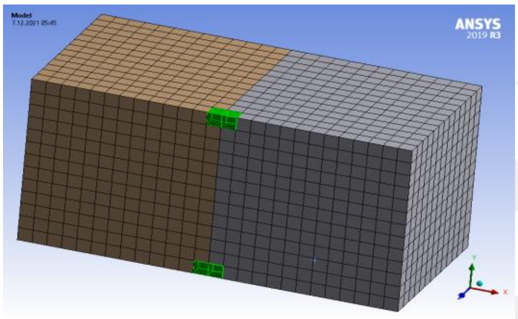

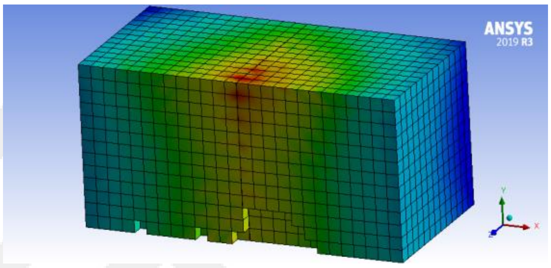

13th microsecond.

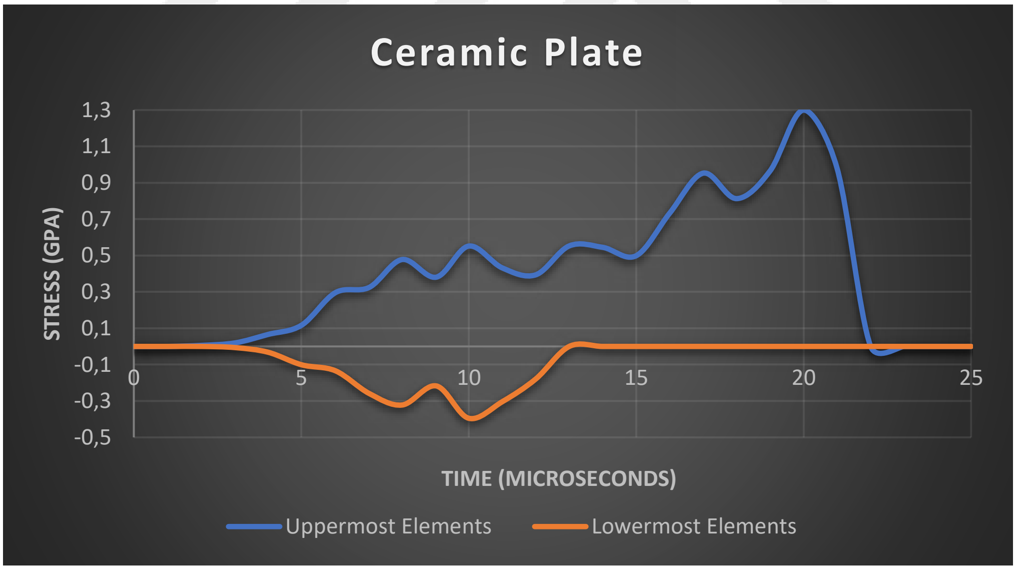

Figure 5.1. Ceramic plate failure mechanism (C-1, V_s=1100 m/s, impact direction: -Y).

According to the data given above, initial stress evolution on both element pairs is nearly the same, but one is from compressive, the other is from tensile nature. As ceramic tensile strength is low, lowermost elements were eroded just after reaching a tensile peak value of 0,4 GPa at 13th microsecond. This data supports what has usually been said on the issue in the literature such as it is in [62].

Following through this section, reader may find metal plates failure modes in the figures[11] in accordance with their location within the relevant armor system. The numerical model figures are incorporated where possible as lagrange domain is not that much qualified to portray actual footages (see section 1.3 for more explanation).

Coverplates of steel tended to ack like a brittle material. In actuality, this is the case. So indeed in shootings, no bulging or ductile hole growth was evident. One cause for this could be the existence of harder contiguous ceramic. But fragmentation stemming from radial fractures at both sides of plates were visible. Some visuals to support this assertion were given in the Figure 5.2. below.

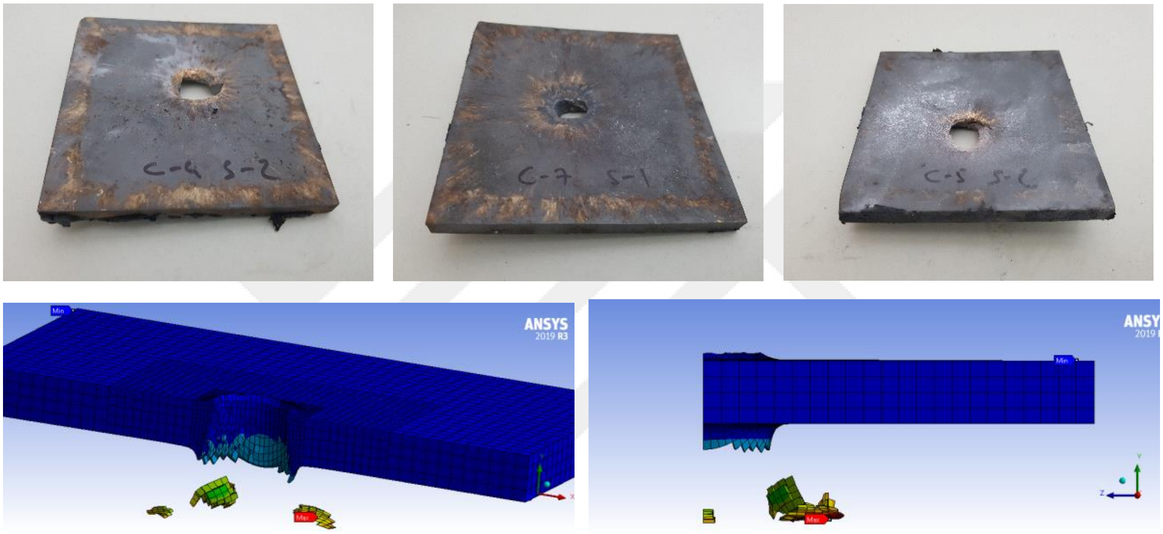

Figure 5.2. Fragmentation in steel coverplate.

As seen from the numerical image, the failure is delineated as if it was fragmentation by petalling. However, photographs prove that the main failure mechanism is radial fracture at the back side followed by cavity expansion. Anyway, numerical images are in conformity with footages to some extent in terms of bending-absence and fragmentation.

For backplates of steels, bending and bulging is becoming more monitorable as no supporting hard and stiff layer was available at the backside. The Figure 5.3. below is such to prove this.

[11] Please note that some configuration numbers placed on targets might have been changed after tests. Keep this in mind through this section.

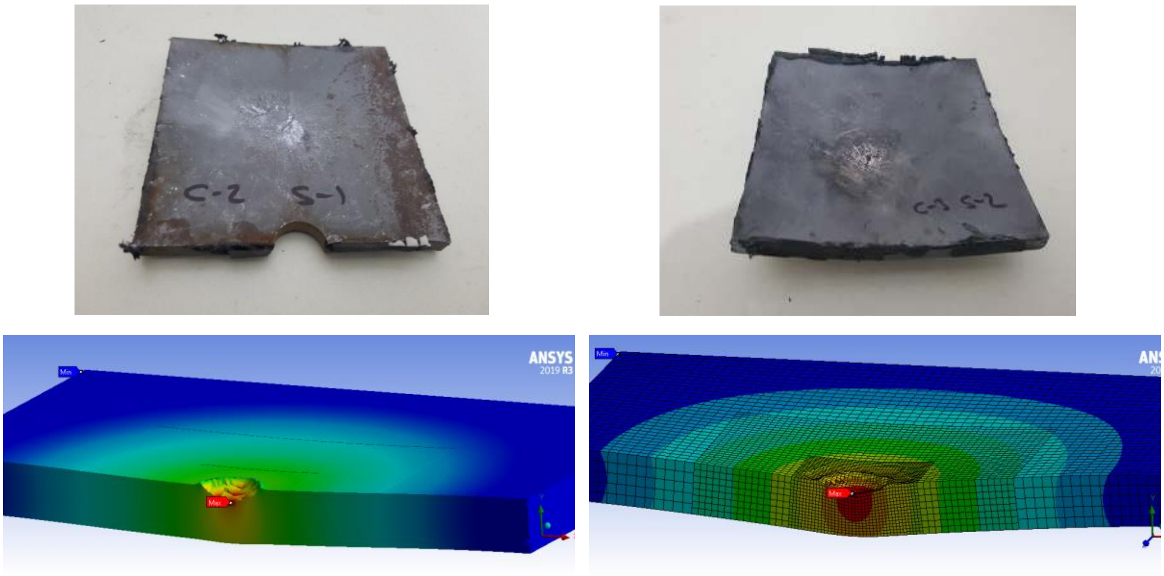

Figure 5.3. Visible bending in steel backplates.

Backplates of aluminum inclined to have broad and but shallow bulging incorporating boundary edges in the radial direction. Evidently, the reason seems to have been the presence of hard ceramic layer just before to dissipate the remaining energy of projectile after perforation of steel coverplate. The Figure 5.4. below exhibits this phenomenon. Top left photograph is able to show fusion between pulverized ceramic and aluminum.

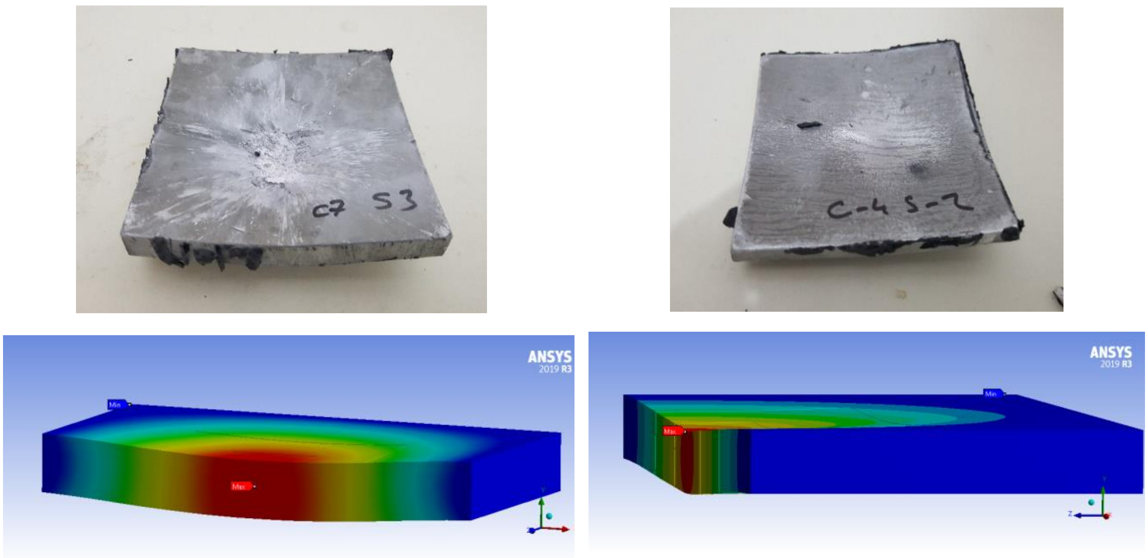

Figure 5.4. Broad and shallow bulging in aluminum backplates.

See the Figure 5.5. below to be acquainted with more localized and deeper bulging of low- stiffness, layered aluminum backplates. This is a typical example how low stiffness coming from material property, layering and having no supportive layer at the back side might deteriorate the overall performance.

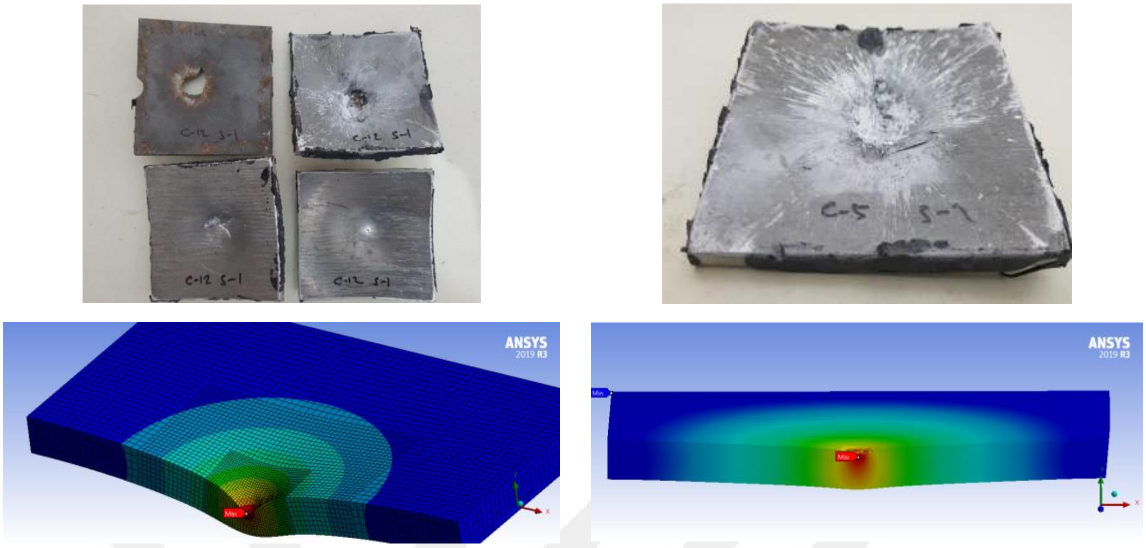

Figure 5.5. Localized bulging on layered aluminum backplates.

Aluminum coverplates showed us common examples of ductile hole growth with evident bulging and material piling up in the radial direction at the entrance of projectile. Again, at the backside of aluminum coverplates lip formation is visible as harder subsequent ceramic layer hinder it from bulge to a considerable degree. The visuals in the Figure 5.6. below can help a reader envision.

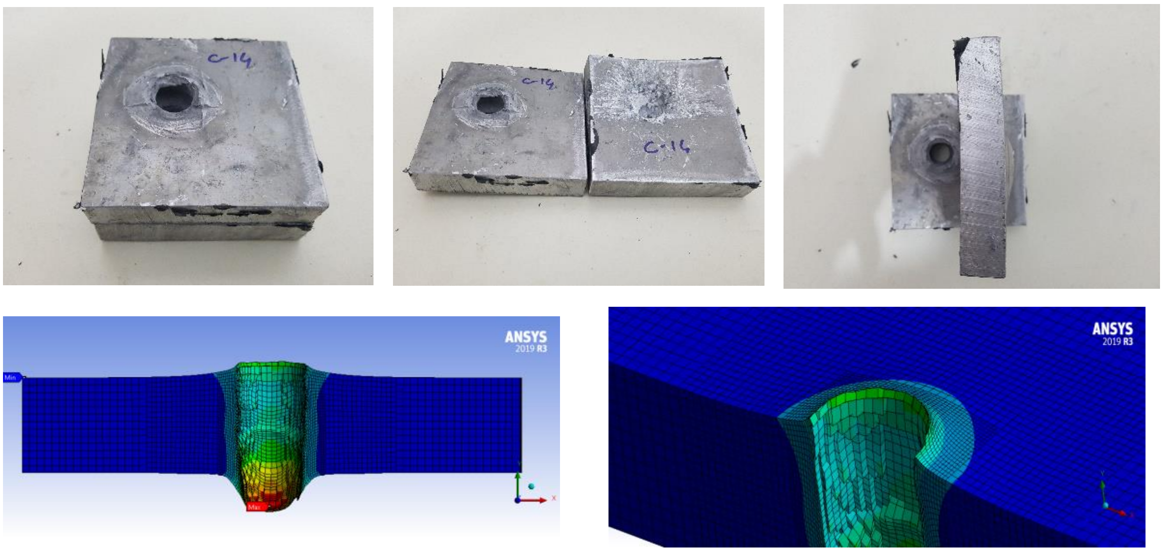

Figure 5.6. Ductile hole growth on aluminum coverplates.

6. CONCLUSIONS

6.1. Thesis Objectives-Driven Conclusions

Keeping in mind the initial results of the previous chapter, there could easily be drawn up a performance collocation. The chart below can depict this order: while the each BLV range is the same for a couple of configurations, the DOP / TT ratio is taken to be the determinant for juxtaposing them in between.

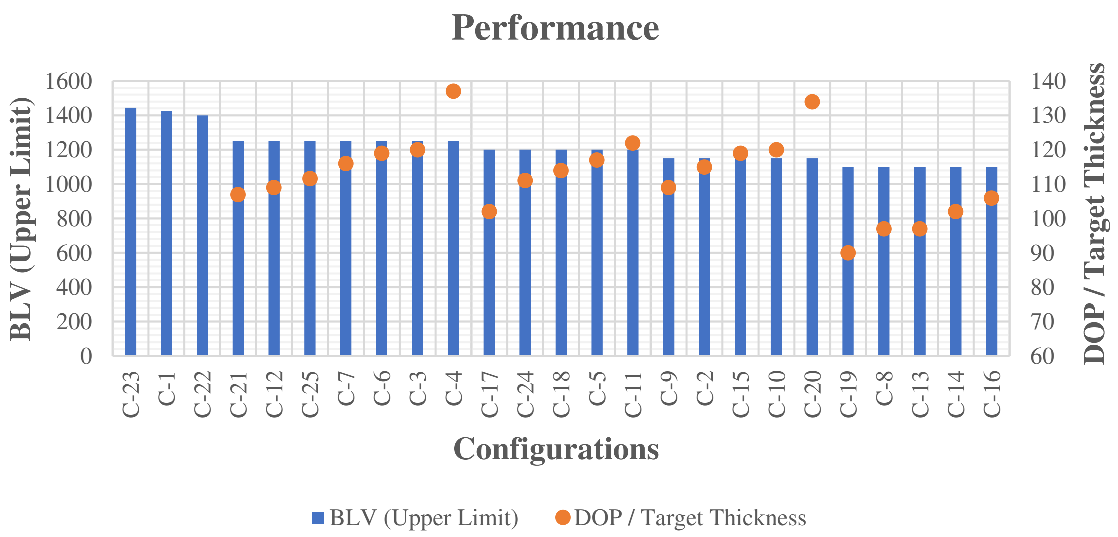

Figure 6.1. Performance of configurations.

As the Figure 6.1. suggest, the best performance was obtained from configuration 23 and 1. Since this is a stating-the-obvious case, more analysis should be involved to fulfill the objective of this study.

<u>The optimum thickness ratio (range) between ceramic and backplate:</u>

The configurations that could favor an optimum thickness ratio between ceramic and backplate are C-1 and C-8. Since BLV of C-1 is 1400 m/s and that of C-8 is found to be less than 1100 m/s, this finding supports a ceramic to backplate ratio of 0,4, which is not in line with the findings of [31], [41] that endorse a thicker ceramic plate compared to backplate. However, the findings of praising backplate thickness on performance herein is such that was found on [46].

Bulking pressure levels of ceramic plates in both configurations can shed a light on the performance diversity. The Figure 6.2. below reveal how these levels differentiate.

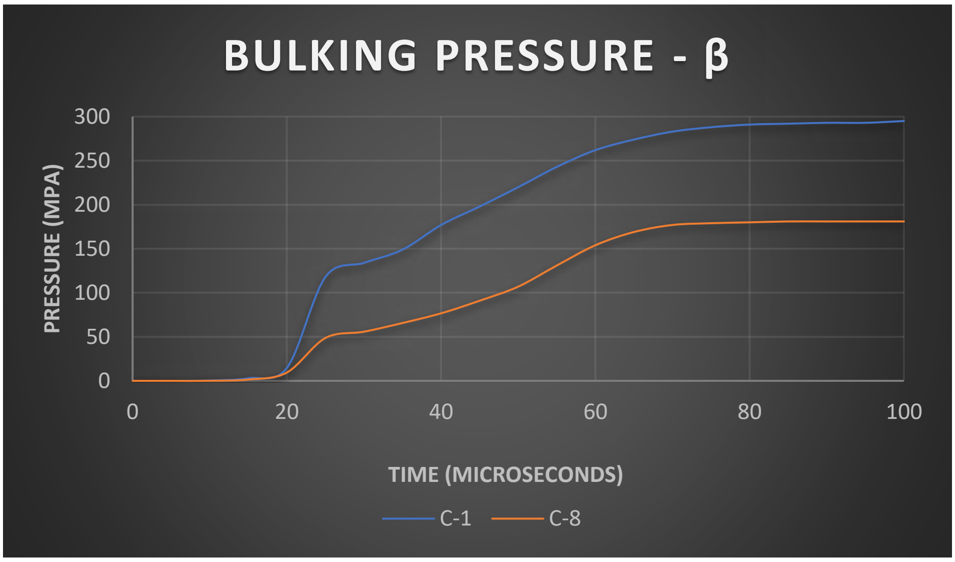

Figure 6.2. Bulking pressure levels of C-1 and C-8, V_s=1100 m/s.

C-1 bulking pressure levels, thus the pressure levels in accordance with equations 3.20 and 3.22 at the end are higher than those of C-8. It means C-1 was better supported compared to C-8 ceramic plates: thick aluminum backing of C-1 waxed the stiffness and left more limited room for ceramic to get out of the way of projectile. This might have added to the function of C-1 ceramic layer to decelerate projectile more effectively.

Fracture energy levels are given below for ceramic layers of both configurations.

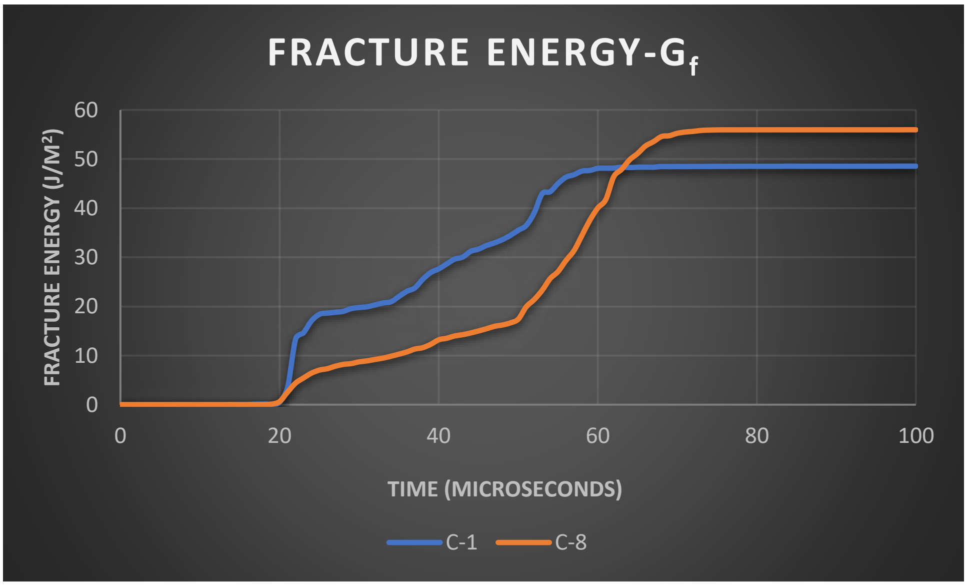

Figure 6.3. Fracture energy levels of C-1 and C-8, V_s=1100 m/s.

Figure 6.3. shows us the superiority of half-thickness ceramic layer in C-1 to absorb more energy than that of C-8 for 40 microseconds. The author acknowledges the handover

on 63rd microsecond (for C-8, it is exactly when the projectile tip met with backing layer, when the ceramic layers started to accumulate pressure by feeling the support of backing layer properly) and as a result of C-8 ceramic volume advantage that lately kicked in. Despite this, the area under C-1 on the graph is more than that of C-8.

<u>The ceramic material itself: density and toughness:</u>

For this issue, the performance discrepancy between the configurations C-2 and C-3 is decisive. Since C-3 performed better in the analyses by roughly 100m/s, there could be pronounced that ceramic density and toughness matter. The author attributes this overt performance augmentation to harder surface, high energy dissipation capability of silicon carbide due to higher young modulus and sound speed compared to alumina. The findings here agree with the ones found in [82], but not conform to the others located in [46] that suggests ceramic compressive strength and toughness would create no difference.

<u>The so-called added value of metal strength: the better performance means the more strength or ductility the metal would have:</u>

Metals are usually utilized as cover or backplate content in armor systems consisting of ceramic plates in the middle. Therefore, while assessing metals to find the best mechanical property to take advantage of, the location where they will be placed is equally important.

The configurations to compare here are C-1, C-2, C-9 and C-12.

As C-1 performed better than the others, that could be inferred that strength for coverplate and ductility for backplate should be opted. The author favors this result to the ability of a ductile backplate to absorb the remaining energy of projectile which is already blunted -and the energy of which is dissipated- by a harder coverplate and a ceramic layer. On the other hand, it seems interesting that utilizing ductile metal both at the front and back (C-12) was more favorable than C-2 and C-9. <u>Nevertheless, the author require reader to be careful as every time ductility may not accompany lower density, as it is the case here that creates thicker cover or back plates. In that vein, the comparison of C-2 and C-9 might be thought-provoking.</u> As for the disparity between C-2 and C-9, there is almost none.

With reference to these results, it is very clear both cover and backplate strength and hardness figures are of same and equal importance, contrary to the findings of [45], [47] which praise either only coverplate or backplate strength / hardness values.

+Below the Figure 6.4. is designed to inform the reader about the best metal selection for cover and backplate considering remaining kinetic energy of the projectile and the DOP / TT ratio on a specific timeframe.

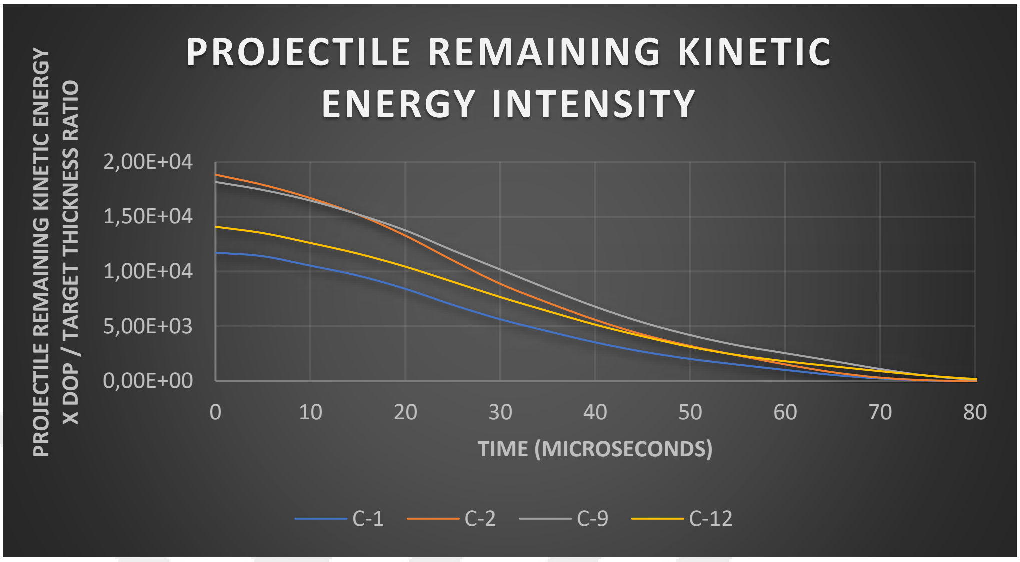

Figure 6.4. Projectile remaining kinetic energy comparison.

The numbers on the Y axis are intended to be recognized only as the intensity of the remaining kinetic energy of the projectile to enable comparison: they are each a result of the multiplication of projectile remaining kinetic energy and DOP / Target ratio on a specific timeframe.

The figure should be construed in this manner: smaller the area under the line, the better the configuration is and the more favorable the metal selection is. Thus, the performance order of these configurations is to be C-1, C-12, C-9 and C-2, the latter two being almost identical. This could be verified by the Figure 6.1.

The effect of layering on backplate:

The configurations to set against one another here are C-1, C-9, C-10, C-19 and C-20. C-1 is the configuration the backplate of which is divided into three or five equal-thickness layers in C-10 and C-20 respectively. Since the performance order between them is C-1, C-10 and C-20, it is observable that layering deteriorates performance, although the difference between the latter two is small.

This result could be reinforced with the findings of C-9 and C-19 with a armor steel backplate, monoblock and 4 layer structure respectively. Therefore, no matter the material property of backplate is, the layering of backplate is equally disrupting for performance.

This outcome is not new to the literature and fairly conforming to the findings in general such as in [37].

The so-called added value of strength / ductility on layered armor plates used for backplate:

Sui generis configurations that are designed to measure up the effect of ductility or strength on layered backplate are C-4 and C-5. Because C-4 achieved better than C-5 by nearly 50 m/s difference in BLV, for any layering on backplate, the frontmost layer should be the one with higher strength, contrary to the findings of [53]. However, the finding herein is also consolidated with the results of [35] with the exception of double layer backplates achieving better compared to monoblock equivalents.

The effect of layer thickness optimization for layered backplate:

C-1, C-10 and C-11 could be resorted to find out best division ratios for a monoblock plate. As C-11 achieved better, the finding might be said to agree with that of [37], stating that the first layer ought to be thinner than the other in double layer armors. Nevertheless, it does not scrap the overall result of this thesis that layering is favorable by no means.

The effect of ceramic-metal-ceramic-metal lamination (not seen as much in literature):

As Medvedovski E. stated in [83], ceramic-metal plate collocation repeating itself consecutively is a methodology which has rarely been tried out. C-6, C-7 and C-21 are such configurations to serve for this purpose.

Regarding the performances of C-6 and C-7, it is readily monitored that this method might not work that way. Pronouncing the case with "might" implies the minute performance difference between them. However, regarding C-21, the monoblock version of C-6 and C-7 -employing single plates of the same total thickness- the performance disparity gets bigger in favor of C-21: as immediately observed from the Figure 6.1., it has a lower DOP / TT ratio within the same range of BLV.

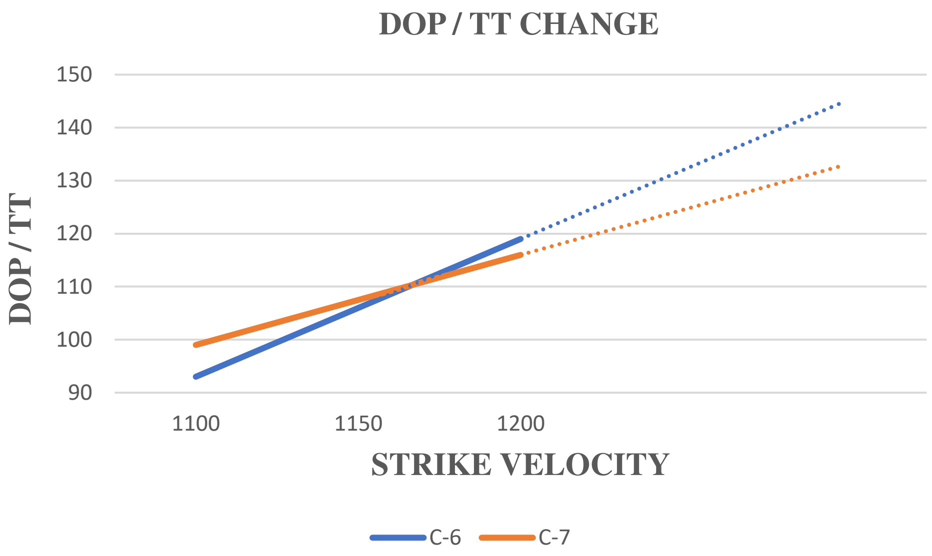

Figure 6.5. DOP / TT change rates of C-6 and C-7.

The Figure 6.5. above indicates the change rate of DOP to TT. Although C-6 performed better for a strike velocity of 1100 m/s, table turns and it happened to get worse for C-6 in terms of strike velocities above 1200 m/s. That could be acknowledged as the configuration C-7 might prove better compared to the C-6 for higher strike velocities provided thicknesses of layers in both of them are increased with the same scaling factor. The author thinks that it is because energy dissipation capability of thicker aceramic layer in C-7 gets more pronounced as strike velocity gets higher.

<u>The effect of layering on ceramic:</u>

C-13 and C-14 are two of the worst configurations. Although C-14 has 4 layers of ceramic with the same total thickness as it is for C-13, the disparity in performance is hard to spot. The author is in the opinion that the backplate was so thin that it couldn't support the contiguous ceramic, whether is monoblock or layered. Because the failure mechanism might have converted from being impedance mismatch confronted by shock waves through ceramic layers to insufficient stiffness to hold ceramic in place.

It is still remarkable to analyze the results of C-7 and C-21. The difference between these configurations is that the monolithic blocks of ceramic and aluminum backplate were divided into two in C-7. Though they performed the same for a strike velocity of 1100 m/s, and ballistic limit velocity figures are not more than 1250 m/s for both of them; the disparity between DOP / TT change rates is visible in the Figure 6.6. The slope of C-7 is more than twice the slope of C-21: 8 and 17 respectively.

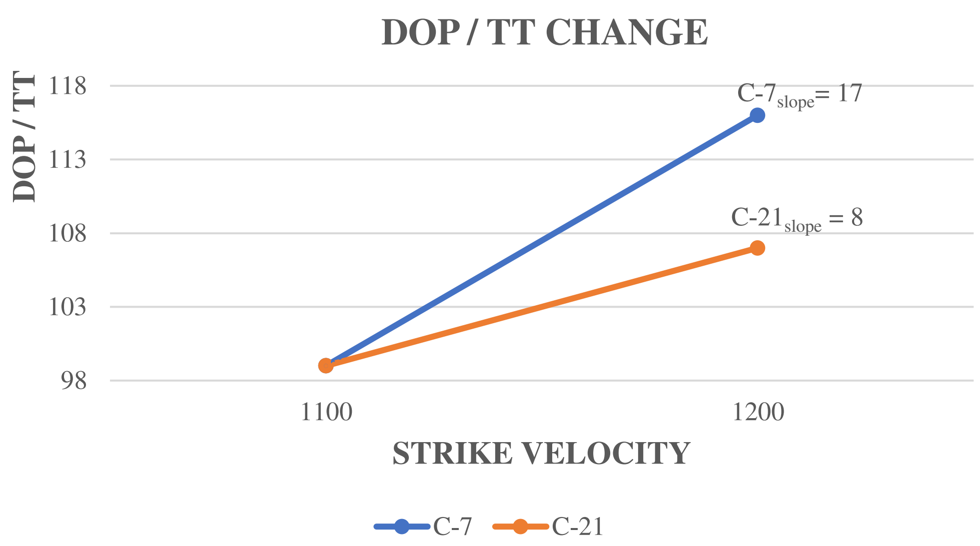

Figure 6.6. DOP / TT change rates of C-7 and C-21.

<u>The effect of layering on coverplate:</u>

C-2, C-12, C-15, C-16, C-17 and C-18 are designed to answer whether the coverplate layering has a positive contribution to the performance. The outcome is no different than the one encountered when it is for backplate.

What is interesting to note is while the layering for aluminum is worsening just beginning from dividing into two, it is steadier for a steel coverplate that it tends to keep performance from dropping too much. For aluminum plates, this finding is just the opposite of how aluminum behaves against layering when employed as backplate.

<u>The effect of spacing:</u>

Spacing effects are tried out for two distinct situations: the effect of a spacing that is located between coverplate and ceramic layer, the effect of a spacing that is located between two layers of coverplate.

For the armor steel coverplates, C-1, C-15, C-22, C-23 assert that spacing conduces to a remarkable performance increase. While the layered coverplate of C-15 without spacing performed way worse than its monoblock peer, C-1, the layered coverplate of C-22 with spacing nearly equalized the performance with its monoblock counterpart. What is more compelling is that the spacing located after coverplate but before ceramic layer even outperformed monoblock structure of C-1.

For the aluminum coverplates, things are a bit different. As C-12, C-17, C-24, C-25 suggest, the spacing between two layers of aluminum coverplate does no good in terms of performance. However, C-25 with a spacing just before ceramic layer perform in a similar manner with C-12.

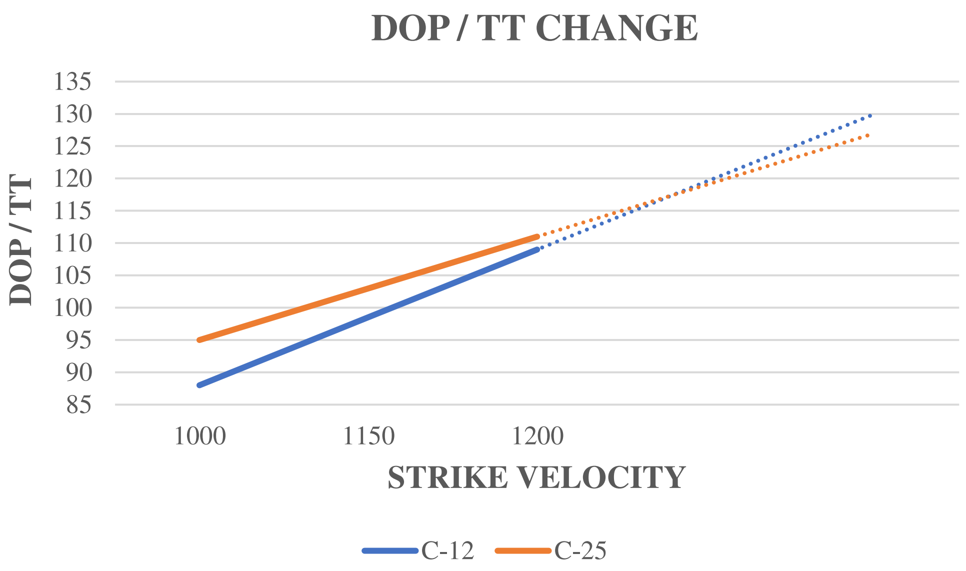

Figure 6.7. DOP / TT change rates of C-12 and C-25.

Though the trends of each configuration on the graph increasingly continue their way starting from 1100 m/s demonstrate that DOP / TT ratios -and so BLV figures- of each configuration tend to converge at some point when strike velocity is 1300 m/s or so, further numeric trials showed that convergence would turn out to be a divergence. The Table 6.1. below delineates the result of a further run, most probably proving that unsupported aluminum coverplate with lesser stiffness decreases the performance.

Table 6.1. Numerical Analysis 7.

CONFIG. NUMBER	**NUMERIC-7,** V_s=1350 m/s	
	DEFORMATION OF TARGET (MM)	**DOP / TT**
C-12	64,1	95%
C-25	69,6	104%

The Table 6.2. below summarizes all the conclusions matching with relevant configuration, where possible.

Table 6.2. Summary of Conclusions.

Configuration	Conclusions Summary
C-1	The best configuration possible with a hard metal as coverplate and a ductile material as backplate.
C-2 / 12	For the same areal density and same metal to be used as cover and backplate, ductility should be sought on metal selection rather than strength. Careful discretion is advised for this conclusion as ductility may not accompany low density and thicker layers every time.
C-3	Tougher ceramics with higher young modulus and sonic velocity perform better.
C-4	Higher strength metal at the front of layered backplate yields better performance.
C-8	Ceramic to backplate thickness ratio should be or around 0,5.
C-11	Thinner layer at the front is better for double layered backplates.
C-18 / 20	Aluminum plates performance degrade instantly in coverplates when doubled, but degradation is not so drastic in backplates when doubled.
C-9 / 10 / 19 / 20	Layering on backplate does no good to overall performance.
C-15 / 16 / 17 / 18	Layering on coverplate does no good to overall performance.
C-22 / 24	Spacing between the layers of coverplate is better.
C-23 / 25	Spacing between the coverplate and ceramic layer is the best.

6.2. Stanag 4569 Conformity-An Analogy

Up to now, differently configurated targets with same areal density were impacted via projectiles having same impact velocities just to bring forth the best configuration possessing the highest BLV or lowest DOP for a specific impact velocity. This could be named as a target point of view.

To serve for a projectile point of view, the best configuration (C-1) was remodeled and analyzed to extract lowest possible areal density to stand against a Stanag 4569 KE-4 situation.

A too basic relationship / analogy was constructed to correspond to the change of projectile from 12,7 to 14,5 caliber making use of "conservation of energy", as given below:

$$BLV_{14,5} = \left(\frac{BLV_{12,7}^2\ x\ M_{12,7}}{M_{14,5}}\right)^{0,5} \tag{6.1}$$

where 14,5 mm projectile mass is 64,2 mm. When minimum standard BLV for 14,5 mm projectile impact is taken as 911 m/s pursuant to Stanag 4569 KE-4, and the mass for the mentioned projectile, 64,2 gr, was included into calculation; the desired BLV for a 12,7 mm projectile emerges as a round value of 1080 m/s.

As C-1 was already capable to withstand such a velocity, the C-1 was needed to be remodeled with a lower areal density, which is just above a required level that does not permit a perforation, namely pertains to BLV. After some trials, a thickness scaling factor of 0,70 proved to be successful, which means thickness figures of all the plates were cut down for 30%. Consequently, the C-1 (redesigned) configuration was obtained, then tried out for a numerical analysis involving a 12,7 mm projectile with an impact velocity of 1080 m/s. The data is tabulated below consisting of layer material and its thickness in millimeters:

Table 6.3. Redesigned C-1 configuration to meet the terms of Stanag 4569 KE-4.

	Layer-1	Layer-2	Layer-3	Total Thickness (mm)	Areal Density (kg/m^2)	DOP / TT
C-1 (Redesigned)	S 5,6	Al_2O_3 7	Al 15,75	28,35	**112,42**	**110%**

In accordance with this approach, C-1 (Redesigned) configuration is able to meet the requirement of Stanag 4569 KE-4: withstand a 14,5 mm projectile having a velocity of 911 m/s. The new configuration has an areal density of 112,42 kg/m^2.

However, this analogy approach has some built-in drawbacks:

- The components (plastic work, bending, friction, fragmentation, heat etc.) of kinetic energy transformed are assumed to keep their proportions in overall total energy unchanged when an impactor type is altered. However, this is not possible due to the inelastic nature of these impact events.

- Stanag 4569 KE-4 stipulates a velocity of 911 m/s from a distance of 200 m to target. Here, this value is taken as strike velocity. Nevertheless, rather than disrupting, this assumption makes the calculation more conservative.

- Boundary conditions are assumed still to be staying on the safe side. But, that wouldn’t be feasible as intensity of Rayleigh waves increases. Furthermore, confinement is assumed still to stand against radial forces generated by the projectile. To be more straightforward, the results obtained by 100 x 100 mm target dimension might not reflect, for example, the armor package of a vehicle when impacted by a 14.5 mm projectile.

- As failure modes are determinants of performance to some degree, assumption of confronting the same modes may drift the analogy to fallacy. However, the author does not anticipate a change in failure modes as these two projectile types have more or less the same nose structure and caliber radius head (CRH).

7. RECOMMENDATIONS

There are some issues to be amended in terms of experiments and numerical analyses inherent to plate and ceramic dimensions, and numeric domain employed in the thesis. If they could be addressed in further trials, the author believes that would pave the way for more literal trust on results.

Boundary conditions:

Confinement of targets were executed by utilizing 1 mm thick carbon sheet metals. Worsening the case of them turning out to be thinner than they should be, confinement in the radial direction was provided by bending the sheets inwards by only 10 mm creating a pocket for plates to settle into (see section 4.1 for visuals of target preparation). This margin was found to be lesser than it ought to be since fixation of plates in the normal direction couldn't be satisfied due to projectile exerting high amount of force upon these margins. This in turn yielded so-called global failure mechanisms that normally would have ended up being more local.

Larger plates of such as 40 x 40 cm would definitely produce more trustworthy results as targets could retain their own moment of inertia to withstand projectile normal force in terms of global perspective. Some ways to connect larger plates would be gluing them to each other or bolting them through their thickness. Ceramics would be encapsulated within backplates by carving a dent on them to mount ceramic pieces inside. Therefore, no artificial confinement would be needed to be materialized.

At the end, employing larger plates of such as 40 x 40 cm was by no means the applicable case for me because of narrow resources.

In a nutshell, while targets were big enough to offset for Rayleigh waves, sufficient global inertia was found to be obtained by larger targets.

Projectile velocity:

Projectile velocity couldn't be increased any further than 1100 m/s roughly due to the capability of barrel that they were fired through. This negatively affected the situation by curbing the possible deductions that could have otherwise been elicited. In the tests, despite the highest value of velocity employed, only one sample was perforated, which means the author got obliged to trust in numerical values beyond that speed figure.

Devising thinner plates to serve for the same objectives as same as this study was not possible because of resources at hand, and of the obligation to design them in a way to enable comparison between them in accordance with objective-dependent variables.

Larger caliber ammunition use would be thought of a solution. However, confinement would not stand against any caliber beyond the one used in the tests.

Lagrangian domain:

Lagrangian domain embodies some issues disrupting visibility of failure mechanisms that took place, causing shear locking, hour glassing, mesh tangling, singularity, element division within run etc. (see subsection 1.3.2 for more information on lagrangian domain).

SPH domain is the best alternative to lagrange as it does not engender mesh tangling with no mesh available. Furthermore, second order element use with reduced integration should certainly leave no room for shear locking or hourglass effect on hex elements. Therefore, Autodyn server would be preferred.

REFERENCES

[1] Editors of Brittanica, “Encyclopedia Britannica, Bballistics, 22 May 2019, https://www.britannica.com/science/ballistics, Accessed 21 Nov. 2021.” [Online]. Available: http://www.britannica.com/EBchecked/topic/190219/epistemology.

[2] G. ÖZTÜRK, “Numerical and Experimental Investigation of Perforation of ST-37 Steel Plates By Oblique Impact,” 2010.

[3] U.S. Army Material Command, *Interior Ballistics of Guns*. 1965.

[4] İ. ÖZER, “Balistik Çarpma Etkisinin Sonlu Elemanlar Yöntemiyle İncelenmesi,” 2015.

[5] T. DEMİR, “Metal ve Katmanlı Zırh Malzemelerinin 7,62 mm’lik Zırh Delici Mermiler Karşısında Balistik Başarımlarının İncelenmesi,” 2008.

[6] Wikipedia, “Ballistics, https://en.wikipedia.org/wiki/Ballistics, Accessed 21 Nov. 2021.” .

[7] H. DENİZ, “Çift Fazlı Bir Çeliğin 7,62 mm’lik Zırh Delici Mermi Karşısında Balistik Davranışının İncelenmesi,” 2009.

[8] M. AYDIN, “Fonksiyonel Kademelendirilmiş Sandviç Plakaların Balistik Davranışı,” 2014.

[9] Emre Aytav, “Verbal Communication, ‘Interior Ballistics’, 14 Mar. 2021.,” 2021.

[10] R. Parnes, *Solid Mechanics in Engineering*. 2001.

[11] Federation of American Scientists, “Introduction to Naval Weapons Engineering, https://fas.org/man/dod-101/navy/docs/es310/ballstic/Ballstic.htm, Accessed 21 Nov. 2021.” .

[12] G. F. Silsby, J. A. Zook, and K. Frank, “Memorandum Report BRL-MR-3960.,” 1992.

[13] M. ÇAKIR, “Penetration of Metallic Plates By Kinetic Energy Projectiles.,” 2015. doi: 10.13140/RG.2.1.1936.5922.

[14] T. Børvik, S. Dey, and A. H. Clausen, “Perforation resistance of five different high-strength steel plates subjected to small-arms projectiles,” *Int. J. Impact Eng.*, 2009, doi: 10.1016/j.ijimpeng.2008.12.003.

[15] Wikipedia, “Kinetic Energy Penetrator, https://en.wikipedia.org/wiki/Kinetic_energy_penetrator, Accessed 21 Nov. 2021.” .

[16] Sofrep, “Long Range Shooting: External Ballistics – Dynamic Stability, https://sofrep.com/news/long-range-shooting-external-ballistics-dynamic-stability, Accessed 21 Nov. 2021.” .

[17] F. Elaldi, “Verbal Communication, ‘Spalling’, 15 Oct. 2020.,” 2020.

[18] Wikipedia, “Shaped Charge, https://en.wikipedia.org/wiki/Shaped_charge, Accessed 18 Nov. 2021.” .

[19] K. Walter, “Shaped charges pierce the toughest targets,” *Sci. Technol. Rev.*, no. June, pp. 17–22, 1998.

[20] W. Walters, “An Overview of the Shaped Charge Concept.”

[21] B. Dodd and F. Coghe, “Damage caused to metals by kinetic and chemical energy projectiles Security and Use of Innovative Technologies Against Terrorism Damage caused to metals by kinetic and chemical energy projectiles,” 2015, doi: 10.13140/RG.2.1.1667.0881.

[22] M. Held, “Liners for Shaped Charges.,” *J. Battlef. Technol.*, vol. 4, 2001.

[23] Z. X. Zhang, *Rock Fracture and Ballistics.* 2016.

[24] Z. Zhang, L. Wang, and V. V. Silberschmidt, “Damage Response of Steel Plate to Underwater Explosion: Effect of Shaped Charge Liner,” *Int. J. Impact Eng.*, vol. 103, pp. 38–49, 2017, doi: 10.1016/j.ijimpeng.2017.01.008.

[25] H. Kemmoukhe, Z. Burzić, S. Savić, S. Terzić, D. Simić, and M. Lisov, “Improvement of shaped charge penetration capability and disturbation of the jet by explosive reactive armor,” *Teh. Vjesn.*, vol. 26, no. 6, pp. 1658–1663, Nov. 2019, doi: 10.17559/TV-20190216141334.

[26] M. B. Steven, “Liner Materials: Resources, Processes, Properties, Costs, and Applications.”

[27] militaryimages.net, “Artillery Ammunition, https://www.militaryimages.net/media/105mm-heat.7142, Accessed 8 Sep. 2021.” .

[28] N. KILIÇ, “Development of Multi-Layer Ballistic Armor Panel With Simulation and Ballistic Tests,” 2014.

[29] Ansys, *Explicit Software for Nonlinear Dynamics*. 2005.

[30] T. L. Warren and K. L. Poormon, “Penetration of 6061-T6511 aluminum targets by ogive-nosed VAR 4340 steel projectiles at oblique angles: Experiments and simulations,” *Int. J. Impact Eng.*, vol. 25, no. 10, pp. 993–1022, 2001, doi: 10.1016/S0734-743X(01)00024-0.

[31] R. Chi, A. Serjouei, I. Sridhar, and G. E. B. Tan, “Ballistic impact on bi-layer alumina/aluminium armor: A semi-analytical approach,” *Int. J. Impact Eng.*, 2013, doi: 10.1016/j.ijimpeng.2012.10.001.

[32] R. Zaera and V. Sánchez-Gálvez, “Analytical modelling of normal and oblique ballistic impact on ceramic/metal lightweight armours,” *Int. J. Impact Eng.*, 1998, doi: 10.1016/S0734-743X(97)00035-3.

[33] J. P. Lambert and G. H. Jonas, “Towards standardization in terminal ballistics testing: velocity presentation.,” 1976.

[34] T. W. Ipson and R. F. Recht, “Ballistic-penetration resistance and its measurement - Two impulses reduce the velocity of a projectile passing through a barrier. Minimum perforation velocity is determined by using the ballistic pendulum to measure the impulse due to barrier strength,” *Exp. Mech.*, vol. 15, no. 7, pp. 249–257, Jul. 1975, doi: 10.1007/BF02318057.

[35] D. Yunfei, Z. Wei, Y. Yonggang, S. Lizhong, and W. Gang, “Experimental investigation on the ballistic performance of double-layered plates subjected to impact by projectile of high strength,” *Int. J. Impact Eng.*, 2014, doi: 10.1016/j.ijimpeng.2014.03.003.

[36] S. Dey, T. Børvik, X. Teng, T. Wierzbicki, and O. S. Hopperstad, "On the ballistic resistance of double-layered steel plates: An experimental and numerical investigation," *Int. J. Solids Struct.*, 2007, doi: 10.1016/j.ijsolstr.2007.03.005.

[37] Y. Deng, W. Zhang, and Z. Cao, "Experimental investigation on the ballistic resistance of monolithic and multi-layered plates against ogival-nosed rigid projectiles impact," *Mater. Des.*, 2013, doi: 10.1016/j.matdes.2012.06.048.

[38] Wikipedia, "Finite Element Method, https://en.wikipedia.org/wiki/Finite_element_method, Accessed 3 Mar.2021." .

[39] Ansys, "Explicit Dynamics Lecture: Material Models," 2018.

[40] J. A. Zukas and D. R. Scheffler, "Impact effects in multilayered plates," *Int. J. Solids Struct.*, 2001, doi: 10.1016/S0020-7683(00)00260-2.

[41] M. Lee and Y. H. Yoo, "Analysis of ceramic/metal armour systems," *Int. J. Impact Eng.*, 2001, doi: 10.1016/S0734-743X(01)00025-2.

[42] Wikiversity, "Nonlinear finite elements/Lagrangian and Eulerian descriptions, https://en.wikiversity.org/wiki/Nonlinear_finite_elements/Lagrangian_and_Eulerian_descriptions, 10 Oct.2020." .

[43] I. Ben Belgacem, H. Khochtali, L. Cheikh, E. M. Barhoumi, and W. Ben Salem, "Comparison Between Two Numerical Methods SPH/FEM and CEL by Numerical Simulation of an Impacting Water Jet," *Lect. Notes Mech. Eng.*, no. January, pp. 50–60, 2020, doi: 10.1007/978-3-030-24247-3_7.

[44] R. Zaera, S. Sánchez-Sáez, J. L. Pérez-Castellanos, and C. Navarro, "Modelling of the adhesive layer in mixed ceramic/metal armours subjected to impact," *Compos. Part A Appl. Sci. Manuf.*, vol. 31, no. 8, pp. 823–833, Aug. 2000, doi: 10.1016/S1359-835X(00)00027-0.

[45] W. L. Goh, Y. Zheng, J. Yuan, and K. W. Ng, "Effects of hardness of steel on ceramic armour module against long rod impact," *Int. J. Impact Eng.*, 2017, doi: 10.1016/j.ijimpeng.2017.08.004.

[46] H. D. Espinosa, N. S. Brar, G. Yuan, Y. Xu, and V. Arrieta, "Enhanced ballistic

performance of confined multi-layered ceramic targets against long rod penetrators through interface defeat," *Int. J. Solids Struct.*, vol. 37, no. 36, pp. 4893–4913, Sep. 2000, doi: 10.1016/S0020-7683(99)00196-1.

[47] M. Übeyli, H. Deniz, T. Demir, B. Ögel, B. Gürel, and Ö. Keleş, "Ballistic impact performance of an armor material consisting of alumina and dual phase steel layers," *Mater. Des.*, 2011, doi: 10.1016/j.matdes.2010.09.025.

[48] A. Manes, F. Serpellini, M. Pagani, M. Saponara, and M. Giglio, "Perforation and penetration of aluminium target plates by armour piercing bullets," *Int. J. Impact Eng.*, 2014, doi: 10.1016/j.ijimpeng.2014.02.010.

[49] X. Teng, T. Wierzbicki, and M. Huang, "Ballistic resistance of double-layered armor plates," *Int. J. Impact Eng.*, 2008, doi: 10.1016/j.ijimpeng.2008.01.008.

[50] E. A. Gamble, B. G. Compton, and F. W. Zok, "Impact response of layered steel-alumina targets," *Mech. Mater.*, 2013, doi: 10.1016/j.mechmat.2013.01.008.

[51] T. Børvik, M. J. Forrestal, O. S. Hopperstad, T. L. Warren, and M. Langseth, "Perforation of AA5083-H116 aluminium plates with conical-nose steel projectiles - Calculations," *Int. J. Impact Eng.*, 2009, doi: 10.1016/j.ijimpeng.2008.02.004.

[52] M. J. Forrestal and T. L. Warren, "Perforation equations for conical and ogival nose rigid projectiles into aluminum target plates," *Int. J. Impact Eng.*, 2009, doi: 10.1016/j.ijimpeng.2008.04.005.

[53] E. A. Flores-Johnson, M. Saleh, and L. Edwards, "Ballistic performance of multi-layered metallic plates impacted by a 7.62-mm APM2 projectile," *Int. J. Impact Eng.*, 2011, doi: 10.1016/j.ijimpeng.2011.08.005.

[54] S. Yadav and G. Ravichandran, "Penetration resistance of laminated ceramic/polymer structures," *Int. J. Impact Eng.*, vol. 28, no. 5, pp. 557–574, 2003, doi: 10.1016/S0734-743X(02)00122-7.

[55] A. I. O. Zaid, "Stress Waves in Solids, Transmission, Reflection and Interaction and Fractures Caused by Them: State of the Art," *Int. J. Theor. Appl. Mech.*, vol. 1, pp. 155–164, 2016.

[56] D. B. Rahbek, J. W. Simons, B. B. Johnsen, T. Kobayashi, and D. A. Shockey, "Effect of composite covering on ballistic fracture damage development in ceramic plates," *Int. J. Impact Eng.*, vol. 99, pp. 58–68, Jan. 2017, doi: 10.1016/J.IJIMPENG.2016.09.010.

[57] B. A. Roeder and C. T. Sun, "Dynamic penetration of alumina/aluminum laminates: Experiments and modeling," *Int. J. Impact Eng.*, 2001, doi: 10.1016/S0734-743X(00)00031-2.

[58] N. K. Gupta, M. A. Iqbal, and G. S. Sekhon, "Effect of projectile nose shape, impact velocity and target thickness on the deformation behavior of layered plates," *Int. J. Impact Eng.*, 2008, doi: 10.1016/j.ijimpeng.2006.11.004.

[59] T. J. Holmquist, D. W. Templeton, and K. D. Bishnoi, "Constitutive modeling of aluminum nitride for large strain, high-strain rate, and high-pressure applications," *Int. J. Impact Eng.*, vol. 25, no. 3, pp. 211–231, Mar. 2001, doi: 10.1016/S0734-743X(00)00046-4.

[60] Y. Deng, W. Zhang, and Z. Cao, "Experimental investigation on the ballistic resistance of monolithic and multi-layered plates against hemispherical-nosed projectiles impact," *Mater. Des.*, 2012, doi: 10.1016/j.matdes.2012.05.021.

[61] D. Sherman and T. Ben-Shushan, "Quasi-static impact damage in confined ceramic tiles," *Int. J. Impact Eng.*, vol. 21, no. 4, pp. 245–265, Apr. 1998, doi: 10.1016/S0734-743X(97)00063-8.

[62] Z. Zuoguang, W. Mingchao, S. Shuncheng, L. Min, and S. Zhijie, "Influence of panel/back thickness on impact damage behavior of alumina/aluminum armors," *J. Eur. Ceram. Soc.*, 2010, doi: 10.1016/j.jeurceramsoc.2009.08.023.

[63] B. A. Gama, J. W. Gillespie, T. A. Bogetti, and B. K. Fink, "Innovative design and ballistic performance of lightweight composite integral armor," *SAE Tech. Pap.*, no. March, 2001, doi: 10.4271/2001-01-0888.

[64] Y. O. Kacan and F. Elaldi, "Ballistic performance of unidirectionally oriented carbon fiber reinforced composite armor with high-velocity impact," doi: 10.1177/0731684420929084.

[65] E. ÖZŞAHİN, “Alüminyum Levhaların Yüksek Hızlı Çarpma Yükleri Altındaki Davranışları,” 2008.

[66] D. S. Cronin, K. Bui, C. Kaufmann, G. Mcintosh, T. Berstad, and D. Cronin, “Implementation and Validation of the Johnson-Holmquist Ceramic M aterial Model in LS-Dyna.”

[67] J. A. Smith, J. M. Lacy, and D. Lévesque, “Use of the Hugoniot elastic limit in laser shockwave experiments to relate velocity measurements ARTICLES YOU MAY BE INTERESTED IN,” vol. 1706, p. 80005, 2016, doi: 10.1063/1.4940537.

[68] D. P. Gonçalves, F. C. L. De Melo, A. N. Klein, and H. A. Al-Qureshi, “Analysis and investigation of ballistic impact on ceramic/metal composite armour,” *Int. J. Mach. Tools Manuf.*, 2004, doi: 10.1016/j.ijmachtools.2003.09.005.

[69] J. As, A. Zukas, J. Wiley, N. York, C. I. Brisbane, and I. Toronto, “High velocity impact dynamics.,” 1990.

[70] Z. Rosenberg and E. Dekel, *Terminal ballistics*. 2020.

[71] A. Dallocchio, A. Bertarelli, F. Carra, N. Mariani, L. Peroni, and M. Scapin, “Advanced Numerical Methods for Simulation of Shock-waves Induced by High Energy Particle Beams.”

[72] L. Schwer, “Optional Strain-Rate Forms for the Johnson Cook Constitutive Model and the Role of the Parameter Epsilon _ 0,” *6th Eur. LS-DYNA Users' Conf.*

[73] P. C. Gautam, R. Gupta, A. C. Sharma, and M. Singh, “Determination of Hugoniot Elastic Limit (HEL) and Equation of State (EOS) of Ceramic Materials in the Pressure Region 20 GPa to 100 GPa,” in *Procedia Engineering*, Jan. 2017, vol. 173, pp. 198–205, doi: 10.1016/j.proeng.2016.12.058.

[74] Ansys-2019R3 Workbench, “Analysis System:Explicit Dynamics, Engineering Data: Material Modelling.” 2019.

[75] İ. Memiş, “Impact Response of Ramor 500 Armor Steel Subjected to High Velocities,” 2016.

[76] G. R. Johnson and W. H. Cook, “A Constitutive Model and Data for Metals Subjected to Large Strains, High Strain rates and High Temperatures,” 1983.

[77] Y. ben Zhang, S. Yao, X. Hong, and Z. gang Wang, “A modified Johnson–Cook model for 7N01 aluminum alloy under dynamic condition,” *J. Cent. South Univ.*, vol. 24, no. 11, pp. 2550–2555, 2017, doi: 10.1007/s11771-017-3668-5.

[78] P. Skoglund, M. Nilsson, and A. Tjernberg, “Fracture modelling of a high performance armour steel,” *J. Phys. IV Fr.*, vol. 134, pp. 197–202, 2006, doi: 10.1051/jp4:2006134030.

[79] A. H. Clausen, T. Børvik, O. S. Hopperstad, and A. Benallal, “Flow and fracture characteristics of aluminium alloy AA5083-H116 as function of strain rate, temperature and triaxiality,” *Mater. Sci. Eng. A*, 2004, doi: 10.1016/j.msea.2003.08.027.

[80] B. Yildirim, S. Muftu, and A. Gouldstone, “Modeling of high velocity impact of spherical particles,” *Wear*, vol. 270, no. 9–10, pp. 703–713, 2011, doi: 10.1016/j.wear.2011.02.003.

[81] G. R. J. and T. J. Holmquist, “An improved computational constitutive model for brittle materials,” *AIP Conf. Proc. 309, 981*, 1994.

[82] E. Medvedovski, “Ballistic performance of armour ceramics: Influence of design and structure. Part 1,” *Ceram. Int.*, vol. 36, no. 7, pp. 2103–2115, Sep. 2010, doi: 10.1016/j.ceramint.2010.05.021.

[83] E. Medvedovski, “Ballistic performance of armour ceramics: Influence of design and structure. Part 2,” *Ceram. Int.*, 2010, doi: 10.1016/j.ceramint.2010.05.022.

[84] T. Borvik, O. S. Hopperstad, T. Berstad, and M. Langseth, “A computational model of viscoplasticity and ductile damage for impact and penetration,” *Eur. J. Mech. A/Solids*, vol. 20, no. 5, pp. 685–712, 2001, doi: 10.1016/S0997-7538(01)01157-3.

[85] E. Q. Sun, “Shear locking and hourglassing in MSC Nastran, ABAQUS and ANSYS.in MSC. Software Users Meeting.,” *Msc Softw. users Meet.*, pp. 1–9, 2006.